Effective Prestress Evaluation of the Varina-Enon Bridge Using a Long-Term Monitoring System and Finite Element Model

Rachel Amanda Brodsky

Thesis submitted to the faculty of the Virginia Polytechnic Institute and State University in partial fulfillment of the requirements for the degree of

Master of Science
In
Civil Engineering

Carin L. Roberts-Wollman (Chair)
Iaonnis Koutromanos
Rodrigo Sarlo

June 16, 2020
Blacksburg, Virginia

Keywords: Post-tensioned concrete, Prestress loss, Varina-Enon Bridge, Finite element modeling, Creep, Shrinkage, Thermal gradient

Long Term Monitoring of the Varina-Enon Bridge: Effective Prestress Evaluation

Rachel A. Brodsky

ACADEMIC ABSTRACT

The Varina-Enon Bridge is a cable-stayed, precast, segmental, post-tensioned box girder bridge located in Richmond, Virginia. Inspectors noticed flexural cracking in July of 2012 that prompted concerns regarding long-term prestress losses in the structure. Prestress losses could impact the future performance, serviceability, and flexural strength of the bridge. Accurately quantifying prestress losses is critical for understanding and maintaining the structure during its remaining service life.

Long-term prestress losses are estimated in the Varina-Enon Bridge using two methods. The first utilizes a time-dependent staged-construction analysis in a finite element model of the full structure to obtain predicted prestress losses using the CEB-FIP ’90 code expressions for creep and shrinkage. The second method involves collecting data from instrumentation installed in the bridge that is used to back-calculate the effective prestress force.

The prestress losses predicted by the finite element model were 44.9 ksi in Span 5, 47.8 ksi in Span 6, and 45.3 ksi in Span 9. The prestress losses estimated from field data were 50.0 ksi in Span 5, 48.0 ksi in Span 6, and 46.7 ksi in Span 9. The field data estimates were consistently greater than the finite element model predictions, but the discrepancies are relatively small. Therefore, the methods used to estimate the effective prestress from field data are validated. In addition, long-term prestress losses in the Varina-Enon Bridge are not significantly greater than expected.

Long Term Monitoring of the Varina-Enon Bridge: Effective Prestress Evaluation

Rachel A. Brodsky

GENERAL AUDIENCE ABSTRACT

Post-tensioned concrete uses stressed steel strands to apply a precompression force to concrete structures. This popular building technology can be used to create lighter, stiffer structures. Over time, the steel strands experience a reduction in force known as *prestress losses*. Accurately quantifying prestress losses is critical for understanding and maintaining a structure during its remaining service life.

The Varina-Enon Bridge is a cable-stayed, prestressed box girder bridge located in Richmond, Virginia. Inspectors noticed cracking in July of 2012 that prompted concerns regarding long-term prestress losses in the structure. Prestress losses were estimated using two methods. The first method utilized a computer model of the full bridge. The second method used data from sensors installed on the bridge to back calculate prestress losses.

It was found that the prestress losses estimated from field data were slightly greater than, but closely aligned with, the computer model results. Therefore, it was concluded that the Varina-Enon Bridge has not experienced significantly more prestress losses than expected.

ACKNOWLEDGEMENTS

I would like to thank the Virginia Department of Transportation for their support on this project, including providing documentation regarding the design and construction of the Varina-Enon Bridge. I would also like to thank Seth Lindley, whose previous work, thesis, and guidance were immensely helpful for this next phase of the project. Thank you also to Drs. Roberts-Wollman, Koutromanos, and Sarlo, whose support and expertise were greatly appreciated. I learned a great deal from you all and thank you for your guidance during the especially unique challenges faced this year.

Lastly, I would like to thank my family for their continued support. Finishing my degree and thesis from home during these challenging times was never something I anticipated, and I could not have done it without them.

TABLE OF CONTENTS

LIST OF FIGURES

LIST OF TABLES

Chapter 1. Introduction

This chapter provides an overview of the research motivation, major concepts, and project purpose. The first section describes the concepts of prestressed concrete and prestress losses to provide context for the research motivation. The second section provides a description of the Varina-Enon Bridge, concerns with the structure, and a brief summary of previous research work. The third section outlines the purpose and scope of the project.

1.1 Research Motivation

Prestressed concrete uses stressed steel strands to apply a precompression force to concrete structures. This can lead to lighter, stiffer, and more efficient construction. Prestressing strands can be stressed before the concrete is placed to create *pretensioned* structures. The steel strands can be stressed after the concrete is cast and hardened to construct *post-tensioned* concrete. Prestressed concrete is now a common method for all types of construction but has become an especially effective technique for bridges.

As infrastructure ages, it is important to be able to assess its remaining service life. One serviceability concern for prestressed concrete is *prestress losses*. Prestress losses occur when the steel strands lose tension force at the time of stressing as well as throughout the life of the structure. Prestress losses can lead to excessive deflections and cracking, which can allow ingress of moisture and subsequently corrosion of steel. In addition, for systems with *unbonded* tendons, prestress losses can negatively impact the flexural strength. One type of unbonded tendon is external to the concrete cross-section, so the forces are transferred only at the anchors and deviators rather than throughout the length of the prestressing strands. Quantifying prestress losses is critical for understanding the serviceability of a structure.

1.2 Varina-Enon Bridge Overview

The Varina-Enon Bridge is located on I-295 and spans the James River in southeastern Richmond, Virginia. It was designed by Figg and Muller Inc. and opened to traffic on July 18, 1990. The structure is a cable-stayed, segmental, precast, post-tensioned box girder bridge. As seen in Figure 1.1, the bridge consists of two parallel box girders carrying three northbound lanes and three southbound lanes. The bridge totals 4,680 ft in length and consists of 28 spans. 21 are *approach spans*, 6 are *transition spans*, and 1 is the *main span*.

Figure 1.1: Aerial View of Varina-Enon Bridge

1.2.1 Approach Span Units

The approach spans are each 150 ft in length and consist of seven 20-ft precast *typical segments* between the piers. Nine-ft long *pier segments* are installed at the locations over the piers. The joints between the typical segments are epoxied, and the spans are completed with six-inch cast-in-place closure joints on either side of the pier segments. Figure 1.2 provides an example of an approach span unit. Pictured are approach Spans 1 through 6, which start at Abutment 1 and end at the first expansion joint located over Pier 7.

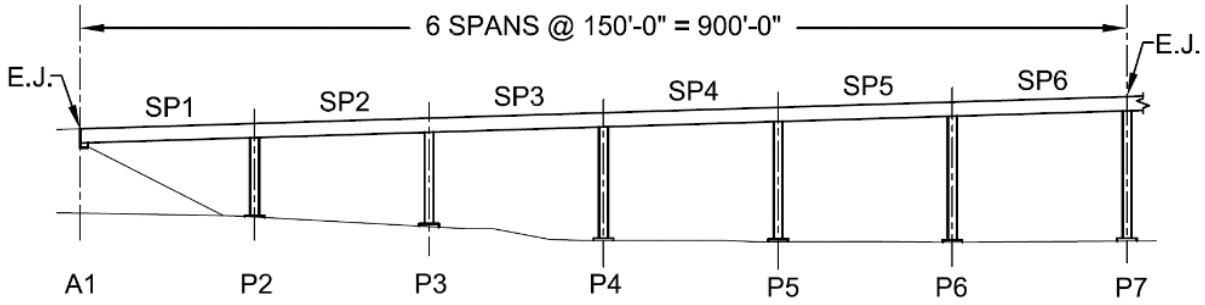

Figure 1.2: Elevation of Approach Spans 1-6 (Lindley 2019, with permission)

The dimensions of the typical and pier segments are shown in Figure 1.3 and Figure 1.4. Each box girder contains transverse internal post-tensioning. As seen in Figure 1.3 and Figure 1.4, the pier segments have the same outer dimensions as the typical segments but contain diaphragms on the interior. These diaphragms enclose additional transverse internal post-tensioning and accommodate the anchors for the longitudinal tendons.

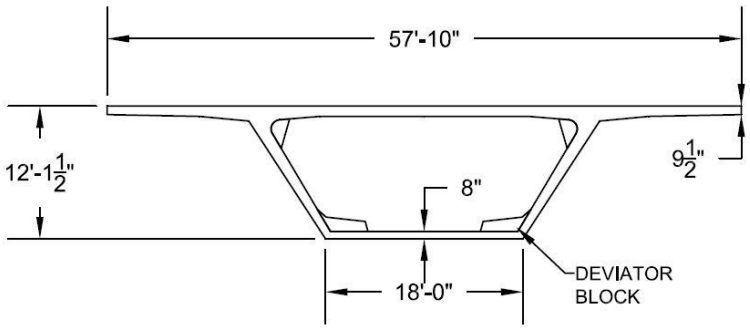

Figure 1.3: Typical Segment Dimensions (Lindley 2019, with permission)

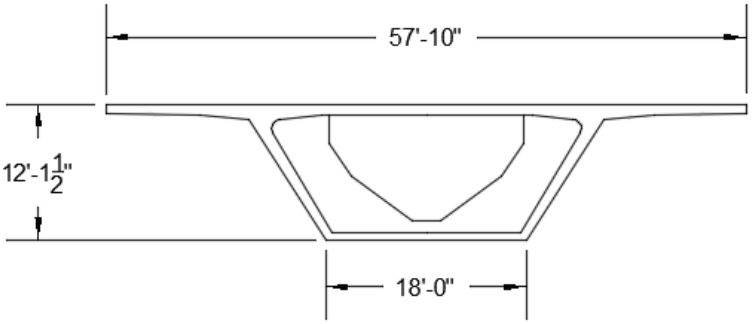

Figure 1.4: Pier Segment Dimensions

Each approach span has external longitudinal post-tensioning consisting of eight tendons located in the hollow interior of the segments. Each tendon contains 19 each 0.6 in. diameter strands. An example post-tensioning layout is shown for Span 6 in Figure 1.5. The tendons are grouted in ducts that run through the deviator blocks seen in Figure 1.5 and Figure 1.3. Figure 1.5 also shows that the tendons overlap over the piers, providing continuity between the spans. Design drawings for all approach span longitudinal post-tensioning layouts can be found in Appendix A.

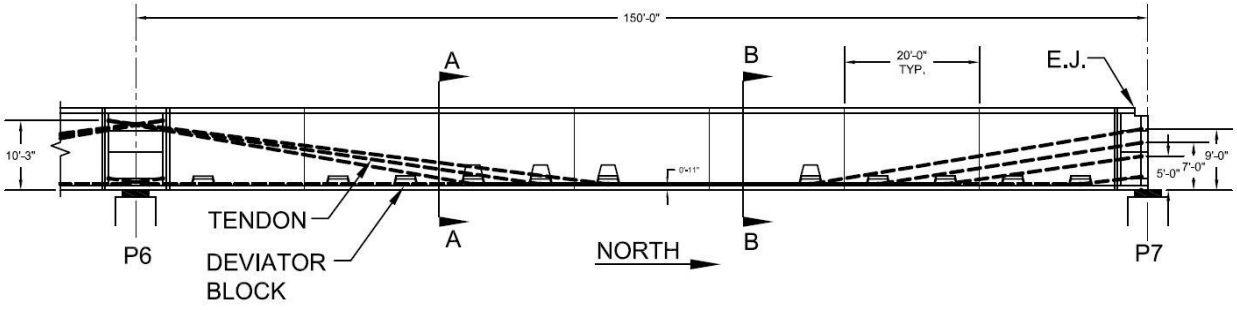

Figure 1.5: Longitudinal Post-Tensioning Layout in Span 6 (Lindley 2019, with permission)

1.2.2 Main Span Unit

The main span unit is the cable-stayed section of the bridge and can be seen in Figure 1.6. The main span unit consists of six transition spans that are similar to the approach spans in that they are each 150 ft long with 20-ft typical segments. The main span is the portion of the bridge that crosses the James River, and it is 630 ft long with 10-ft typical segments. This span was built with the cantilever method using a beam and winch system, beginning at Piers 16 and 17 and ending where the segments meet at midspan. See Appendix B for the original drawings outlining the construction process of the main span unit.

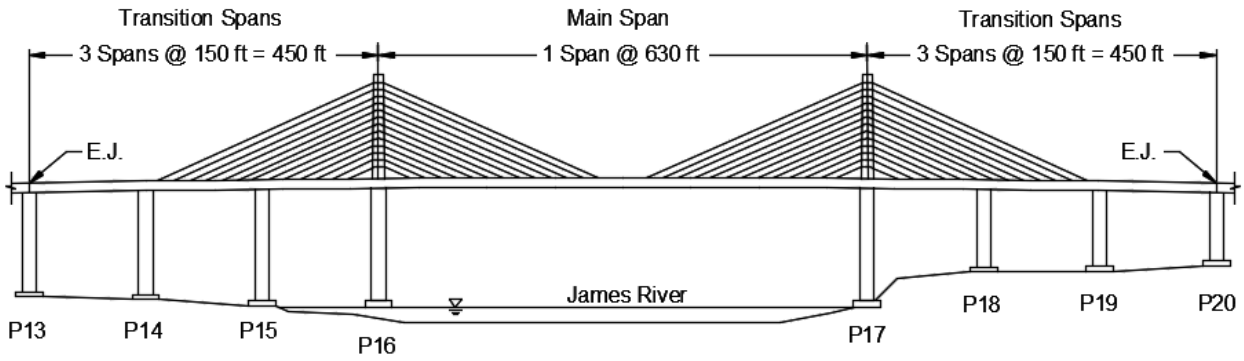

Figure 1.6: Elevation of Main Span Unit

The northbound and southbound sides of the main span unit are joined by a closure pour. At each location where a stay cable meets the superstructure, a *delta frame* distributes the stay force with a truss-like behavior. Each delta frame has internal transverse post-tensioning. Figure 1.7 shows the expected behavior of the delta frames under the stay force and dead load only.

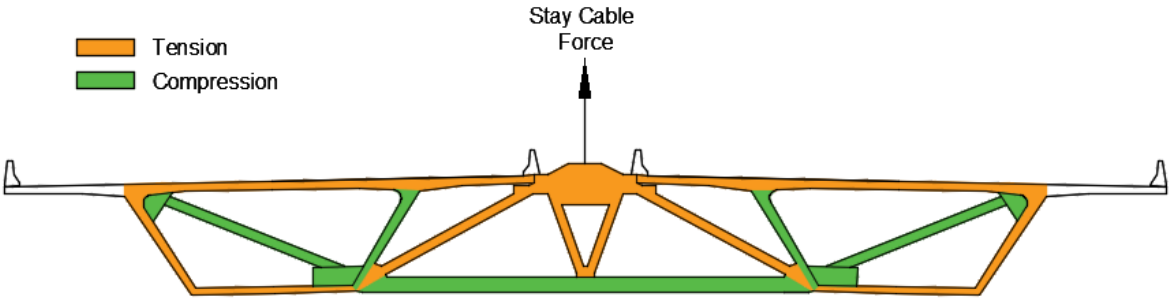

Figure 1.7: Delta Frame Behavior Under Stay Force and Self-Weight

The main span unit contains both internal and external longitudinal post-tensioning. The internal longitudinal post-tensioning runs through the top and bottom slabs of the box girders as well as through the

closure pour. The internal longitudinal tendons in the transition spans consist of 4 each 0.6 in. strands, while those in the main span and closure pour contain 12 each 0.6 in. strands. The transition spans have a similar harped external post-tensioning layout to that of the approach spans. These tendons consist of 19 each 0.6 in. strands. The main span has a unique external longitudinal post-tensioning layout as seen in Figure 1.8. These tendons contain 12 each 0.6 in. strands. The stay cables consist of 0.6 in. strands varying in number from 80 to 90. Design drawings for all main span unit external and internal longitudinal post-tensioning layouts can be found in Appendix A.

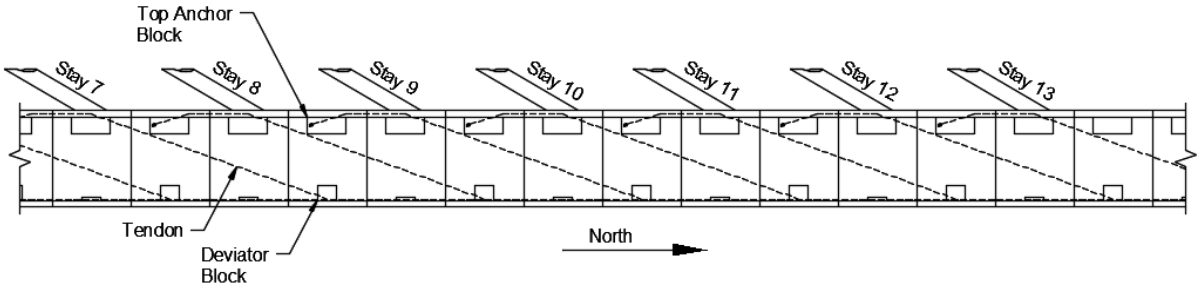

Figure 1.8: Longitudinal External Post-Tensioning Layout in Main Span 16

1.2.3 Project Background

In July 2012, inspectors visually observed the joint in the bottom flange at Section A-A in Figure 1.5 opening up to 1/16 in. under heavy traffic loads. This could indicate unanticipated high levels of tension in the bottom flange that would not be expected for a heavily prestressed structure. While this could partially be attributed to large *thermal gradients*, or the temperature difference throughout the depth of the segments, it could also indicate larger than expected prestress losses.

Several studies have previously been conducted to evaluate the crack-opening behavior at the joint in Span 6 of the Varina-Enon Bridge. Maguire et al. (2014) installed a long-term monitoring system to measure the joint opening as well as the thermal gradient at that location. It was concluded that crack openings are greatly influenced not just by heavy traffic, but by the interaction of these loads with large thermal gradients. In 2017, a study was conducted evaluate the effective prestress force in Span 6 using the data collected at the opening joint. The results of this study were not published. Lindley (2019) reinstalled the original long-term monitoring system and refined the effective prestress evaluation in Span 6. These previous research projects are discussed in greater detail in the Literature Review.

1.3 Purpose and Scope

The purpose of this research project is to estimate longitudinal prestress losses using field data from flexural crack openings at several locations throughout the bridge and compare these values to those

obtained from a finite element model of the full structure. This purpose can be broken down into the following scope:

- Estimate the longitudinal effective prestress force in multiple spans from field data collected at joint openings.
- Develop a finite element model of the full structure. For this thesis, it will be used evaluate predicted prestress losses using standard models for creep and shrinkage. The model will be used by future researchers to investigate other aspects of behavior of the bridge, such as response to superloads.
- Monitor, maintain, and expand instrumentation on the Varina-Enon Bridge.
- Provide recommendations for continued research on the Varina-Enon Bridge.

Chapter 2. Literature Review

Extensive research has been conducted on several bridges that are similar to the Varina-Enon Bridge. In addition, there have been previous studies on the Varina-Enon Bridge itself. This chapter discusses the similar and previous work as it relates to this project. The chapter is broken down into the four major concepts of computer modeling, creep and shrinkage, prestress losses, and thermal gradient. A general overview is provided for each concept, and then the methods utilized by previous researchers to address these topics are discussed.

2.1 Computer Modeling

Finite element models of structures are powerful tools in the design process but can also be useful for analysis of existing structures. Finite element analysis software enables the user to input the geometry, material properties, and loading of a structure in order to obtain a mathematical response of the system. Environmental loads such as temperature and time-dependent effects such as creep and shrinkage may also be included in a model. The mathematical response of a system from a finite element analysis includes valuable information such as member stresses, strains, and deflections.

2.1.1 Veterans' City Glass Skyway Modeling

The Veterans' Glass City Skyway (VGCS) is a precast, segmental concrete bridge similar to the Varina-Enon Bridge. The VGCS was known as the Maumee River Crossing until it opened to traffic in 2007. It is located on I-280 in Toledo, Ohio and carries three lanes of traffic in each direction. The VGCS consists of 56 approach spans totaling 7,273 ft and one cable-stayed main span totaling 1,525 ft (Helmicki et al. 2012). Figure 2.1 provides a view of the bridge that shows where it crosses the Maumee River.

Figure 2.1: Artistic Rendering of Veterans' Glass City Skyway (Helmicki et al. 2012, public domain)

A three-dimensional finite element model was created for the VGCS main span using LARSA 4D. An overview of the model is shown in Figure 2.2. Although cable-stayed bridges are generally highly nonlinear in terms of deformations and dynamic effects, the arrangement of the box girders and delta frames make the VGCS very stiff. Therefore, linear behavior was assumed for the model. It was also assumed that the delta frames do not contribute to the longitudinal stiffness of the structure. Another assumption was that the elastomeric bearings at the superstructure to substructure connections only contribute to vertical stiffness. Elastomeric bearing stiffness was neglected in the longitudinal, transverse, and rotational directions (Helmicki et al. 2012).

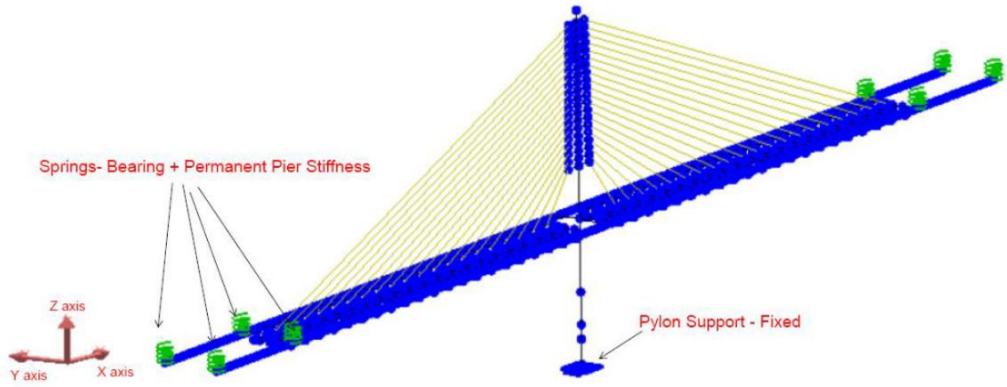

Figure 2.2: VGCS Main Span Finite Element Model (Helmicki et al. 2012, public domain)

The three types of elements in the finite element model were beam elements, cable elements, and spring elements. Cable elements were used to model the cable stays. Although in reality the stays for the VGCS are continuous through a cradle over the pylon, they were represented in the model as two separate stays stressed simultaneously. Cable elements have stress stiffening properties that require nonlinear analysis. However, since the self-weight of the bridge is so high, it is expected that the cables will always be in tension and there would never be a live load large enough to reverse the stresses. Therefore, stress stiffening properties of the cables were ignored. Spring elements were used to model the elastomeric bearing and pier compressive stiffnesses. The box girders and delta frame members were modeled as beam elements (Helmicki et al. 2012). The arrangement of delta frame elements is shown in Figure 2.3.

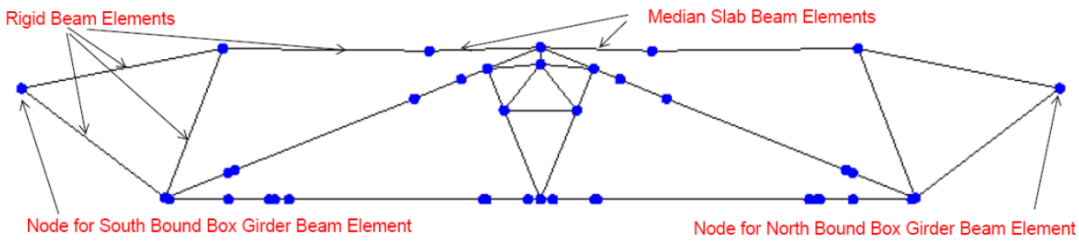

Figure 2.3: VGCS Delta Frame in Finite Element Model (Helmicki et al. 2012, public domain)

Some VGCS box girders were instrumented with strain gages during casting, allowing for *progressive calibration*. Progressive calibration is calibration of a finite element model against construction loads for intermediate construction stages. Both dynamic load tests using segment haulers and static load tests using cranes were conducted, and the measured strains were compared to those predicted by the model. The model was further validated by conducting a truck test on the completed VGCS and comparing the analytically obtained values to the measured data. Electrical-resistance strain gages were used to collect data from dynamic truck tests, while both vibrating wire and electrical-resistance strain gages collected data for static truck tests. An *influence line* was obtained from dynamic truck tests that could be compared to the results of an influence line analysis in the model. The locations of maximum response were also compared (Helmicki et al. 2012).

The delta frame model was calibrated separately before being included in the full finite element model, also using progressive calibration. Strains in delta frame members were measured during initial and final post-tensioning and compared to the model predictions. A stress-to-strain transformation was used to convert the stresses predicted by the model to values of strain that could be compared to the measured data. It was concluded that a finite element model created using LARSA 4D accurately represented the expected behavior of the VGCS (Nimse et al. 2015).

2.1.2 Varina-Enon Bridge Modeling

LARSA 4D was also used by Lindley (2019) to create a three-dimensional finite element model of the northbound approach Spans 1-6 of the Varina-Enon Bridge. An overview of this model can be seen in Figure 2.4. The model utilized beam elements for the box girders and piers, and spring elements for the neoprene bearing pads at the connections from the superstructure to substructure. Referencing the axes defined in Figure 2.4, the springs had translational stiffness in the Z and X-directions, and rotational stiffness about the Y-axis. The springs were modeled as fixed for the remaining three degrees of freedom. The spring stiffness values utilized were validated by live load tests conducted by Maguire et. al (2014). The longitudinal external post-tensioning tendons were included in the model, as well as the self-weights of the tendon deviator blocks and barrier rails. The finite element model was validated using deflection data collected from live load tests conducted by Maguire et al. (2014). The deflections measured due to different load configurations were compared to the deflections predicted by the model under those loadings, and were found to match reasonably well (Lindley 2019).

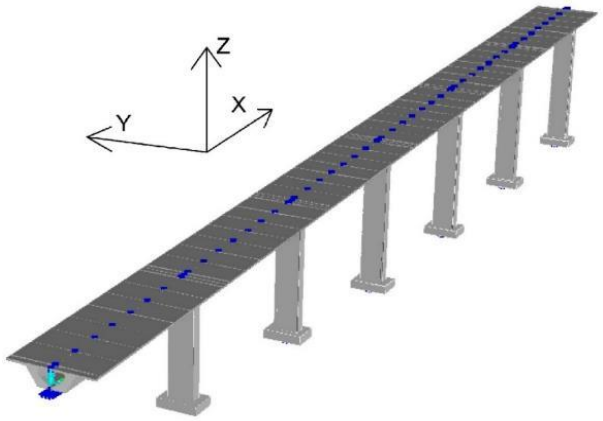

Figure 2.4: Isotropic View of Varina-Enon Bridge Approach Spans 1-6 FE Model (Lindley 2019, with permission)

2.2 Creep and Shrinkage

Creep is the long-term deformation of a structure due to a sustained load, and shrinkage is the volume change of material due to moisture losses. It is necessary to quantify creep and shrinkage effects in order to investigate long-term prestress losses. Stresses and strains due to creep and shrinkage are generally modeled as increasing over time and approaching an asymptotic value, as shown in Figure 2.5. The figure also demonstrates that after the time of unloading, there is recovery of all elastic strain and some creep strain. Various creep and shrinkage models exist such as CEB-FIP ’78, CEB-FIP ’90, ACI 209, AASHTO, and B3. Each model accounts for material properties and environmental conditions, but uses different functions to quantify the progression of creep and shrinkage over time (Lindley 2019). For a detailed overview of each of these models and how they differ, see Lindley (2019).

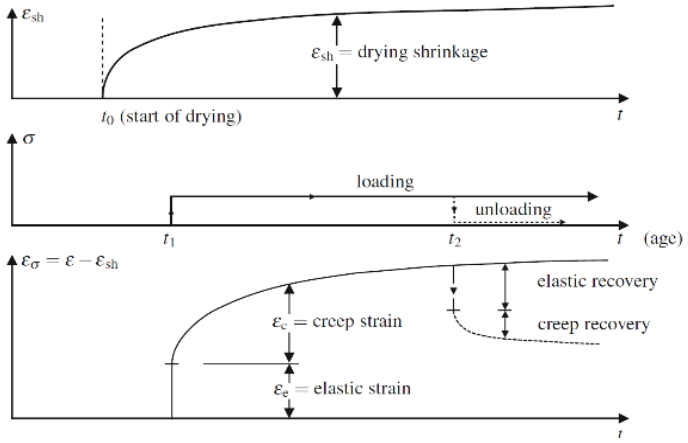

Figure 2.5: Creep and Shrinkage Strains Over Time (reprinted by permission from Springer Nature Customer Service Centre GmbH: Springer Nature Basic Properties of Concrete Creep, Shrinkage, and Drying by Bažant and Jirásek 2018)

2.2.1 Sunshine Skyway Bridge Creep and Shrinkage Models

The Sunshine Skyway Bridge is a prestressed, concrete, cable-stayed bridge located on I-275 in Florida. It is composed of four types of spans including trestle approach spans, low-level approach spans, high-level approach spans, and three cable-stayed spans. The trestle approach spans consist of standard prestressed I-girders, the low-level approach spans are comprised of twin box girders, and the high-level approach spans contain a single-cell box girder. The main cable-stayed spans consist of single-cell precast box segments (Shahawy and Arockiasamy 1996a). An elevation view of the main cable-stayed span of the bridge can be seen in Figure 2.6.

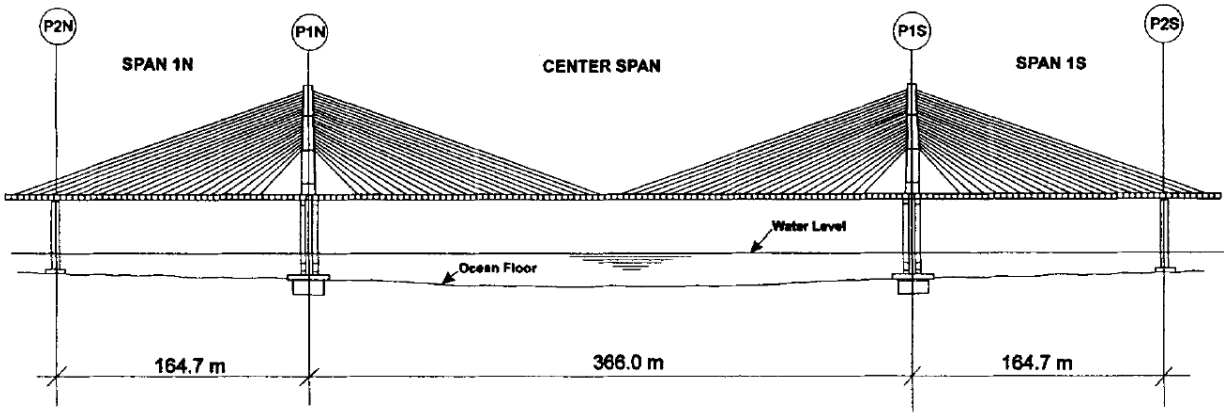

Figure 2.6: Elevation View of Sunshine Skyway Bridge (Shahawy and Arockiasamy 1996b, with permission from ASCE)

Shahawy and Arocklasamy (1996) conducted a study to develop an analytical model to predict time-dependent strain histories throughout all construction stages of the Sunshine Skyway Bridge. Box girders in the main span as well as the pylons were instrumented with strain gages, and the collected data was used to calibrate the analytical computer model. The age-adjusted effective-modulus method was used to compute the time-dependent creep and shrinkage strains. This method includes an aging coefficient that accounts for the effect of aging on the ultimate value of creep after the application of a load. There is also a correction factor accounting for ambient relative humidity, volume to surface ratio, and temperature. An iterative process was used to analyze the stresses and strains in the concrete sections after each construction stage of the Sunshine Skyway Bridge. The loading changed in each construction stage, so the aging coefficient changed as well. However, the study showed that time-dependent strains due to the construction sequence based on a constant aging coefficient aligned closely with those considering a varying aging coefficient. Therefore, a constant aging coefficient was determined to be adequate for analysis (Shahawy and Arockiasamy 1996b).

2.2.2 Varina-Enon Bridge Creep and Shrinkage

As mentioned in the Introduction, Lindley (2019) studied the prestress losses in Span 6 of the Varina-Enon Bridge. Predicted prestress losses were evaluated from the finite element model considering three different creep and shrinkage models: CEB-FIP '78, CEB-FIB '90, and AASHTO. Although the bridge was designed under the CEB-FIB '78 model code, it was found that the theoretical effective prestress using CEB-FIP '90 most closely matched the calculated effective prestress from field data (Lindley 2019). Therefore, for the purposes of this thesis, CEB-FIP '90 is used to quantify the creep and shrinkage effects of the structure over time.

2.2.3 CEB-FIP '90 Creep and Shrinkage Model

The CEB-FIP '90 model code was published by the Comité Euro-International Du Béton in 1990 as an update to the CEB-FIP '78 model code. In this model, creep and shrinkage are represented as a hyperbolic change over time. The ultimate values are corrected for mixture proportions and environmental conditions. The parameters required for the model include the age of the concrete when drying starts, the age of the concrete at loading, the mean 28-day compressive strength, the relative humidity, the volume-surface ratio of the member, and the cement type (ACI 209 2008). The CEB-FIP '90 calculations for creep and shrinkage per ACI 209 (2008) are subsequently described. All units are in terms of lb. and in.

The creep effect is defined by the compliance function given by Equation (2-1), which describes the total stress-dependent strain per unit stress.

$$J(t,t_o) = \frac{1}{E_{cmto}} + \frac{\Phi_{28}(t,t_o)}{E_{cm28}} \qquad (2\text{-}1)$$

E_{cmto} is the modulus of elasticity at the time of loading t_o, calculated with Equation (2-2).

$$E_{cmt} = E_{cm28} exp\left[\frac{s}{2}\left(1 - \sqrt{\frac{28}{t/t_1}}\right)\right] \qquad (2\text{-}2)$$

t_1 = 1 day, and s is a value dependent on the type of cement and compressive strength of concrete taken from Table 2.1.

Table 2.1: Coefficient s Based on Cement Type and Compressive Strength (ACI 209 2008, with permission)

f_{cm28}	Type of cement	s
≤60 MPa (8700 psi)	RS (rapid hardening high-strength cement)	0.20
	N or R (normal or rapid hardening cements)	0.25
	SL (slowly-hardening cement)	0.38
>60 MPa (8700 psi)*	All types	0.20

*Case not considered in CEB MC90.

E_{cm28} is the mean 28-day modulus of elasticity calculated with Equations (2-2) and (2-3).

$$E_{cm28} = \alpha_E 3{,}118{,}310_3 \sqrt{\frac{f_{cm28}}{f_{cmo}}} \qquad (2\text{-}2)$$

$$f_{cm28} = f'_c + 1160psi \qquad (2\text{-}3)$$

f_{cmo} is taken as 1450 psi, and α_E is a value dependent on the aggregate type taken from Table 2.2. f'_c is the compressive cylinder strength defined as the strength below which only 5% of all possible strength measurements may be expected to fall.

Table 2.2: Effect of Aggregate Type on Modulus of Elasticity (ACI 209 2008, with permission)

Aggregate type	α_E
Basalt, dense limestone aggregates	1.2
Quartzitic aggregates	1.0
Limestone aggregates	0.9
Sandstone aggregates	0.7

Φ_{28} is the 28-day creep coefficient calculated in Equations (2-4) through (2-10), which gives the ratio of the creep strain at the time of loading t_o, to the elastic stress due to a constant stress applied at 28 days.

$$\Phi_{28}(t, t_o) = \Phi_o \beta_c (t - t_o) \qquad (2\text{-}4)$$

$$\Phi_o = \Phi_{RH}(h)\beta(f_{cm28})\beta(t_o) \qquad (2\text{-}5)$$

$$\Phi_{RH}(h) = \left[1 + \frac{1 - h/h_0}{\sqrt[3]{0.1[(V/S)/(V/S)_0]}}\alpha_1\right]\alpha_2 \qquad (2\text{-}6)$$

$$\beta(f_{cm28}) = \frac{5.3}{\sqrt{f_{cm28}/f_{cmo}}} \qquad (2\text{-}7)$$

$$\beta(t_o) = \frac{1}{0.1 + (t_o/t_1)^{0.2}} \qquad (2\text{-}8)$$

$$\alpha_1 = \left[\frac{3.5 f_{cmo}}{f_{cm28}}\right]^{0.7} \qquad (2\text{-}9)$$

$$\alpha_2 = \left[\frac{3.5 f_{cmo}}{f_{cm28}}\right]^{0.2} \qquad (2\text{-}10)$$

h is the ambient relative humidity in decimals, $h_o = 1$, V/S is the volume-surface ratio, and $(V/S)_o = 2$ in. The coefficient $\beta_c(t\text{-}t_o)$ describes the development of creep over time after loading and can be calculated with Equations (2-11) through (2-13).

$$\beta_c(t - t_o) = \left[\frac{(t - t_o)/t_1}{\beta_H + (t - t_o)/t_1}\right]^{0.3} \qquad (2\text{-}11)$$

$$\beta_H = 150[1 + (1.2h/h_o)^{18}](V/S)/(V/S)_o + 250\alpha_3 \leq 1500\alpha_3 \qquad (2\text{-}12)$$

$$\alpha_3 = \left[\frac{3.5 f_{cmo}}{f_{cm28}}\right]^{0.5} \quad (2\text{-}13)$$

In order to determine shrinkage effects, the total shrinkage strains are calculated from Equation (2-14).

$$\varepsilon_{sh}(t, t_c) = \varepsilon_{cso}\beta_s(t - t_c) \quad (2\text{-}14)$$

t is the age of the concrete (days) at the time of interest, and t_c is the age of the concrete (days) at the beginning of drying. ε_{cso} is the notional shrinkage coefficient obtained from equations (2-15) through (2-18).

$$\varepsilon_{cso} = \varepsilon_s(f_{cm28})\beta_{RH}(h) \quad (2\text{-}15)$$

$$\varepsilon_s(f_{cm28}) = [160 + 10\beta_{sc}(9 - f_{cm28}/f_{cmo})]10^{-6} \quad (2\text{-}16)$$

$$\beta_{RH}(h) = -1.55\left[1 - \left(\frac{h}{h_o}\right)^3\right] \; for \; 0.4 \leq h < 0.99 \quad (2\text{-}17)$$

$$\beta_{RH}(h) = 0.25 \; for \; h \geq 0.99 \quad (2\text{-}18)$$

The coefficient β_{sc} depends on the type of cement and can be taken from Table 2.3.

Table 2.3: Coefficient Based on Type of Cement (ACI 209 2008, with permission)

Type of cement according to EC2	β_{sc}
SL (slowly-hardening cements)	4
N and R (normal or rapid hardening cements)	5
RS (rapid hardening high-strength cements)	8

$\beta_{sc}(t\text{-}t_c)$ gives the development of shrinkage with time and is given by Equation (2-19).

$$\beta_s(t - t_c) = \left[\frac{(t - t_c)/t_1}{350[(V/S)/(V/S)_o]^2 + (t - t_c)/t_1}\right]^{0.5} \quad (2\text{-}19)$$

2.3 Prestress Losses

As mentioned in the Introduction, prestress losses are the loss of tension force in prestressing strands. Total prestress losses are the summation of immediate and time-dependent losses, as shown in Equation (2-20) (Lindley 2019). Immediate prestress losses include those due to seating and friction (Δf_{pFS}) as well as elastic shortening (Δf_{pES}). Of greater concern are time-dependent prestress losses which include those due to creep (Δf_{pCR}) and shrinkage (Δf_{pSH}) of the concrete as well as relaxation of the steel strands (Δf_{pRE}). Time-dependent effects can be difficult to predict but are critical for quantifying prestress losses and understanding the serviceability of a structure.

$$\Delta f_{pT} = \underbrace{\Delta f_{pFS} + \Delta f_{pES}}_{\text{Short-term losses}} + \underbrace{\Delta f_{pCR} + \Delta f_{pSH} + \Delta f_{pRE}}_{\text{Long-term losses}} \qquad (2\text{-}20)$$

Several methods have been developed for calculating long-term prestress losses with varying degrees of accuracy. The lump-sum method depends only the level of stress in the steel and concrete. Another simplified method estimates the long-term losses due to creep, shrinkage, and relaxation individually using factors dependent on the type of concrete, age at loading, and type of prestressing steel. The most accurate methods are time-step methods and age-adjusted effective modulus methods, which directly consider the creep, shrinkage, and relaxation models for the materials being used. These methods for calculating long-term prestress losses are outlined in ACI 423.10R *Guide to Estimating Prestress Losses* (ACI 423 2016), and described in greater detail by Lindley (2019).

2.3.1 Varina-Enon Bridge Prestress Losses

As mentioned in the Introduction and Section 2.2.2, Lindley (2019) studied prestress losses in Span 6 of the northbound side of the Varina-Enon Bridge. Data collected from the joint opening at Section A-A in Figure 1.5 was used to determine the effective prestress force at that location. The effective prestress force was back-calculated from both 2013 and 2019 field data based on the assumption that there is zero stress at the location of the crack when it opens. The finite element model described in Section 2.1.2 was used to obtain predicted prestress losses that could be compared to those calculated from field data. In 2013 the average prestress loss was calculated as 47.3 ksi, while the model employing the CEB-FIP ’90 model for creep and shrinkage predicted losses of 43.3 ksi. Therefore, the actual prestress losses were determined to be 8.4% greater than those predicted by the model (Lindley 2019).

2.4 Thermal Gradient

As mentioned in the Introduction, *thermal gradients* are the temperature differences throughout the depth of a structure. Figure 2.7 shows that this temperature distribution is affected by several environmental factors including solar radiation, ambient temperature, wind, and humidity (Xu et al. 2019). Large box girders develop thermal gradients since the wide top flange is exposed to solar radiation, but shades the webs and bottom flange (Lindley 2019).

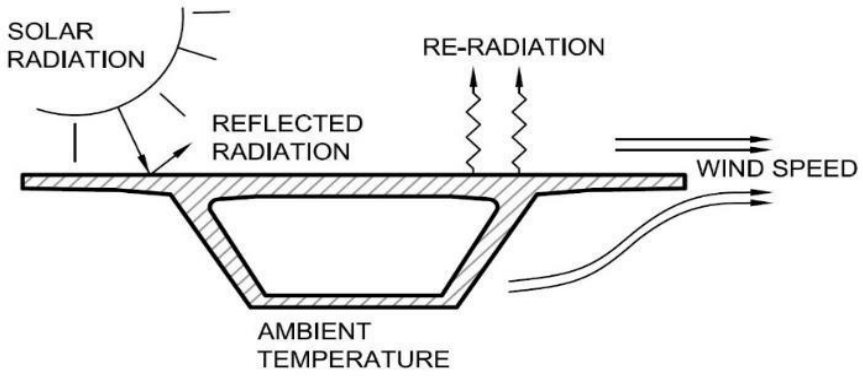

Figure 2.7: Environmental Factors Affecting Thermal Gradients (Lindley 2019, with permission)

Non-linear thermal gradients tend to develop in bridges such as the Varina-Enon Bridge on days with large temperature fluctuations. This induces two types of internal stress: *self-equilibrating stress* and *continuity stress*. Self-equilibrating stresses are the stresses induced when considering a simply supported configuration. Continuity stresses arise from the effects of the non-linear thermal gradient on the redundant structure (Lindley 2019). Table 2.4 summarizes the types of temperature induced thermal stresses. For a more detailed description of the concepts related to thermal gradient, see Lindley (2019). See Sections 3.4.6 and 3.4.7 of this thesis for descriptions of the calculations for self-equilibrating stress and continuity stress.

Table 2.4: Summary of Temperature Induced Thermal Stresses (Lindley 2019, with permission)

	Determinate	Indeterminate
	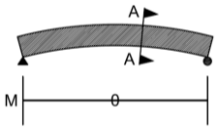	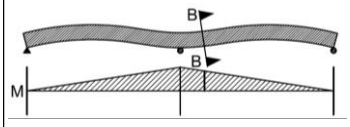
Linear Thermal Gradient 	Stresses @ A-A 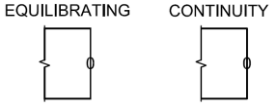	Stresses @ B-B 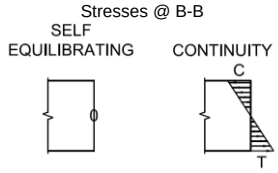
Non-Linear Thermal Gradient 	Stresses @ A-A 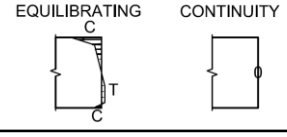	Stresses @ B-B 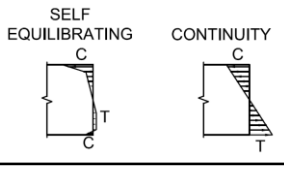

2.4.1 Veterans' Glass City Skyway Thermal Gradient

Helmicki et al. (2012) conducted a study on the thermal gradient within the concrete box girders of the Veterans' Glass City Skyway. Both *positive thermal gradients* and *negative thermal gradients* were considered. Positive thermal gradients occur when the top of the cross section is at a higher temperature

than the middle and bottom, while negative thermal gradients occur when the top of the cross section is at a lower temperature than the middle. Negative thermal gradients are of particular concern because they can lead to cracking of the top slab, allowing ingress of moisture that could corrode reinforcing steel and prestressing strands (Helmicki et al. 2012).

The purpose of the thermal gradient study on the VGCS was to assess if the actual thermal gradients are consistent with the AASHTO design code. Table 2.5 shows several AASHTO positive and negative design gradients for various years. Eight full months of temperature data were collected using thermistors embedded in the box girders of the VGCS. The positive thermal gradient was determined to be consistent in shape throughout the eight months of the study. In addition, it was found that the positive gradients typically fell within the AASHTO design code. Only two months of data showed occurrences of negative thermal gradients, indicating that the issues associated with them are not a large concern. The negative gradients were not as consistent in shape as the positive gradients, but they still typically fell within the AASHTO design code (Helmicki et al. 2012).

Table 2.5: AASHTO Design Gradients

Design Code	AASHTO 89	AASHTO 94	AASHTO 98
Positive Gradients	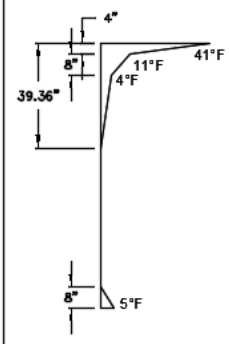	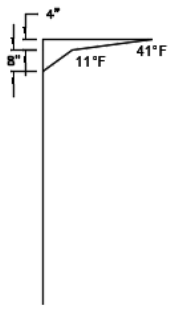	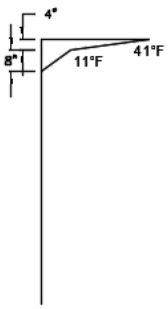
Negative Gradients	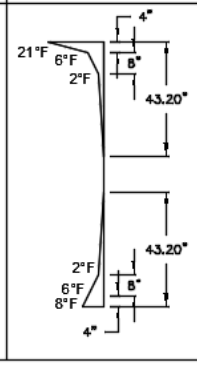	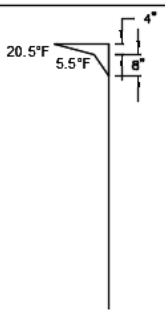	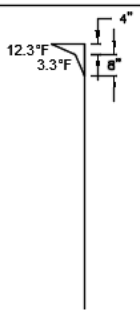

2.4.2 Sunshine Skyway Bridge Thermal Gradient

Six bridge segments of the Sunshine Skyway Bridge were each instrumented with 28 thermocouples to measure the temperature in the bridge superstructure. The thermocouples were clustered

into seven groups throughout the depths of the box sections, each with four thermocouples. The pylons were also instrumented with 14 thermocouples to measure temperature distributions across their major and minor axes (Shahawy and Arockiasamy 1996a). It was found that nonlinear thermal gradients had a considerable effect on the total strain magnitude in the bridge segments. In some cases, high thermal strains doubled the magnitude of the total strain at certain locations in the cross-section (Shahawy and Arockiasamy 1996b).

2.4.3 Varina-Enon Bridge Thermal Gradient

Maguire et. al (2014) conducted a study on the thermal gradient of the Varina-Enon Bridge. Temperature data was collected using thermocouples installed throughout the depth of the box girder at Section A-A in Figure 1.5. The purposes of this study were to determine if the measured thermal gradient fell within the AASHTO design code, and to characterize the relationship between the thermal gradient and the observed joint opening at Section A-A in Figure 1.5.

The study concluded that the measured thermal gradient was the same shape as the design gradient, but significantly less severe in magnitude. The other key conclusion was that the crack opening in Span 6 is influenced by both heavy truck loads and large thermal gradients. As seen in Figure 2.8, there were more crack opening events, and the crack displacements were larger, in warmer months when the differential temperatures were generally greater. Cooler months had fewer and smaller crack openings (Maguire et al. 2014).

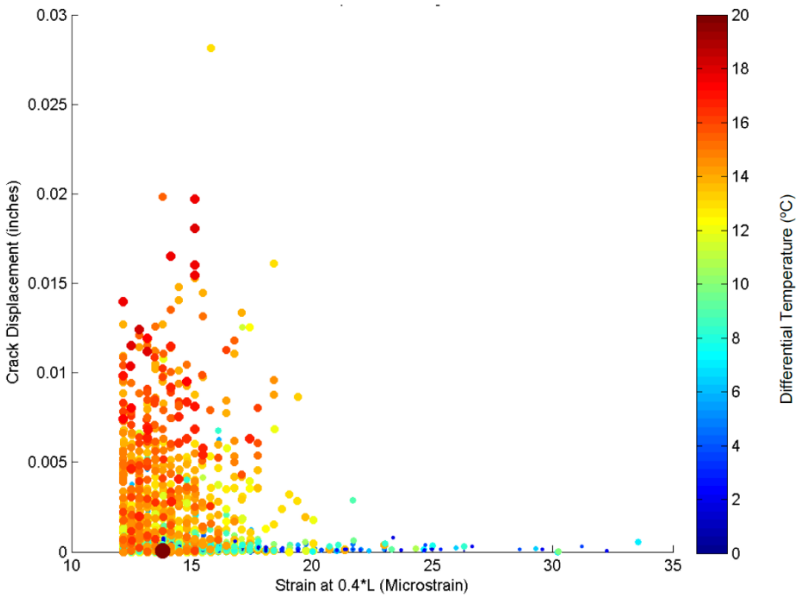

Figure 2.8: Crack-Temperature-Strain Plot for 2013 Crack Opening Events (Maguire et al. 2014, with permission)

2.5 Summary of the Literature

Finite element modeling has been used for multiple precast box girder bridges to predict the staged-construction and time-dependent behavior related to creep, shrinkage, and prestress losses. A model was created of the Veteran's Glass City Skyway and calibrated during various construction stages of the bridge to provide a baseline model that could be used for long-term monitoring. A model was created of the Varina-Enon Bridge in order to obtain predicted prestress losses and aid in calculations of prestress losses from measured data. In general, finite element models can be used to obtain valuable information regarding the behavior of a structure that can be used in conjunction with collected data for long-term monitoring.

The time-dependent effects of creep and shrinkage are important to quantify in order to understand a structure's long-term behavior and obtain predicted prestress losses. There are several different models that quantify creep and shrinkage strains over time. An analytical model was created for the Sunshine Skyway Bridge with time-dependent creep and shrinkage strains computed per the age-adjusted effective modulus method. Multiple creep and shrinkage models were used to predict prestress losses in the Varina-Enon Bridge, but it was concluded that the CEB-FIP '90 model provided the most accurate prediction.

Quantifying time-dependent prestress losses is critical for understanding the serviceability of a structure. Prestress losses in northbound Span 6 of the Varina-Enon Bridge were computed from measured data at the location of the observed joint opening. The calculated prestress losses were compared to the predicted prestress losses from the finite element model. Actual prestress losses were determined to be 8.4% greater than the losses predicted by the model.

Non-linear thermal gradients lead to the development of internal stresses in large box girders. The effects of thermal gradients have been studied for several precast, segmental, box girder bridges. A study on the VGCS determined that the measured thermal gradients fell within the AASHTO design code. Research on the Sunshine Skyway Bridge found that nonlinear thermal gradients had a considerable effect on the total strain magnitude in the bridge segments. A study on the Varina-Enon Bridge concluded that the measured gradient fell within the design code, and that greater thermal gradients lead to more and larger crack openings.

Chapter 3. Methodology

This chapter describes the processes and steps taken to fulfill the project purpose of estimating the effective prestress force from field data collected at multiple joint opening locations in the Varina-Enon Bridge and comparing the results to those obtained from a finite element model of the full structure. The first section describes how data was acquired from instrumentation in northbound Spans 5, 6, and 9. The second section explains how the data was processed to obtain key measurements of interest. The third section provides an overview of the computer model and describes how it took time-dependent effects into account. The fourth section details how the effective prestress forces were calculated from field data.

3.1 Data Acquisition

3.1.1 Spans 5 and 6 Instrumentation

The original long-term monitoring system was installed by Maguire et al. (2014) for the main purpose of measuring the crack opening and thermal gradient at the visually observed opening joint in Span 6. Instrumentation was also installed to monitor an opening joint in Span 5. This system was reinstalled by Lindley (2019) in order to continue research and evaluation of the effective prestress force. The sensors in this long-term monitoring system include Transtek linear variable differential transformers (LVDTs), Bridge Diagnostics Inc. (BDI) strain transducers, and thermocouples (TCs). Figure 3.1 shows the locations of the sensors in Span 6, and Figure 3.2 shows the locations of the sensors in Span 5.

The strain transducers measured lived load strains on the top of the bottom flange of the box girders. ST01 was installed at the location of the maximum expected live load moment in Span 6, Section B-B, which is 0.4 times the span length from Pier 7. This strain transducer served as the trigger gage for the data acquisition system since crack-opening events were expected to occur under large live loads. ST02 measured the strain at the top of the bottom flange adjacent to the opening joint in Span 6. The LVDTs at Section A-A in Figure 3.1 measured the crack displacement at the opening joint in Span 6. They were installed on the top of the bottom flange of the box girder as shown in Figure 3.3. Similarly, the LVDT at Section C-C was located on the top of the bottom flange of the box girder and measured the crack displacement at the opening joint in Span 5.

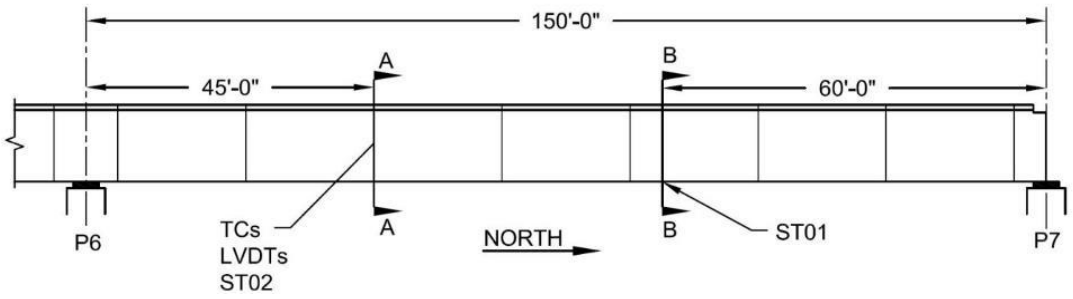

Figure 3.1: Sensor Layout in Span 6 (Lindley 2019, with permission)

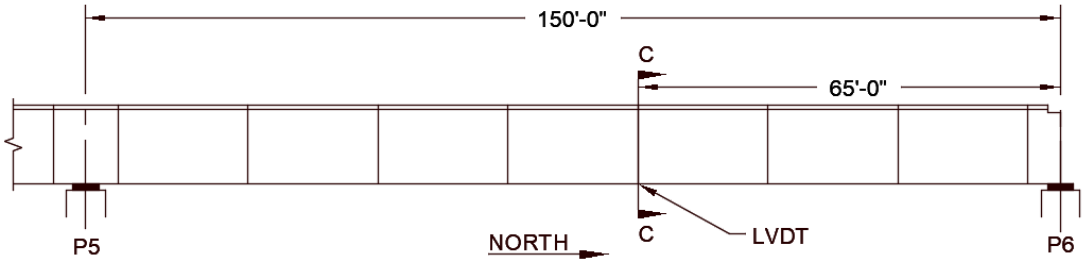

Figure 3.2: Sensor Layout in Span 5

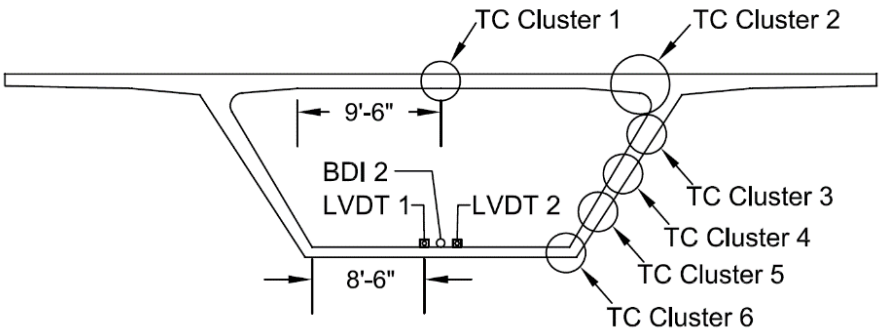

Figure 3.3: Section A-A Sensor Layout (Lindley 2019, with permission)

The thermocouples were installed in clusters throughout the depth of the box girder at Section A-A as shown in Figure 3.3. Each thermocouple had a tributary area over which the temperature was taken as constant. Several thermocouples were located at approximately the same depth in the section, so their temperature measurements were averaged and treated as one measurement. These thermocouples are grouped together in Table 3.1, which summarizes the location of each thermocouple from the top of the wearing surface, the tributary area, and the centroid of the area from the bottom of the section. The values from this table were used in the calculations of the self-equilibrating stresses in Section 3.4.6 and the thermal continuity forces in Section 3.4.7. It was assumed that the measured thermal gradient at Section A-A is representative of the thermal gradient along the full length of the Varina-Enon Bridge (Maguire et al. 2014).

Table 3.1: Thermocouple Locations and Tributary Areas (Lindley 2019, with permission)

TC	Elev. from top of wearing surface, in.	CG from the bottom, in.	Tot area, in.^{2}	Area*cg, in.^{3}
1	140.0	8.1	1,086.8	8,838.8
2	142.3	3.2	496.5	1,602.6
3	144.5	1.1	457.5	481.4
4,5	108.8	35.8	754.9	27,043.1
	110.8			
6,7	78.0	66.2	848.4	56,156.3
	80.6			
8,9	48.5	97.5	1,030.0	100,394.8
	51.1			
10	15.8	122.9	667.5	82,040.1
11	13.8	131.8	317.2	41,810.9
12	11.8	133.9	673.2	90,158.4
13	9.8	135.3	713.9	96,594.5
19	9.5	136.2	692.9	94,363.8
14	7.8	137.6	1,041.0	143,241.6
15	6.5	138.9	798.1	110,876.0
16,21	5.5	140.0	694.0	97,160.0
	5.5			
17,22	4.5	141.0	694.0	97,854.0
	4.5			
18,23	3.5	142.0	694.0	98,548.0
	3.5			
24	2.5	143.7	957.7	137,614.8
99	0.8	145.6	1,131.2	164,666.0

For more details regarding the types and locations of sensors installed in Spans 5 and 6 of the Varina-Enon Bridge, see Maguire et al. (2015) and Lindley (2019).

3.1.2 Span 9 Instrumentation

Another joint of interest in Span 9 was instrumented to monitor the crack-opening under heavy live loads and evaluate the effective prestress force in that span. The layout of the Transtek LVDTs and BDI strain transducers in Span 9 is shown in Figure 3.4. ST04 was located at Section E-E, the midspan and location of expected maximum live load moment in the span. ST04 served as the trigger gage for the data

acquisition system in Span 9. Section D-D was the location of the opening joint, where two LVDTs measured the crack displacement and ST03 measured the strain adjacent to the joint. This data acquisition system was installed with the intent of periodically moving it to different joints throughout the length of the bridge in order to monitor various crack-opening locations.

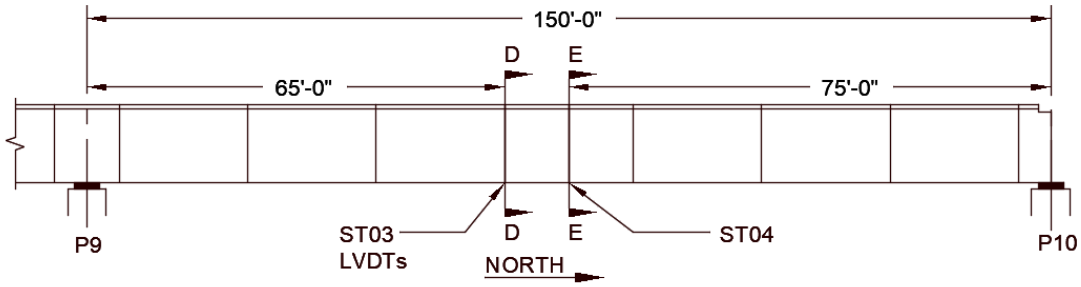

Figure 3.4: Sensor Layout in Span 9

3.1.3 Data Collection

The data from all sensors was collected using Campbell Scientific data acquisition systems. Two CR1000 dataloggers collected the data from the sensors in Spans 5 and 6. One collected the strain transducer and LVDT data at a 33 Hz sample rate for a 3.6 second event when the strain measurement from the trigger gage, ST01, exceeded 11 με. The other collected the thermocouple data at a continuous 2-minute sample rate. A CR1000X datalogger collected the strain transducer and LVDT data in Span 9 in the same manner as the CR1000 in Span 6. In this case, data was collected when the strain measurement from the trigger gage, ST04, exceeded 11 με. Three separate data files were downloaded from the dataloggers every 24 hours: one with strain transducer and LVDT data from Spans 5 and 6, one with thermocouple data from Span 6, and one with strain transducer and LVDT data from Span 9.

3.2 Data Processing

The data collected from the instrumentation throughout the Varina-Enon Bridge was processed using Matlab codes that matched the strain and displacement data for each "event" to the corresponding temperature data. "Bad" events were eliminated through a series of exclusionary criteria that ensured the trigger strain gages measured at least 11 με, and that the time difference between the strain and temperature measurements was less than 2 hours. Although the time difference would not be expected to be more than 2 minutes, this criterion was included because a difference of up to 2 hours would be considered acceptable. It was also ensured that the events were sufficiently short in length in case a trigger gage measurement drifted above the threshold value for an extended period of time. In addition, it was ensured there was not an unreasonable change in strain resulting from a "jump" in the strain measurements. A five-point moving average filter was used to remove noise from the data before each event was plotted and values of interest

were extracted. Sample plots of a crack-opening event in Spans 5 and 6 before and after the application of the moving average filter are shown in Figure 3.5 and Figure 3.6. Values of interest including the timestamp, maximum and minimum strains from the trigger gage, maximum crack displacement, and thermocouple readings were output into an Excel spreadsheet for each event. These spreadsheets were directly used for the effective prestress calculations from field data described in Section 3.4.

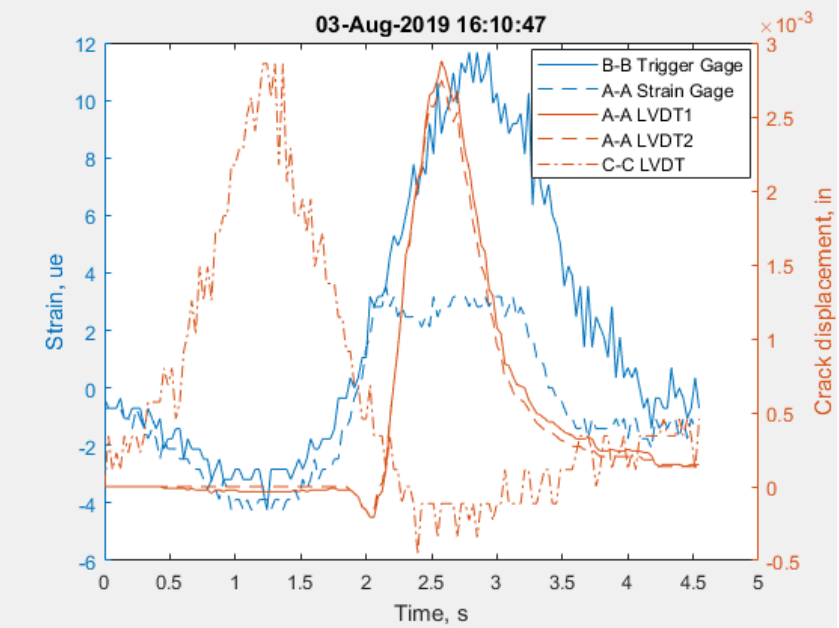

Figure 3.5: Sample Plot of Spans 5 and 6 Event Data Without Moving Average Filter

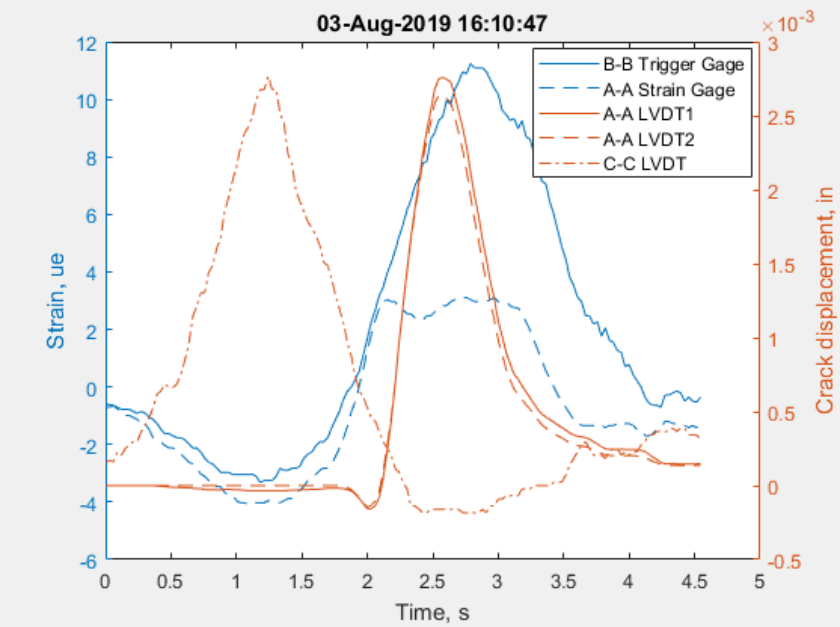

Figure 3.6: Sample Plot of Spans 5 and 6 Event Data With Moving Average Filter

3.3 Finite Element Model

3.3.1 Finite Element Model Overview

A finite element model was created of the full Varina-Enon Bridge using LARSA 4D and is shown in Figure 3.7. The bridge was modeled as two parallel box girders. All approach spans were modeled in a similar fashion to the model of approach spans 1-6 created by Lindley (2019) and described in Section 2.1.2. The only significant change was the boundary conditions of the springs representing the elastomeric bearings at the superstructure to substructure connections. Referencing the axes defined in Figure 3.7, the model created by Lindley (2019) represented the bearings with springs that had translational stiffness in the Z and X-directions, and rotational stiffness about the Y-axis. The springs were fixed, or *restrained* from movement, in the remaining three degrees of freedom. In the revised model, the springs were *constrained* in these remaining degrees of freedom. The constraints ensured that the box girder and pier cap at the superstructure to substructure connections must displace together in the directions in which the bearings did not provide stiffness.

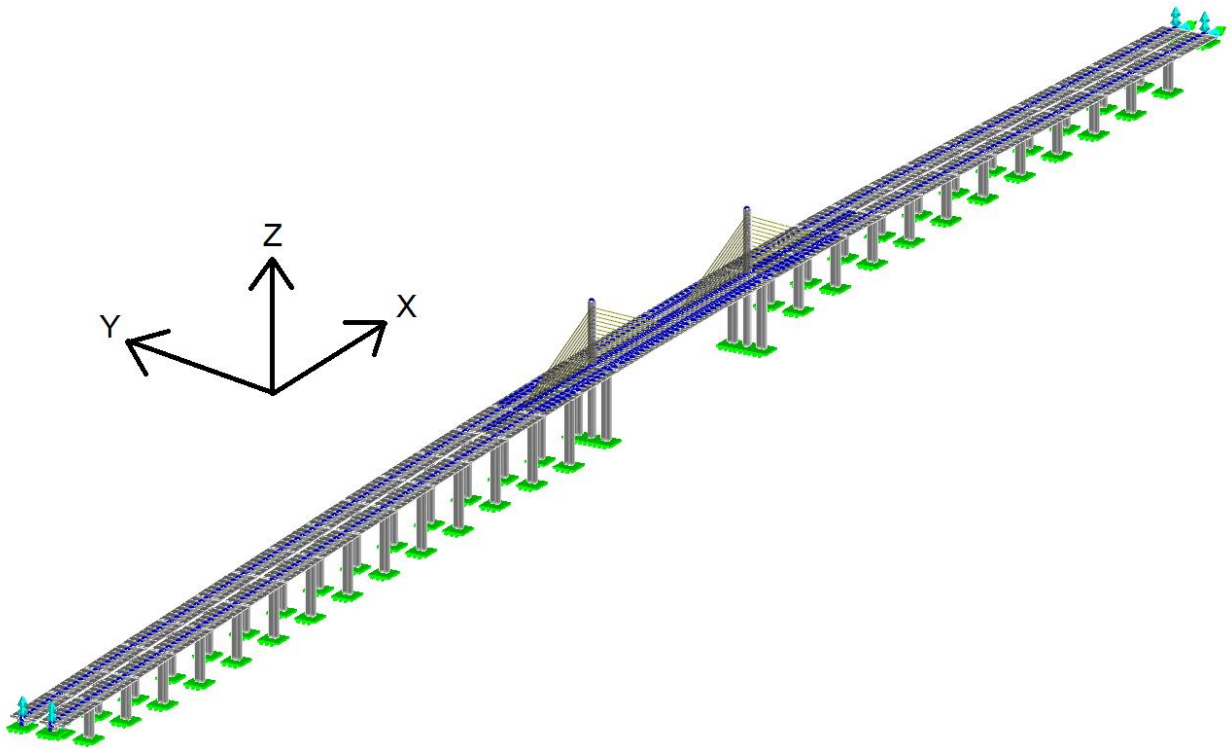

Figure 3.7: Isometric View of Varina-Enon Bridge Full FE Model

The main span unit, consisting of transition spans and a main span as described in Section 1.2.2, was modeled with beam elements, cable elements, spring elements, and truss elements. Beam elements were used to model the box girders, substructure, closure pour, and rigid links that provided connections

between various elements. Cable elements were used to model the cable stays in a similar fashion to the stays in the VGCS model (Helmicki et al. 2012). Although the stays are actually continuous through a cradle in the pylons, they were represented by two separate prestressed cable elements. Stress-stiffening properties were ignored since the large dead load of the bridge makes stress reversal due to live loads unlikely. Spring elements were used to model the pot bearings at each end of the main span. The value of translational stiffness in the Z-direction was taken from the description of a previous finite element model of the Varina-Enon Bridge main span unit (Lissenden 1988). The corresponding rotational stiffness about the Y-axis was calculated using dimensions of the elastomeric disc provided in design drawings. The springs were modeled as constrained in the remaining four degrees of freedom. Truss elements were used for delta frame members to account for the fact that the delta frames do not contribute to the longitudinal stiffness of the structure. A cross-section of the delta frame model is shown in Figure 3.8.

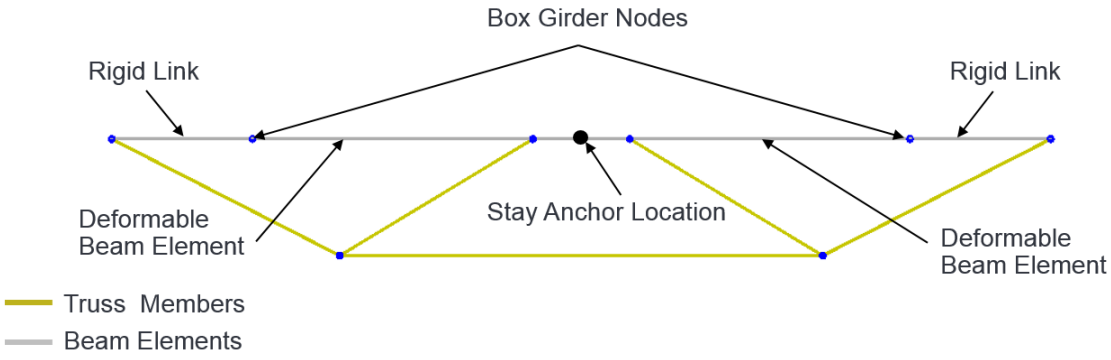

Figure 3.8: Cross Section of Delta Frame in FE Model

All longitudinal post-tensioning was included in the model using geometry and jacking forces from the design drawings in Appendix A. The material properties used in the finite element model are summarized in Table 3.2.

Table 3.2: Material Properties for Finite Element Model

Property	Value	Source
Concrete Elastic Modulus	5000 ksi	Verified by live load tests (Maguire et al. 2014)
Concrete Strength	6600 psi	Assumed
Tendon Tensile Strength	270 ksi	Design Drawings
Tendon Elastic Modulus	27,400 ksi	As-Built Testing (F&M Engineers 1993)

3.3.2 Staged Construction Analysis

A *time-dependent staged construction analysis* was used to represent the segmental construction of the Varina-Enon Bridge. This analysis accounted for the impact of the placement and stressing of each

span as well as the time-dependent effects due to creep, shrinkage, and relaxation. In this analysis, construction *stages* were broken down into *steps* and *activities*. Each stage represented one day of construction for the purposes of the time-dependent analysis. Each step represented an individual analysis and could be broken down into a series of activities. An activity could include placing an element, applying a load, or stressing a tendon (Lindley 2019).

The model contained 88 stages that each represented the construction of a span or a portion of a span of the Varina-Enon Bridge. The construction of approach spans and transition spans were each represented as one stage. The cantilever construction of the main span, Span 16, was broken up into 30 stages following the processes outlined in the original construction drawings in Appendix B. The activities included in the first step of each stage were adding the elements, applying the self-weight, and adding the dead loads due to guardrails, deviator blocks, and anchor blocks. The remaining steps were for stressing the longitudinal post-tensioning strands and/or cable stays. Each tendon was stressed in its own step so that the analysis accounted for elastic shortening losses. The cable stays were each stressed to an initial prestress force during the cantilever construction of the main span. All of the stays were restressed to their final prestress force in the 89th stage by adding duplicate cable elements with a prestress force equal to the difference between the final and initial prestress forces. The values of these jacking forces can be found in the original drawings in Appendix B. During the actual construction of the Varina-Enon Bridge, the stays were stressed from both ends simultaneously. This was accounted for in the model by representing each stay as two separate stays that met in the cradle and were stressed in the same step.

Each box girder was input into the model with a casting day in order to account for time-dependent effects. Day zero was defined as the day that the first box girder was cast, which was April 29, 1986. The 89 construction stages of the Varina-Enon Bridge took place from day 106 to day 1104. Empty construction stages were input in increments ranging from 200 to 1,000 days up until day 12,000. The empty stages served as time-steps for the time-dependent analysis (Lindley 2019). Day 2,000 represented the year 1992, and day 9,800 represented the year 2013. These stages were input so that the model could be validated using data from live load tests conducted by Duemmel et al. (1992) and Maguire et al. (2014), as discussed in Section 4.1. Day 12,000 represented the year 2019 so that the prestress losses predicted by the model could be compared with those calculated from 2019 and 2020 field data.

3.1.4 Prestress Losses

The finite element model incorporated both short-term and long-term prestress losses. As discussed in Section 2.3, short term prestress losses include those due to friction, seating, and elastic shortening losses. Friction losses arise from both *curvature friction* and *wobble friction*. Curvature friction results from the contact between the tendon and the duct when there is an intentional change in direction (Larsa 4D 2019).

The curvature friction coefficient, μ, was taken as 0.25 for the model since this value was measured during construction (F&M Engineers 1993). Wobble friction arises from unintentional misalignment of tendons and only occurs for internal tendons (Larsa 4D 2019). The wobble friction coefficient was assumed to be 0.0002 for the internal longitudinal tendons in the main span. Seating losses are a result of slippage at the anchorage due to stress transfer from the steel strands to the concrete when they are released after jacking. The anchor set was taken as 3/8 inch for the Varina-Enon Bridge from as-built drawings (F&M Engineers 1993). Both friction losses and seating losses were computed in the finite element model before the staged construction analysis (Larsa 4D 2019).

Elastic shortening losses depend on the total number of tendons in the section as well as the sequence of stressing. These losses arise from the elastic shortening of the concrete as the precompression force from each tendon is applied when released after jacking. Since elastic shortening losses are dependent on the sequence of stressing, they were computed during the staged construction analysis in the model. The long-term prestress losses due to creep and shrinkage were also computed during the staged construction analysis (Larsa 4D 2019). CEB-FIP ’90 code expressions were used to compute creep and shrinkage strains at each time step, and the changes in these strains were used to calculate the prestress losses (Lindley 2019). Long-term losses due to relaxation of the steel strands over time were also computed during the staged construction analysis (Larsa 4D 2019). Figure 3.9 provides an example of a tendon force profile computed by the finite element model during jacking, after seating, and in 2019 after long-term losses.

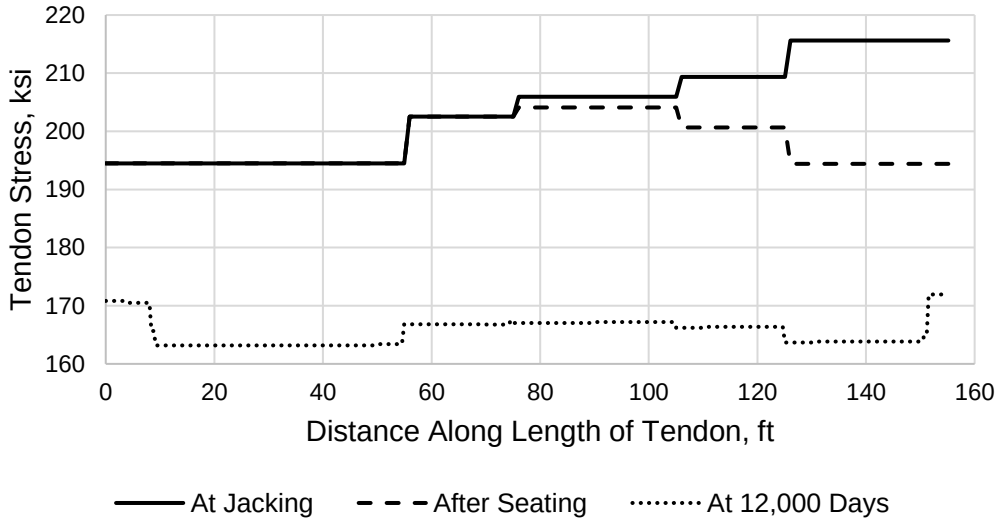

Figure 3.9: Tendon S6-T9L Stress Profile

3.4 Effective Prestress Calculations from Field Data

3.4.1 Overview

The effective prestress forces at the joint openings in Spans 5, 6, and 9 were calculated using data acquired from the instrumentation in those spans. The calculation procedure was based on the assumption that the total stress at the location of a joint when it opens is zero. Equation (3-1) governs the computation of the stress in the cross-section of a prestressed structure.

$$\sigma = -\left(\frac{P_e}{A}\right) - \left(\frac{P_e e y}{I}\right) + \left(\frac{M y}{I}\right) + \sigma_{temp} \qquad (3\text{-}1)$$

Where:

P_e = effective prestress force

A = area of cross-section

e = tendon eccentricity from centroid of section

y = centroid of section

I = moment of inertia of section

M = sum of all moments due to self-weight, live load, secondary prestress, creep, and shrinkage

σ_{temp} = stresses arising from forces due to thermal gradients

Setting the above equation equal to zero, rearranging to solve for effective prestress, and further breaking down the terms gives Equation (3-2), which was directly used to calculate the effective prestress force from field data (Lindley 2019).

$$P_e = \left(-\sigma_{SE} + \sigma_{con} + \frac{\left(M_{sw} + M_{live} + M_{other}\right) y}{I_{cr}} + \frac{P_{sw} + P_{other}}{A_{cr}} \right) \left(A_{cr} + \frac{I_{cr}}{e_{cr} y_{cr}} \right) \qquad (3\text{-}2)$$

Where:

P_e = effective prestress force

σ_{SE} = self-equilibrating stress at the bottom flange due to thermal gradients

σ_{con} = continuity stress associated with thermal moments

M_{sw} = self-weight moment

M_{live} = live-load moment

M_{other} = moment due to secondary effects from prestressing, creep, and shrinkage

I_{cr} = cracked transformed moment of inertia of the box girder

P_{sw} = axial force due to the self-weight of the structure and restraint of movement at bearings

P_{other} = axial force due to secondary effects from prestressing, creep, and shrinkage

A_{cr} = cracked transformed area of the box girder

e_{cr} = tendon eccentricity from the cracked centroid

y_{cr} = distance from the cracked centroid to the top of the bottom flange of the section

y = distance from the uncracked centroid to the top of the bottom flange of the section

All of the terms on the right-hand-side of the equation were obtained from either field data, known section properties, or a staged construction analysis in the finite element model. The processes of computing these values are described in the following sections. See Lindley (2019) for sample calculations following these procedures.

3.4.2 Section Properties

Transformed, cracked section properties were used in the calculation of the effective prestress force since the bottom flange was entirely decompressed when the joint opened and data was collected. The contribution of mild steel to the transformed section was not considered since it does not extend through the joints between segments. The cracked section used in the analysis is shown in Figure 3.10. The cracked, transformed area was taken as 12,267.75 in^2. The cracked, transformed moment of inertia was calculated to be 16,346,893.09 in^4. The centroid of the uncracked section was taken as 98.5 in., while the centroid of the cracked section was taken as 112.67 in. (Lindley 2019). The tendon eccentricities from the centroid of the cracked section were calculated to be 91.06 in. for Section A-A in Span 6, and 109.68 in. for Section C-C in Span 5 and Section D-D in Span 9.

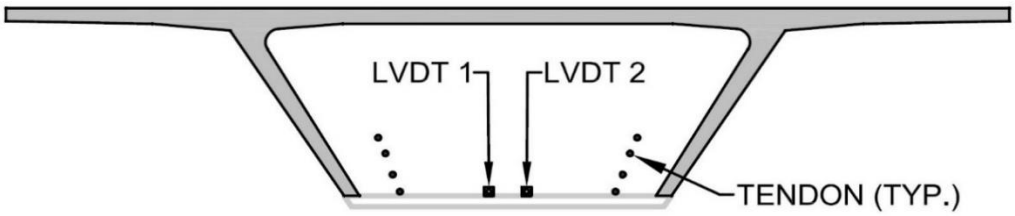

Figure 3.10: Cracked Section Used in the Analysis (Lindley 2019, with permission)

3.4.3 Dead Load Moment

The dead load moment was calculated by running a staged construction analysis in the finite element model. The dead load included the self-weight of the superstructure, deviator blocks, anchor blocks, and barrier rails. The self-weights of the deviator blocks and anchor blocks were calculated from the geometry given in the design drawings. These weights were applied as point loads at their respective

locations in the model. The rest of the self-weight, including the barrier rail, was incorporated as a distributed load equal to 15.86 klf (Lindley 2019). Figure 3.11 and Figure 3.12 show the moments due to dead load in Spans 5, 6, and 9. The values of the dead load moment at Section A-A, Section C-C, and Section D-D are indicated.

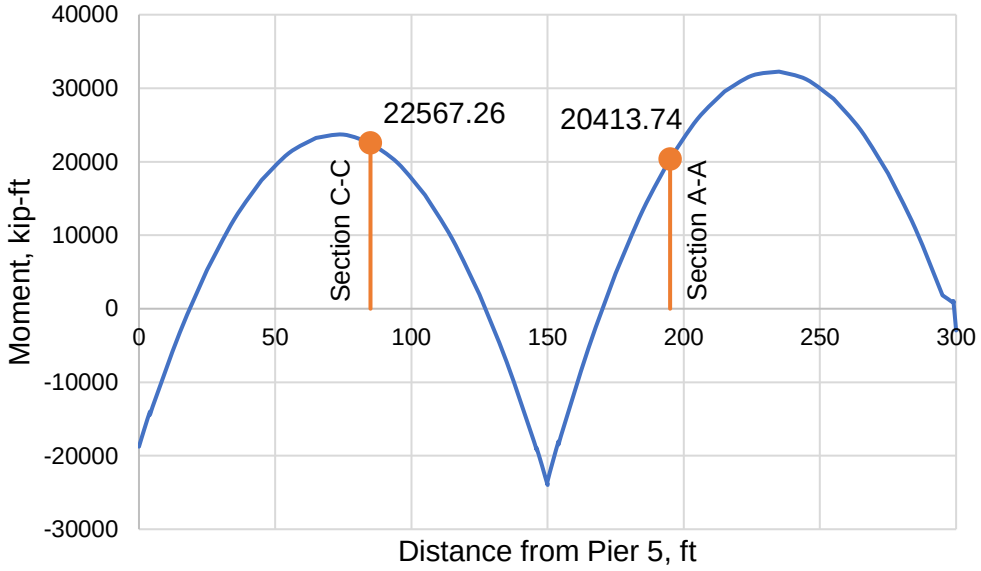

Figure 3.11: Spans 5 and 6 Dead Load Moment

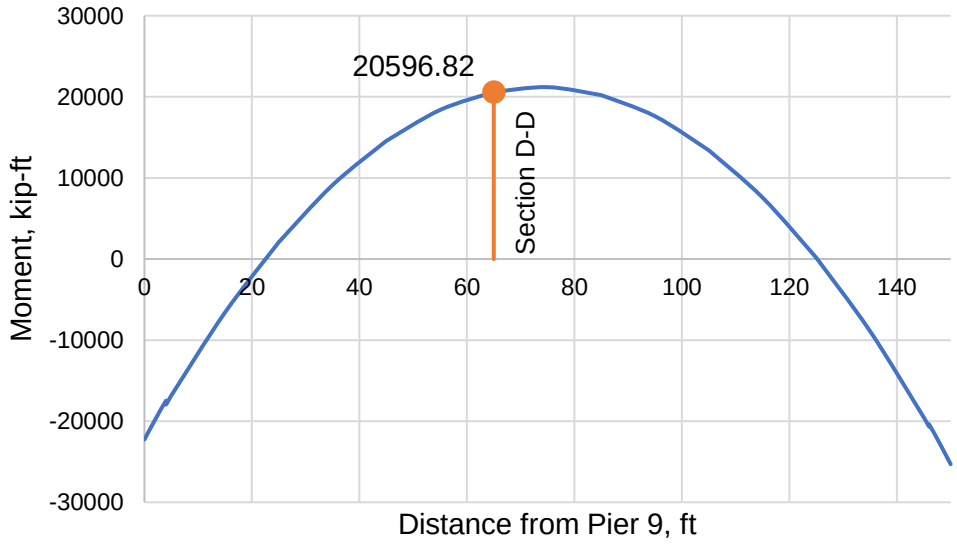

Figure 3.12: Span 9 Dead Load Moment

3.4.4 Live Load Moment

The live load moments at the joint openings were calculated by conducting an influence line analysis in the finite element model to correlate the measured live load strains at the trigger gages to the strains at the locations of interest. This method was used rather than directly calculating the live load strain from the strain measurements adjacent to the opening joints because the bottom flange could resist no more tension force when it decompressed during a crack-opening event. This created a "plateau" effect in the strain measurement, which can be seen in Figure 3.6.

The strain measured by the trigger gage at Section B-B, ST01, was used to determine the live load moments at Sections A-A and C-C. Conducting an influence line analysis in the finite element model resulted in an envelope of maximum moments that could be used to correlate the maximum moment at Section B-B to the maximum moments at Sections A-A and C-C (Lindley 2019). This envelope of maximum moments as a fraction of the moment at Section B-B is shown in Figure 3.13. Similarly, the live load moment at Section D-D in Span 9 was determined from the strain measured by the trigger gage at Section E-E, ST04. The envelope of maximum moments as a fraction of the moment at Section E-E is shown in Figure 3.14. The coefficients indicated in Figure 3.13 and Figure 3.14 were used to scale the live load strains and obtain the live load moments at the sections of interest.

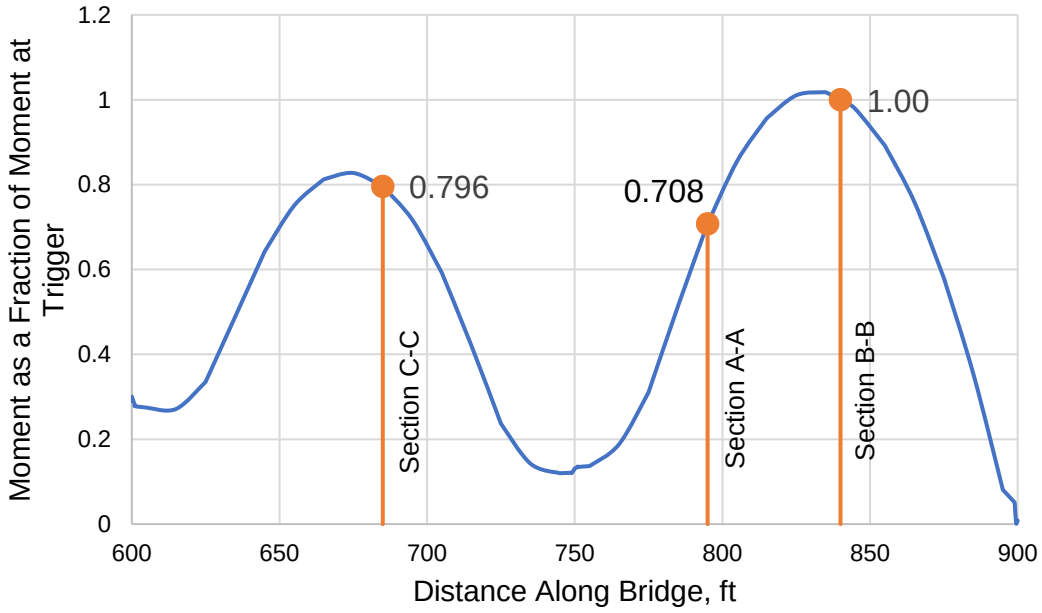

Figure 3.13: Spans 5 and 6 Envelope of Maximum Moments

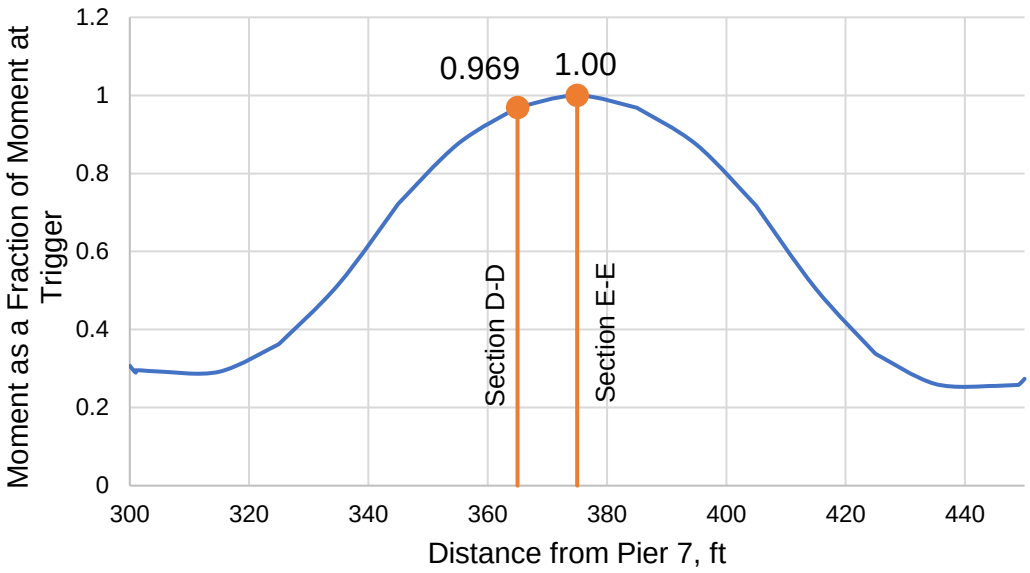

Figure 3.14: Span 9 Envelope of Maximum Moments

3.4.5 Creep, Shrinkage, and Secondary Prestress Axial Forces and Moments

Creep, shrinkage, and secondary prestress effects result in axial forces and moments due to redundancy in a structure. All axial forces and moments at locations of interest due to these effects were determined from a staged construction analysis in the finite element model, and can be seen in Table 3.3. The values of these axial forces and moments were dependent on the creep and shrinkage factors input as parameters in the finite element model, and the primary prestress forces and tendon forces are directly tied to the secondary forces. Therefore, iteration of these factors was required in order to obtain the appropriate values for creep, shrinkage, and secondary prestress axial forces and moments. Various trial creep and shrinkage factors were input as parameters in the finite element model until the effective prestress results obtained from the model and from field data were closely aligned. The appropriate creep and shrinkage factors were determined to each be 1.85.

Creep causes axial shortening and bending in a structure as it deforms under a sustained dead load. The creep axial force tends to be positive (tensile) due to the axial shortening. However, negative (compressive) values of creep axial force can be attributed to the restrained bending of the superstructure. Shrinkage causes axial shortening with no bending, so the shrinkage axial force is always positive. Bending moments due to shrinkage effects result from differential shortening of the superstructure. Secondary prestress effects are caused when a redundant structure is stressed. Prestress forces would cause a simply supported structure to shorten axially and camber upwards. In a redundant structure, these deformations are restrained by the self-weight of the superstructure and the stiffness of the bearing supports (Lindley 2019).

Table 3.3: Creep, Shrinkage, and Secondary Prestress Effects at Instrumented Joint Openings

Force/Moment	Section C-C (Span 5)	Section A-A (Span 6)	Section D-D (Span 9)
M_{cr}	1,623 kip-ft	1,960 kip-ft	749.2 kip-ft
P_{cr}	56.10 kip	172.4 kip	-34.90 kip
M_{sh}	-487.6 kip-ft	310.1 kip-ft	588.9 kip-ft
P_{sh}	842.7 kip	661.2 kip	839.4 kip
M_2	20,150 kip-ft	15,830 kip-ft	23,280 kip-ft
P_2	166.7 kip	163.6 kip	261.2 kip

3.4.6 Self-Equilibrating Stresses

As mentioned in Section 2.4, nonlinear thermal gradients result in both self-equilibrating stresses and thermal continuity stresses. The process of calculating self-equilibrating stresses is described in this section, and the computations for thermal continuity stresses are described in Section 3.4.7. See Lindley (2019) for a more detailed description of the concepts underlying these calculations.

Self-equilibrating stress can be conceptualized as the thermally induced stress due to a non-linear thermal gradient in an artificially restrained structure, added to the stresses resulting from the axial load and moment that would be required to remove the artificial restraints. Therefore, the thermally induced stress in the bottom flange was calculated considering the removal of interior supports and artificially restraining each approach span unit at the locations of expansion joints (Lindley 2019). For calculations in Spans 5 and 6, the interior supports were removed, and the superstructure was restrained only at Piers 1 and 7. For calculations in Span 9, the interior supports were removed, and the superstructure was restrained only at Piers 7 and 13. Equation (3-3) governed the calculation of the thermally induced stress in the bottom flange (Lindley 2019).

$$\sigma_{t1} = -E\alpha\Delta T_1 \qquad (3\text{-}3)$$

Where:

σ_{t1} = thermally induced stress in the bottom flange when fully restrained

E = modulus of elasticity

α = coefficient of thermal expansion

ΔT_1 = difference in temperature between the coolest location, and TC_1

The restraining axial forces and moments were calculated as those required to fully restrain the structure from elongation and bending due to thermally induced stresses. These computations were governed by Equations (3-4) and (3-5) (Lindley 2019).

$$P = \sum_{i=1}^{18} E\alpha\Delta T_i A_i \quad (3\text{-}4)$$

$$M = \sum_{i=1}^{18} E\alpha\Delta T_i A_i Y_i \quad (3\text{-}5)$$

Where:

ΔT_i = difference in temperature between TC_i, and TC_{cool}

A_i = tributary area of thermocouple i, as presented in Table 3.1

Y_i = distance of thermocouple i from the center of gravity of the section

Finally, the total self-equilibrating stresses were calculating by summing the thermally induced stress in the bottom flange, the stress due to the restraining axial force, and the stress due to the restraining axial moment. This computation was governed by Equation (3-6) (Lindley 2019).

$$\sigma_{SE} = \sigma_t + \frac{P}{A} + \frac{My}{I} \quad (3\text{-}6)$$

3.4.7 Thermal Continuity Forces

As described in Section 2.4, thermal continuity forces arise from the application of non-linear thermal gradients on a redundant structure, so these forces were calculated considering the internal supports. Forces arising from thermal gradients can be idealized as a constant moment and axial force applied at the ends of a structure. Therefore, a constant moment and axial force were applied at the ends of Spans 1-6 and Spans 7-12 in the finite element model to obtain normalized bending moment and axial force diagrams. These diagrams were used to obtain coefficients at Sections A-A, C-C, and D-D that could be used to scale Equations (3-4) and (3-5) for any distribution of temperatures. The scaled axial force and moment were the thermal continuity forces (Lindley 2019). The axial force coefficients were taken as -0.0266 for Section C-C in Span 5, -0.02 for Section A-A in Span 6, and -0.0195 for Section D-D in Span 9. The normalized bending moment diagrams with the scaling coefficients indicated can be seen in Figure 3.15 and Figure 3.16.

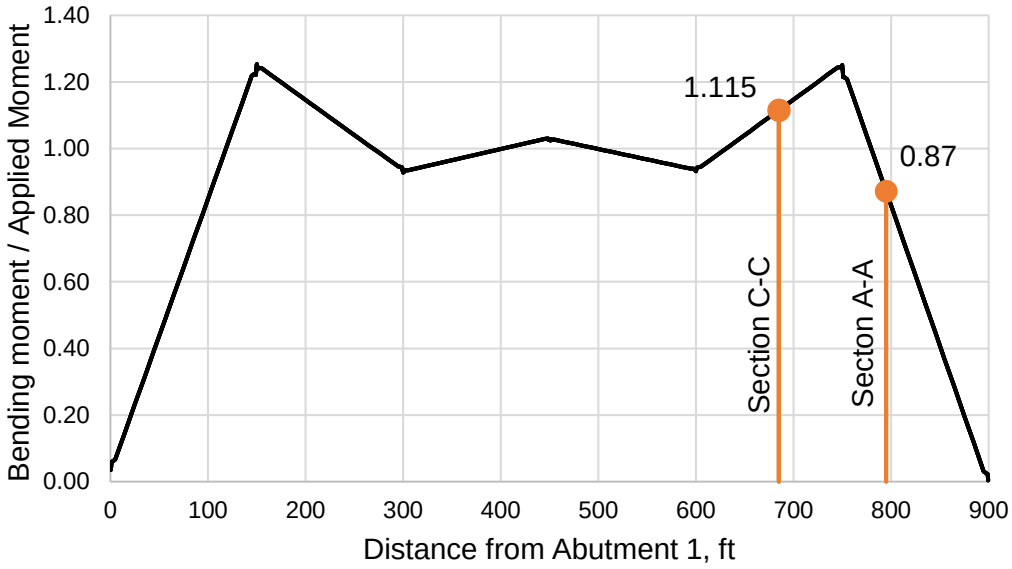

Figure 3.15: Thermal Continuity Moment as a Fraction of Applied Moment, Spans 1-6

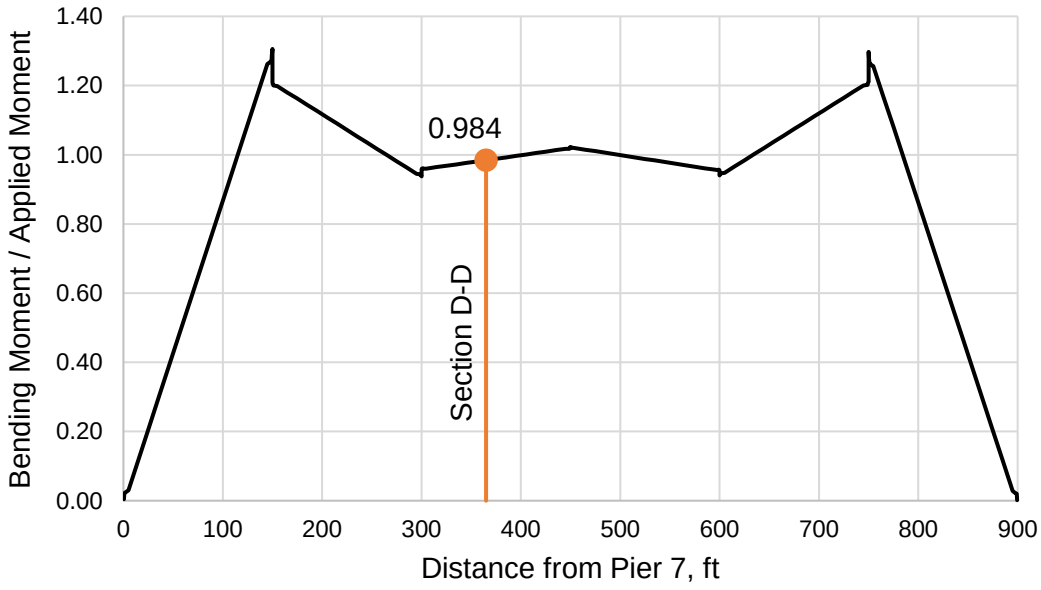

Figure 3.16: Thermal Continuity Moment as a Fraction of Applied Moment, Spans 7-12

Chapter 4. Results and Discussion

This chapter presents analysis results as obtained by the methods described in the previous chapter. In the first section, the finite element model is validated using data from load tests conducted by Duemmel et al. (1992) and Maguire et al. (2014). The second section outlines the results from the model including the prestress losses predicted at the crack-opening locations in Spans 5, 6, and 9. In the third section, the results of the effective prestress calculations from field data are presented. Finally, the fourth section provides a comparison of finite element and field data results.

4.1 Validation of Finite Element Model

4.1.1 Approach Span Validation

The modeling of approach spans was validated by verifying that the predicted behavior was consistent with that measured during live-load tests conducted by Maguire et al. (2014) in August of 2012. Three different *load configurations* were implemented during the live load tests. Load configuration 1 (LC1) consisted of one truck driving in the northbound center lane. Load configuration 2 (LC2) consisted of one truck driving in the northbound left lane. Load configuration 3 (LC3) consisted of two trucks, one driving in the northbound left lane and one driving in the northbound center lane. A deflectometer measured the vertical deflections at the mid-span of Span 5 during the load tests (Maguire et al. 2014).

The axle loads for the three loading configurations were applied to the finite element model as static loads. Table 4.1 provides a comparison between the field-recorded maximum mid-span deflections in Span 5 and those obtained from the model. The percent difference between the analytically obtained and measured deflections ranges from 0.00% to 20.97%, which is considered satisfactory. The results obtained from this validation are almost identical to those obtained by Lindley (2019). This is expected since the approach spans in the full structure model were modeled very similarly to the approach spans in the reduced model.

Table 4.1: Measured and Computed Span 5 Mid-span Deflections

Load Configuration	Span 5, Mid-Span Deflection, in.		Percent Difference
	Live-Load Test Results	FE Model Results	
LC1	-0.03	-0.035	16.67%
LC2	-0.035	-0.035	0.00%
LC3	-0.062	-0.075	20.97%

The strains throughout the depth of the box girder cross-sections at the mid-span of Span 5 and Section A-A in Span 6 were also measured. Figure 4.1 and Figure 4.2 provide comparisons between the field-recorded and analytically obtained strains. By visual observation it can be concluded that the strains throughout the depth of the box girders given by the finite element model align closely with the measured strains. Discrepancies can be attributed to the fact that the model assumes linear elastic behavior, but the structure may undergo nonlinear behavior under heavy loadings. In addition, the opening joints in the bottom flanges of the box girders may have influenced the strain readings at those locations. These strain comparisons, in conjunction with the Span 5 mid-span deflection comparison, confirm that the approach span portions of the finite element model adequately represent the actual structure's behavior.

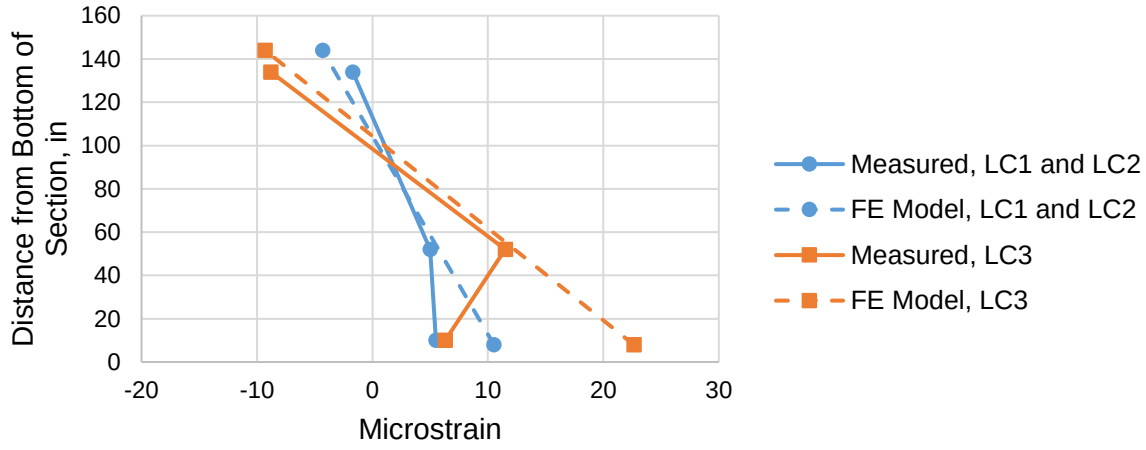

Figure 4.1: Measured and Computed Strains Throughout the Depth of the Box Girder Cross-Section at the Mid-span of Span 5

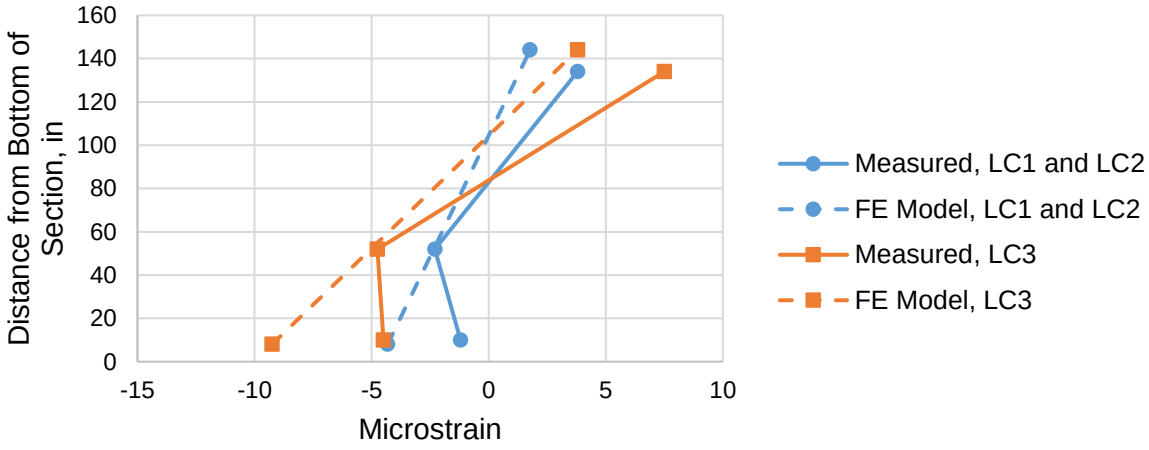

Figure 4.2: Measured and Computed Strains Throughout the Depth of the Box Girder Cross-Section at Section A-A in Span 6

4.1.2 Main Span Validation

The modeling of the main span unit was validated by verifying that the model adequately predicted the bridge response when compared to the measurements obtained during live-load tests conducted by Duemmel et al. (1992). One truck was used for these load tests, and its location varied along the length of the main span unit. Loading configurations were implemented on both the northbound and southbound sides, and in both the exterior and interior lanes. The resulting upper and lower flange strains were measured in two segments, Segment 33 and Segment 62, with strain gages embedded in the cross-sections. Segment 33 is located in Span 16 next to the segment adjacent to Pylon 17. Segment 62 is located at the mid-span of Span 16 (Duemmel et al. 1992).

The axle loads were applied to the finite element model as static loads. Two loading configurations were considered, one with the truck on the northbound side and one with the truck on the southbound side. For each case, the location of the truck was 780 ft from Pier 14. The resulting lower flange strains in northbound Segment 33 and upper flange strains in northbound Segment 62 were analyzed. Table 4.2 and Table 4.3 provide a comparison between the analytically obtained and field-recorded strains in Segment 33 and Segment 62, respectively. The percent difference between the finite element results and field measurements ranges from 7.93% to 20.89%, which is considered satisfactory. Therefore, it can be concluded that the main span model adequately represents the actual structure's behavior.

Table 4.2: Measured and Computed Lower Flange Strains in Segment 33

Load Configuration	Segment 33 Lower Flange Strain (με)		Percent Difference
	Live-Load Test Results	FE Model Results	
NBL	-8	-9.27	15.91
SBL	-3.75	-4.35	15.98

Table 4.3: Measured and Computed Upper Flange Strains in Segment 62

Load Configuration	Segment 62 Upper Flange Strain (με)		Percent Difference
	Live-Load Test Results	FE Model Results	
NBL	-0.25	-0.20	20.89
SBL	-0.45	-0.41	7.93

4.2 Finite Element Results

A time-dependent, staged-construction analysis was conducted in the finite element model using the CEB-FIP ’90 code expressions. The results of the analysis included predicted prestress losses in the year 2019, or at 12,000 days. The average tendon stress profiles obtained from the model for Spans 5, 6, and 9 are shown in Figure 4.3, Figure 4.4, and Figure 4.5, respectively. Table 4.4 presents the jacking stresses, effective prestress values at 12,000 days, and prestress losses obtained from the finite element model for each joint opening location considered. The jacking forces were taken from the original design drawings in Appendix A. The prestress losses were calculated as the difference between the jacking stresses and the prestress forces at 12,000 days.

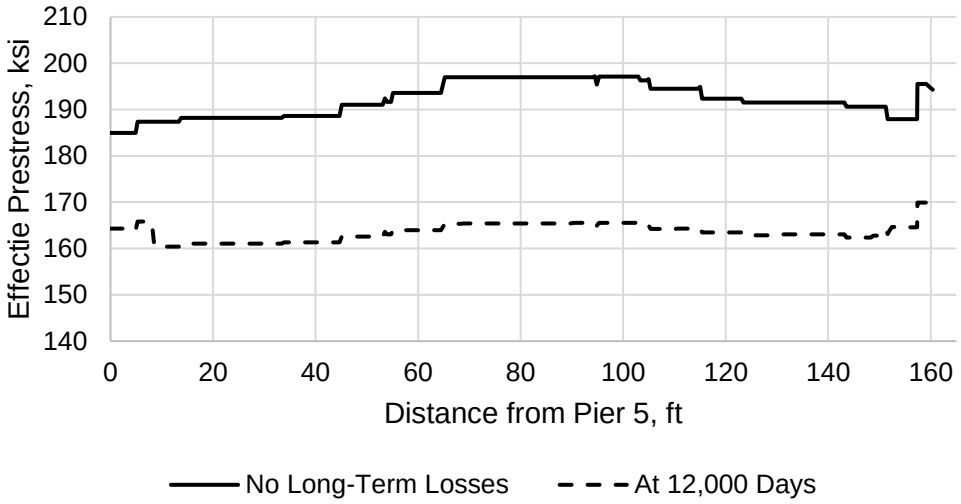

Figure 4.3: Span 5 Average Tendon Profiles

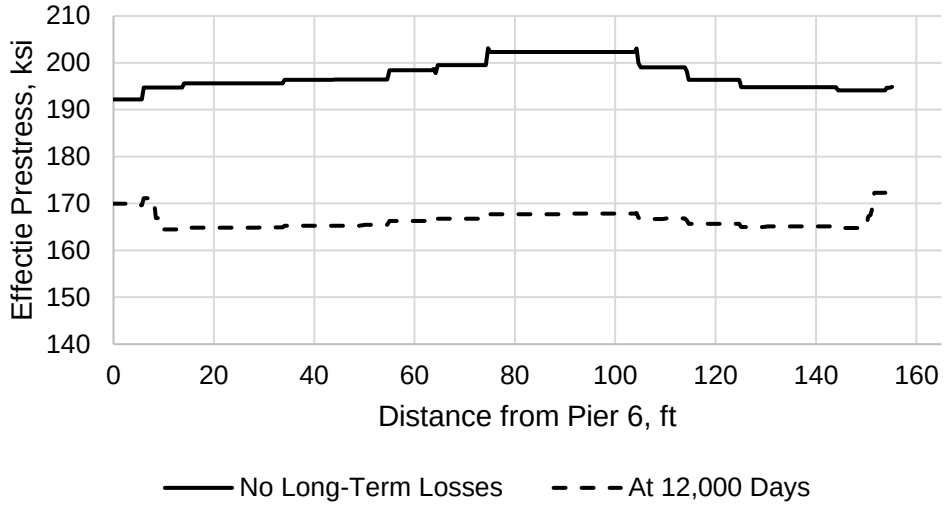

Figure 4.4: Span 6 Average Tendon Profiles

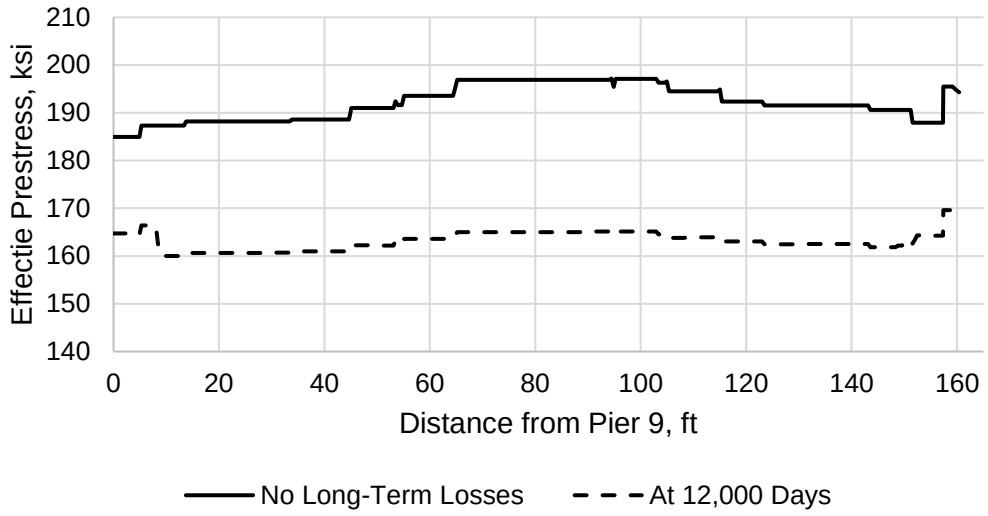

Figure 4.5: Span 9 Average Tendon Profiles

Table 4.4: Prestress Losses per FE Model

Location	Average Jacking Stress (ksi)	Average Prestress at 12,000 Days (ksi)	Average Prestress Loss (ksi)
Section C-C, Span 5	210.3	165.4	44.9
Section A-A, Span 6	213.1	165.3	47.8
Section D-D, Span 9	210.3	165.0	45.3

4.3 Field Data Results

Data collected from the instrumentation at joint openings was used to calculate the effective prestress force for each crack-opening event in accordance with the methods described in Chapter 3. The effective prestress force was estimated at the crack-opening locations in Spans 5, 6, and 9 to compare with the finite element model results.

4.3.1 Span 5 Effective Prestress from Field Data

A total of 10,150 crack-opening events were recorded in Span 5 from May 16, 2019 to June 3, 2020. The average of the effective prestress values calculated at Section C-C for each event was 148.1 ksi with a standard deviation of 6.5 ksi. The maximum crack displacement recorded was 0.0174 in., but the majority of crack openings were significantly smaller than this. A plot of all effective prestress values versus corresponding crack displacements can be seen in Figure 4.6. A histogram showing the distribution of calculated prestress values can be seen in Figure 4.7.

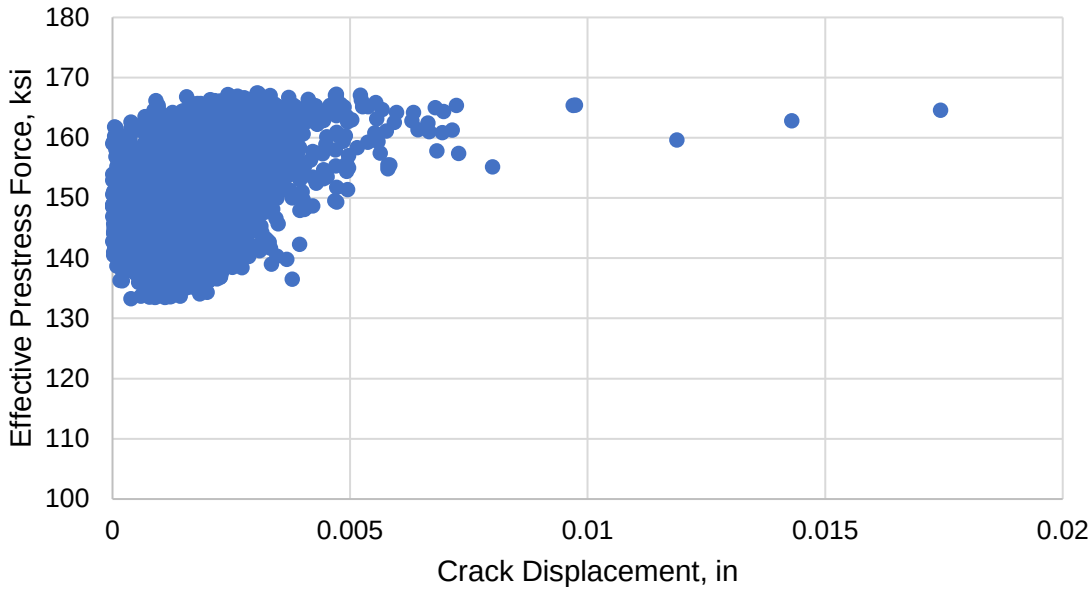

Figure 4.6: Effective Prestress vs. Crack Displacement for all Span 5 Events

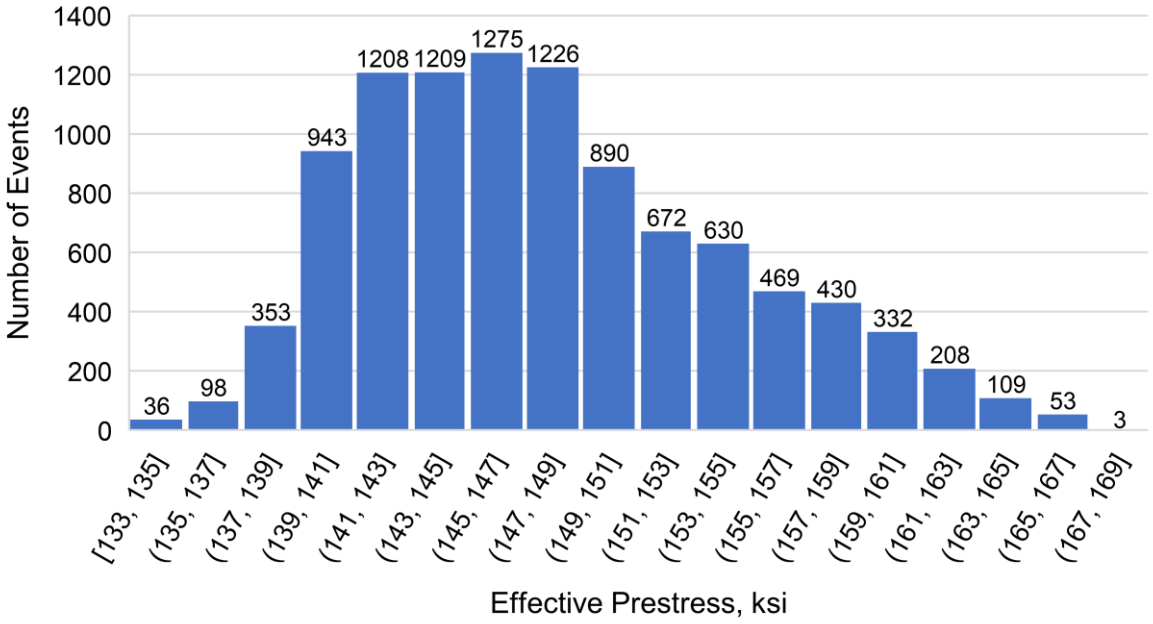

Figure 4.7: Histogram of Prestress Values for all Span 5 Events

It can be seen by the plot in Figure 4.6 that the scatter of prestress values decreases as the crack opening increases. The large variation in prestress estimates at smaller crack displacements is likely due to the fact that the bottom flange may not fully decompress when the crack only opens a small amount. The existence of a compressive stress at the joint opening is inconsistent with the underlying assumption of zero

stress that governs the effective prestress calculations. Therefore, events for which the crack displacements were less than 0.004 in. were discarded. This threshold was chosen since the prestress values in Figure 4.6 begin to converge above this value.

The plot in Figure 4.8 shows the effective prestress values for events with a crack displacement greater than or equal to 0.004 in. This reduced data set consists of 96 events. The mean effective prestress value of these events is 160.3 ksi with a standard deviation of 5.0 ksi.

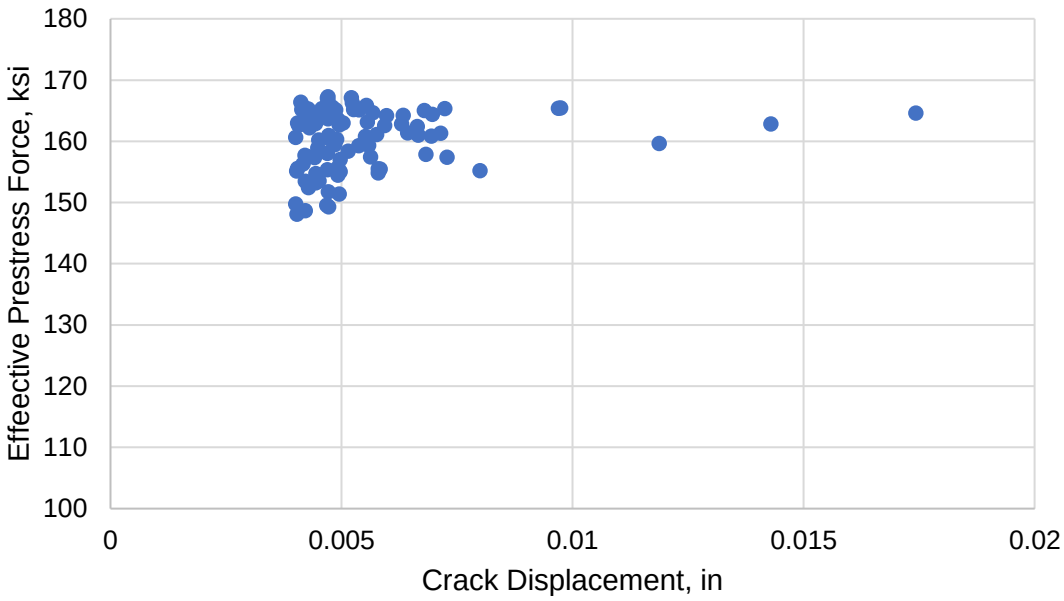

Figure 4.8: Effective Prestress vs. Crack Displacement for Span 5 Events with Corresponding Crack Openings of 0.004 in. or Greater

4.3.2 Span 6 Effective Prestress from Field Data

A total of 10,134 crack-opening events were recorded in Span 6 from May 16, 2019 to June 3, 2020. The mean effective prestress value calculated at Section A-A was 152.6 ksi. The standard deviation of the effective prestress values calculated for all events was 5.8 ksi. The maximum crack displacement recorded was 0.01 in., but the vast majority of crack openings were much smaller. Figure 4.9 presents a plot of effective prestress versus corresponding crack displacements for all Span 6 crack-opening events. Figure 4.10 shows the distribution of the effective prestress values.

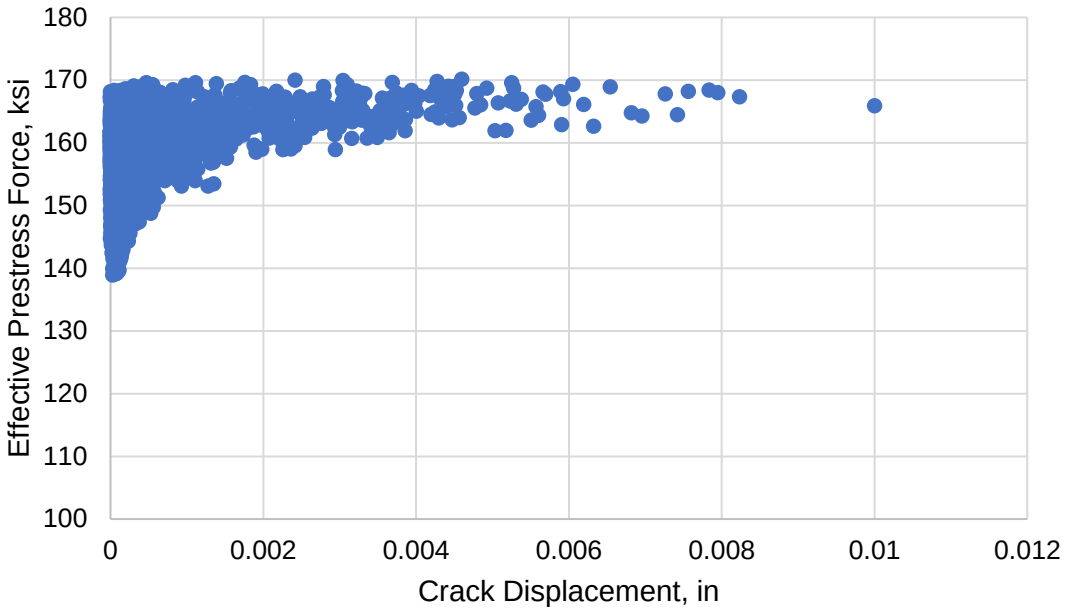

Figure 4.9: Effective Prestress vs. Crack Displacement for all Span 6 Events

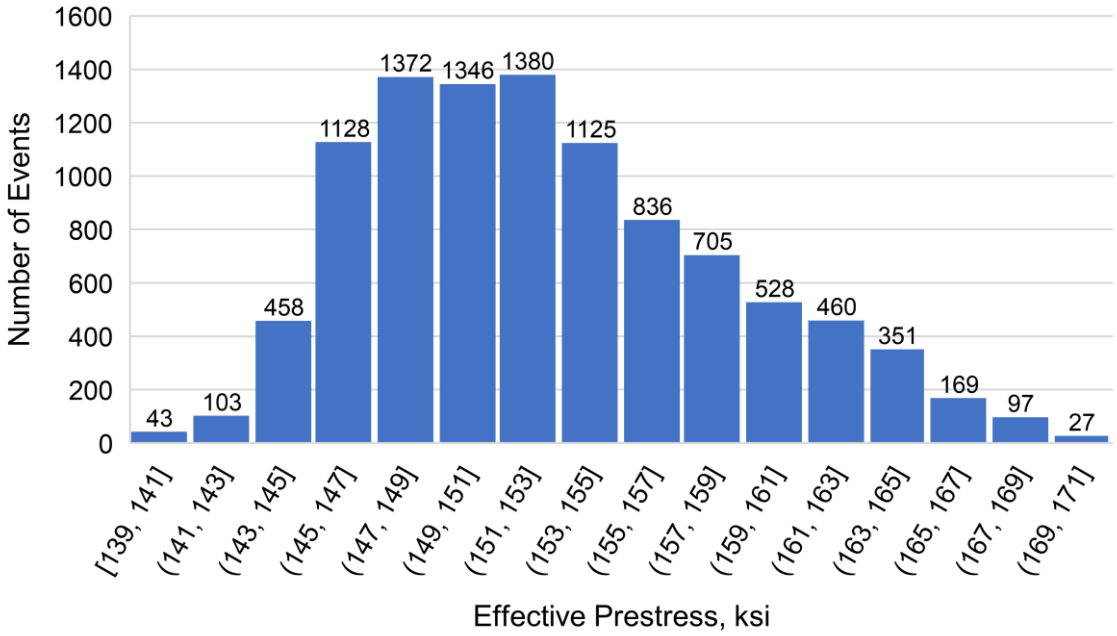

Figure 4.10: Histogram of Prestress Values for all Span 6 Events

Again, it can be seen in Figure 4.9 that there is more scatter in the effective prestress values at lower crack openings since the bottom flange may not fully decompress during these small crack-opening events. In this case, events with corresponding crack displacements less than 0.002 in. were discarded since this

appears to be the value above which the effective prestress calculations begin to converge. A plot of the effective prestress values for events with crack displacements greater than or equal to 0.002 in. can be seen in Figure 4.11. This reduced data set consisting of 212 effective prestress values has a mean of 165.1 ksi and a standard deviation of 2.5 ksi.

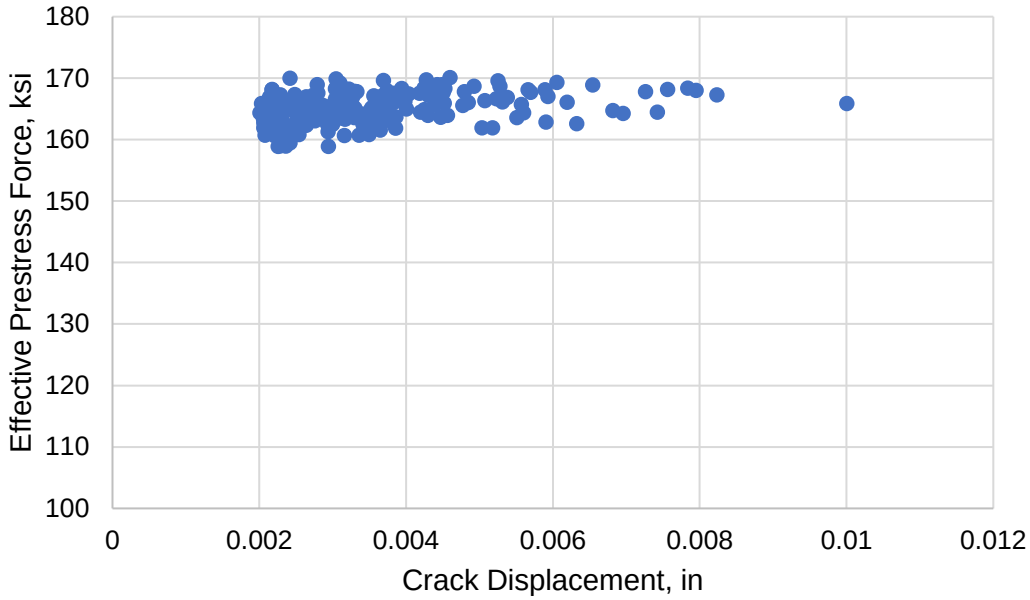

Figure 4.11: Effective Prestress vs. Crack Displacements for Span 6 Events with Corresponding Crack Openings of 0.002 in. or Greater

4.3.3 Span 9 Effective Prestress from Field Data

A total of 1302 crack-opening events were recorded at Section D-D in Span 9 from March 12, 2020 to June 3, 2020. This is a more limited data set than for Spans 5 and 6. The average of the effective prestress values calculated at Section D-D for all events was 155.3 ksi with a standard deviation of 5.7 ksi. The maximum crack opening recorded was 0.00151 in. Again, most crack displacements were significantly smaller than this. A plot of all effective prestress values versus their corresponding crack openings can be seen in Figure 4.12. A histogram showing the distribution of effective prestress values can be seen in Figure 4.13.

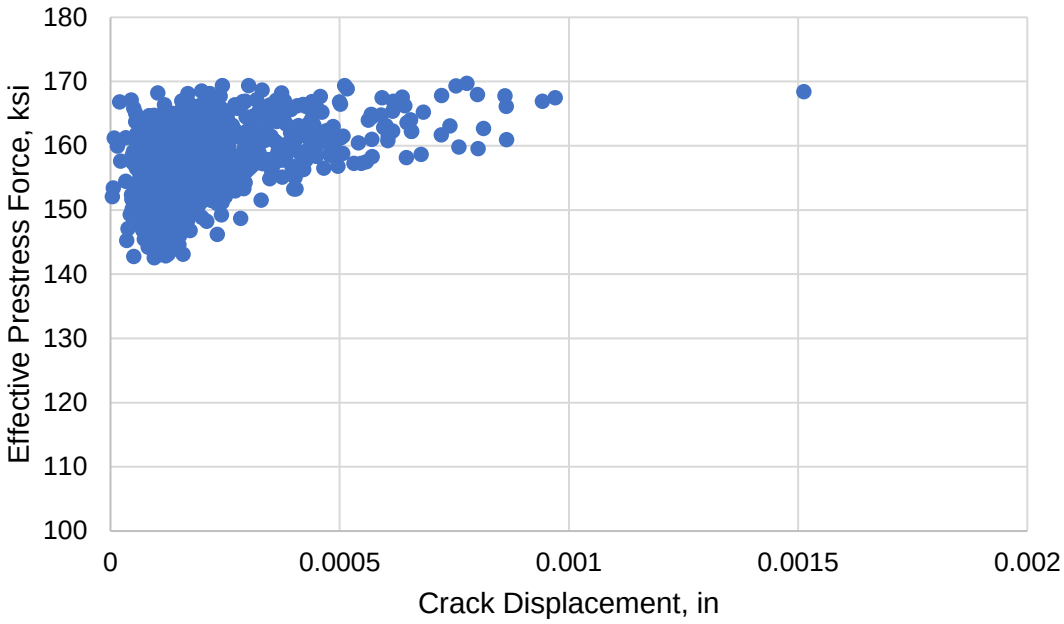

Figure 4.12: Effective Prestress vs. Crack Displacement for all Span 9 Events

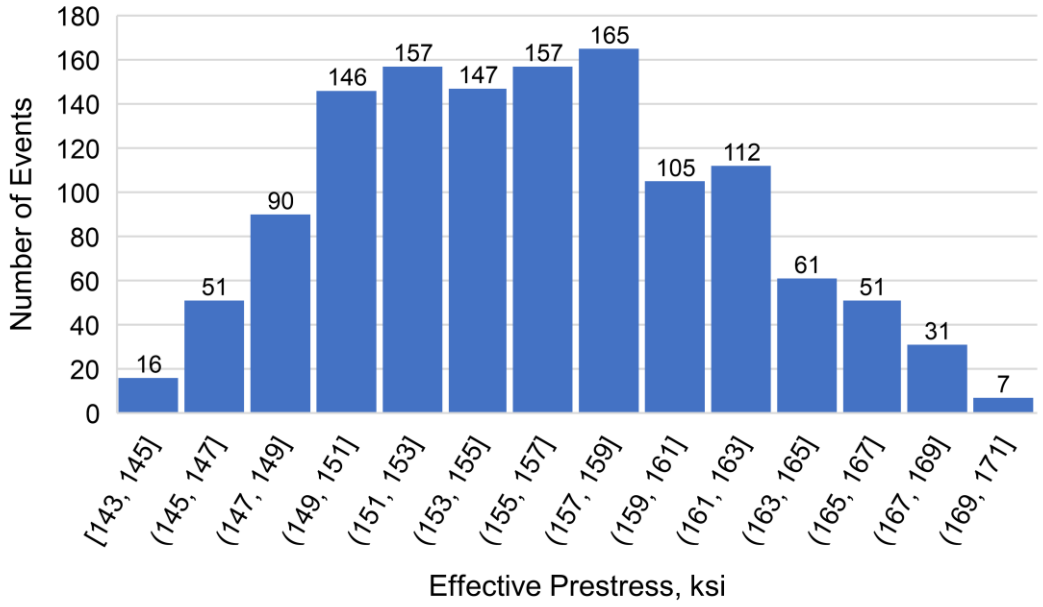

Figure 4.13: Histogram of Prestress Values for all Span 9 Events

Figure 4.12 indicates that, again, there is more scatter in the effective prestress values when the crack displacements are smaller. Events corresponding to crack openings smaller than 0.0005 in. were discarded since the effective prestress calculations begin to converge above this value. Figure 4.14 presents a plot of effective prestress values versus corresponding crack displacements for crack openings greater

than or equal 0.0005 in. This reduced data set consists of 48 events. The average of the effective prestress values for these events is 163.6 ksi with a standard deviation of 3.6 ksi.

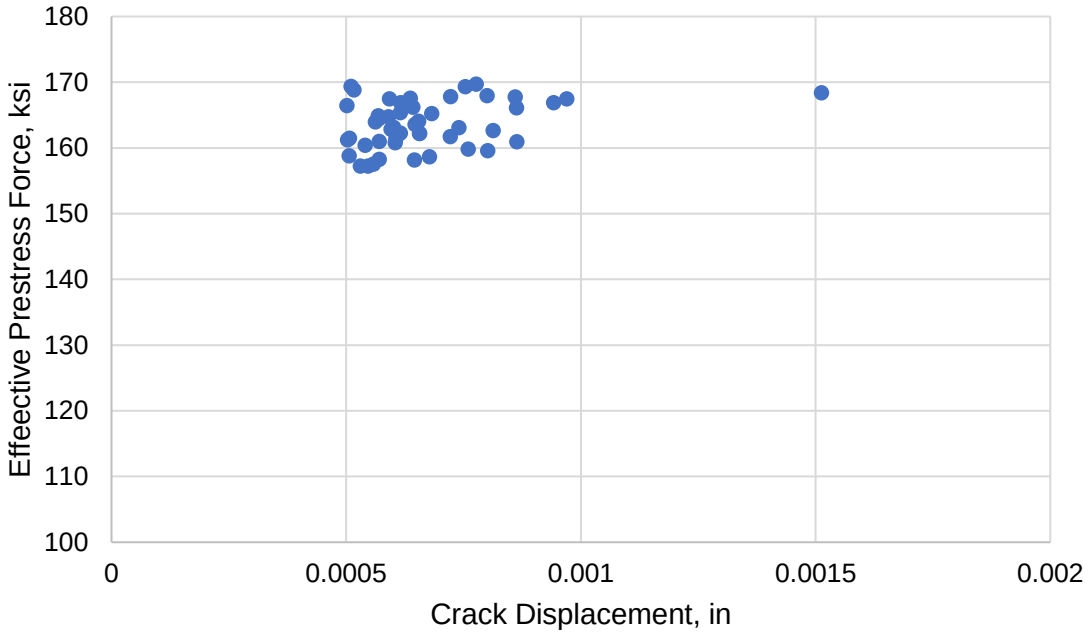

Figure 4.14: Effective Prestress vs. Crack Displacement for Span 9 Events with Corresponding Crack Openings of 0.005 in. or Greater

4.3.4 Field Data Results Summary

A summary of the results obtained from the calculations using field data is provided in Table 4.5. These are the results when considering only crack-opening events with joint displacements greater than the threshold values previously discussed.

Table 4.5: Prestress Losses per Calculations From Field Data

Location	Average Jacking Stress (ksi)	Average Prestress at 12,000 Days (ksi)	Average Prestress Loss (ksi)
Section C-C, Span 5	210.3	160.3	50.0
Section A-A, Span 6	213.1	165.1	48.0
Section D-D, Span 9	210.3	163.6	46.7

4.4 Finite Element and Field Data Comparison

The field data results were compared to the finite element results in order to verify the assumptions made in the effective prestress calculations, and to assess if actual prestress losses are greater than those

predicted by the model. A summary of this comparison is provided in Table 4.6. Again, prestress losses were calculated by subtracting the effective prestress values at 12,000 days from the original jacking stresses. The percent differences between the effective prestress values estimated from field data and those predicted by the model with CEB-FIP '90 code expressions were calculated for each location analyzed.

Table 4.6: Finite Element and Field Data Comparison

		Prestress at 12,000 Days (ksi)	% Difference
Section C-C, Span 5	FE Model	165.4	3.08
	Field Data	160.3	
Section A-A, Span 6	FE Model	165.3	0.12
	Field Data	165.1	
Section D-D, Span 9	FE Model	165.0	0.85
	Field Data	163.6	

Chapter 5. Summary, Conclusions, and Recommendations for Future Work

5.1 Summary

In July of 2012, a flexural crack on the bottom flange of a segment in the Varina-Enon Bridge was observed to open under heavy traffic loads. This indicated unanticipated high levels of tension, which could be attributed to several factors including larger than expected prestress losses. The purpose of this thesis was to estimate the effective prestress forces at the original observed joint-opening location in Span 6 as well as at two other joint-opening locations in Spans 5 and 9. Field data from instrumentation in Spans 5, 6, and 9 was used to calculate the effective prestress forces based on the assumption that the total stress when the cracks opened was equal to zero. A finite element model of the full bridge structure was created in order to conduct a time-dependent staged construction analysis using CEB-FIP '90 code expressions and obtain predicted values of effective prestress to compare with those obtained from field data. This enabled verification of the methods used to calculate effective prestress from field data and provided a means to evaluate if prestress losses were greater than expected.

The results indicated a lot of scatter in calculated effective prestress values for crack-opening events with small joint displacements. Therefore, the results were refined to only include events for which the crack-opening was greater than or equal to a chosen threshold value. These threshold joint displacements were 0.004 in. for Span 5, 0.002 in. for Span 6, and 0.0005 in. for Span 9. The average effective prestress values calculated from these reduced data sets were 160.3 ksi at the crack in Span 5, 165.1 ksi at the crack in Span 6, and 163.6 ksi at the crack in Span 9. The corresponding effective prestress values predicted by the finite element model were 165.4 ksi, 165.3 ksi, and 165.0 ksi.

5.2 Conclusions

Effective prestress estimates from the raw field data including events for all joint displacements indicate significantly larger prestress losses than predicted by the finite element model. However, excluding crack-opening events with very small joint displacements results in improved agreement. The prestress losses calculated from field data are still greater than those predicted by the model, but the discrepancies are not as significant. The model overestimates the effective prestress in 2019 by 3.08% at the crack in Span 5, 0.12% at the crack in Span 6, and 0.85% at the crack in Span 9. These differences are considered to be within a reasonable margin of error, indicating good agreement between the finite element model and field data results. Therefore, it can be concluded that the finite element model verifies the assumptions and methods used to calculate the effective prestress from field data. In addition, the Varina-Enon Bridge does

not seem to be experiencing significantly greater prestress losses than expected when considering CEB-FIP ’90 code expressions.

Prestress losses could greatly influence the future performance and serviceability of the Varina-Enon Bridge. One serviceability concern could be excessive cracking which could lead to ingress of moisture and deterioration of steel tendons. However, considering the opening joints are located on the bottom flanges of the segments and the tendons are encased in grouted PVC ducts, this is not of great concern.

Other future performance concerns related to prestress losses are excessive deflections and reductions in flexural strength. Since prestress losses calculated from field data are not significantly greater than those predicted by the finite element model, these issues are not of great concern either. However, it is important to note that the analyses were run in the model using the CEB-FIP ’90 code expressions, while the Varina-Enon Bridge was designed under the CEB-FIP ’78 code. Previous research concluded that greater prestress losses were predicted using the CEB-FIP ’90 code expressions than the CEB-FIP ’78 code expressions. Therefore, the effective prestress values calculated from field data more closely aligned with the finite element results using CEB-FIP ’90 (Lindley 2019). This leads to the conclusion that although prestress losses are not much greater than those obtained from more recent code expressions, there are greater discrepancies when considering the code that was used for design.

The progression of prestress losses can be evaluated by comparing the results calculated from 2019 and 2020 data to those obtained from 2013 and 2014 data by Lindley (2019). Lindley calculated the effective prestress at just the crack location in Span 6 and obtained a value of 166 ksi. The effective prestress of 165.1 ksi calculated from 2019 and 2020 data represents a 0.54% decrease. In general, it is expected that the effective prestress force decreases rapidly initially after construction and approaches a nearly asymptotic value over time. Using the CEB-FIP ’90 code expressions, the losses in 2013 represent 93.7% of the total 100-year losses (Lindley 2019). Given these two considerations, the effective prestress would be expected to decrease only slightly from 2013 to 2019. The 0.54% decrease obtained aligns with this expectation. Therefore, it can be concluded that the progression of prestress losses in the Varina-Enon Bridge follows what is anticipated.

5.3 Recommendations for Future Work

This research has investigated the prestress losses in Spans 5, 6, and 9 of the Varina-Enon Bridge. In order to further assess the condition of the structure, the following recommendations for future work are made:

1. The prestress losses in Spans 5 and 6 should continue to be monitored in order to evaluate the rate of prestress losses at these locations. This progression should be compared to that obtained from finite element analyses using model codes such as CEB-FIP ’90.
2. Similar cracking to that observed in Spans 5, 6, and 9 has been observed at other locations throughout the bridge. The “mobile” instrumentation setup at Span 9 should be periodically moved to other joints of interest in order to monitor those crack locations and evaluate prestress losses in a similar manner to Spans 5, 6, and 9.
3. For this thesis, LVDTs were installed on the top of the bottom flange at crack locations in Spans 5, 6, and 9. However, the crack openings are likely greater on the bottom of the bottom flange. LVDTs should be installed at the bottom of the bottom flange in order to compare the joint displacements at the top and bottom of the bottom flange.
4. A more detailed analysis should be conducted to determine how the progression of prestress losses affects the future load rating of the Varina-Enon Bridge.
5. The finite element model of the full structure should be used to investigate other aspects of the behavior of the Varina-Enon Bridge, such as response to superloads.

BIBLIOGRAPHY

ACI 209. (2008). *Guide for Modeling and Calculating Shrinkage and Creep in Hardened Concrete*. American Concrete Institute, Farmington Hills, MI.

ACI 423. (2016). *Guide to Estimating Prestress Loss*. American Concrete Institute.

Bažant, Z. P., and Jirásek, M. (2018). *Creep and Hygrothermal Effects in Concrete Structures*. *Solid Mechanics and its Applications*, Springer Science+Business Media B.V., Dordrecht, The Netherlands.

Duemmel, P. S., Baber, T. T., Barton, F. W., and McKeel, Wallace T., J. (1992). *Field Instrumentation and Measured Response ofthe 1-295 Cable-Stayed Bridge: Part I - Field Study of Live Load Responses*. Richmond, VA.

F&M Engineers, I. (1993). *Owner's Manual for Inspection and Maintenance of Segmental Concrete Approaches and Main Span*.

Helmicki, A. J., Hunt, V. J., and Nims, D. K. (2012). *Instrumentation of the Maumee River Crossing*. Cincinnati, OH.

Larsa 4D. (2019). "Larsa 4D Reference Manual."

Lindley, S. M. (2019). "Investigation of the Time-Dependent Longitudinal Flexural Behavior of the Varina-Enon Bridge." Virginia Tech.

Lissenden, C. J. I. (1988). "Dynamic Modeling of a Cable-Stayed Bridge During Construction." University of Virginia.

Maguire, M., Moen, C. D., Roberts-Wollmann, C., and Cousins, T. (2015). "Field verification of simplified analysis procedures for segmental concrete bridges." *Journal of Structural Engineering (United States)*, 141(1), 1–11.

Maguire, M., Roberts-Wollmann, C. L., and Cousins, T. (2014). *Live Load Test and Long Term Monitoring of the Varina-Enon Bridge*. Blacksburg, VA.

Nimse, P. S., Nims, D. K., Hunt, V. J., and Helmicki, A. J. (2015). "Use of Construction Stages to Review a Bridge Finite-Element Model." *Journal of Bridge Engineering*, 20(8), 1–14.

Shahawy, M. A., and Arockiasamy, M. (1996a). "Field instrumentation to study the time-dependent behavior in sunshine skyway bridge. I." *Journal of Bridge Engineering*, 1(2), 76–86.

Shahawy, M. A., and Arockiasamy, M. (1996b). "Analytical and measured strains in sunshine skyway bridge. II." *Journal of Bridge Engineering*, 1(2), 87–97.

Xu, X., Huang, Q., Ren, Y., Zhao, D. Y., Yang, J., and Zhang, D. Y. (2019). "Modeling and Separation of Thermal Effects from Cable-Stayed Bridge Response." *Journal of Bridge Engineering*, 24(5), 1–16.

Appendix A. Original Drawings of Tendon Profiles

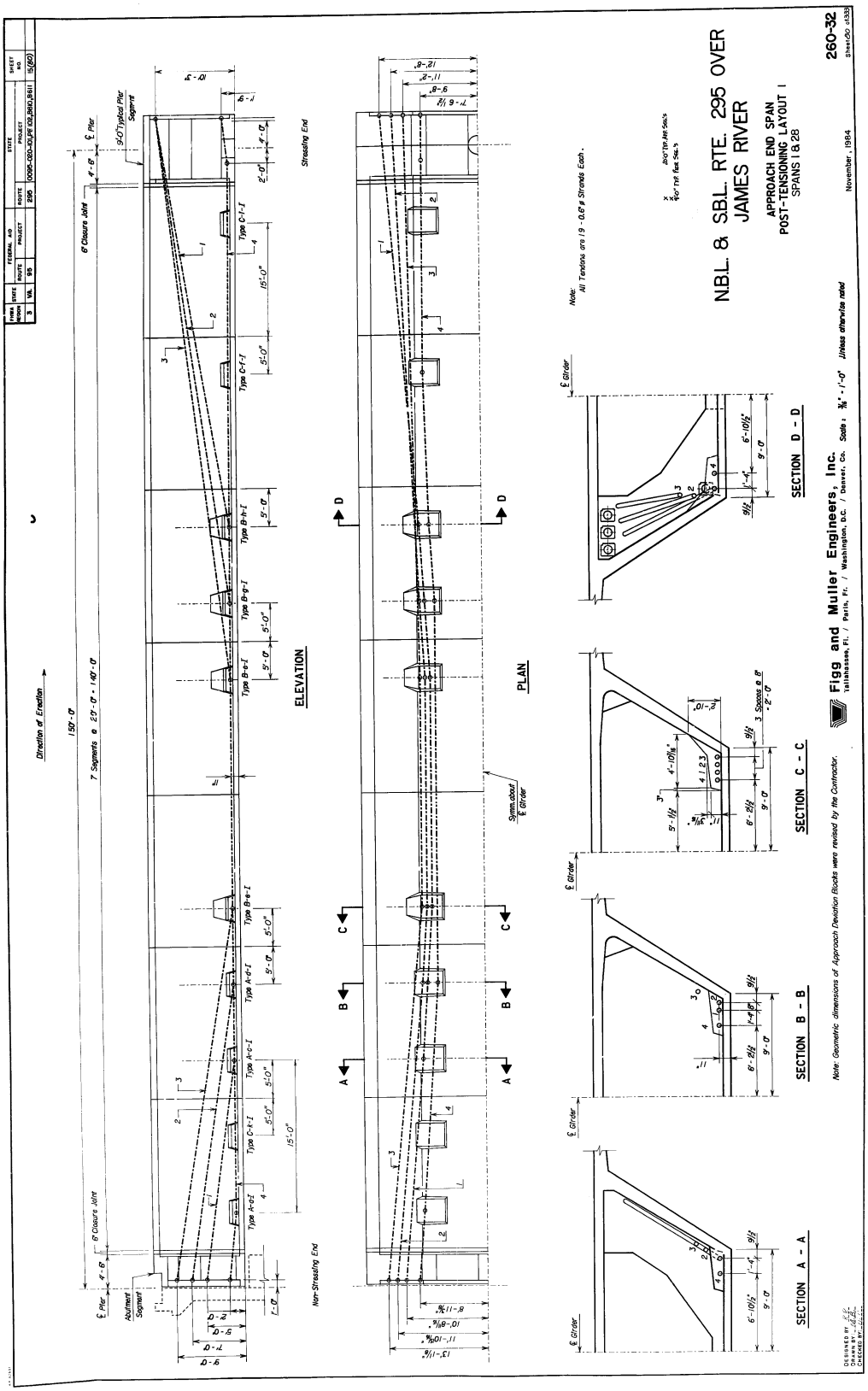

FHWA REGION	STATE	FEDERAL AID ROUTE	FEDERAL AID PROJECT	STATE ROUTE	STATE PROJECT	SHEET NO.
3	VA.	95		295	0095-020-101,PE 102,B610,B611	15(81)

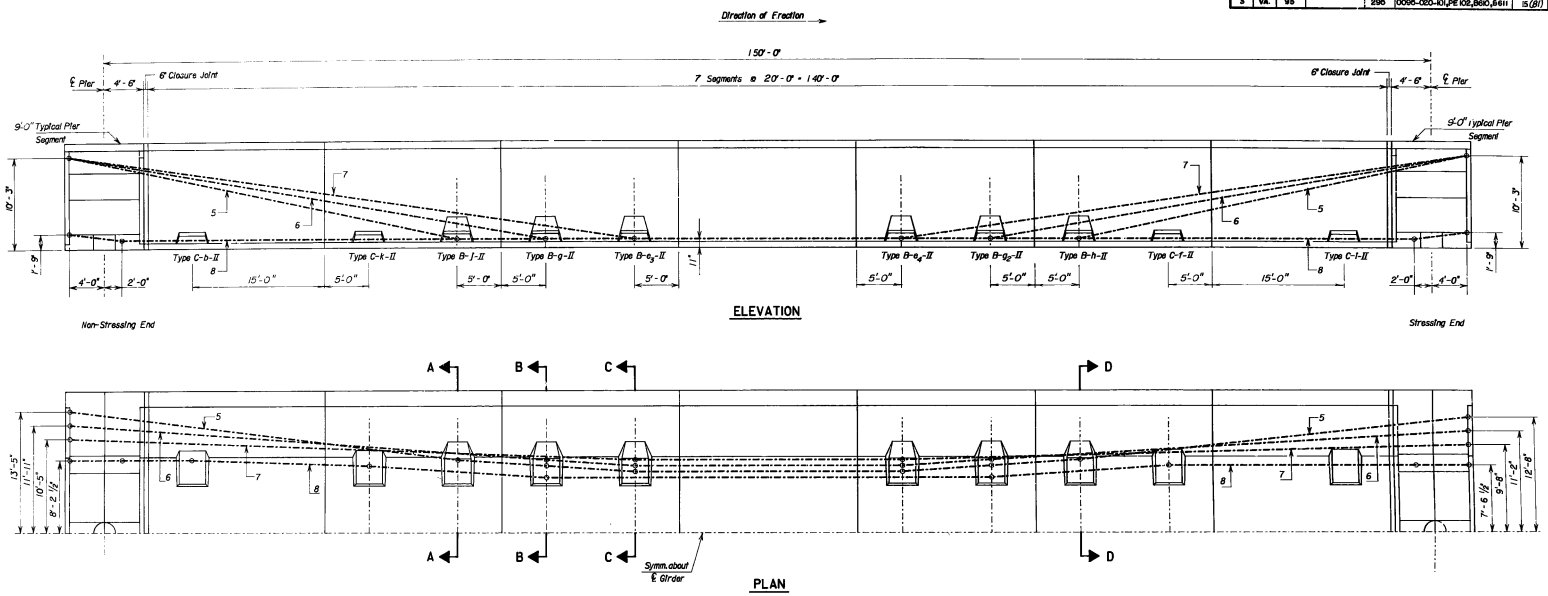

ELEVATION

PLAN

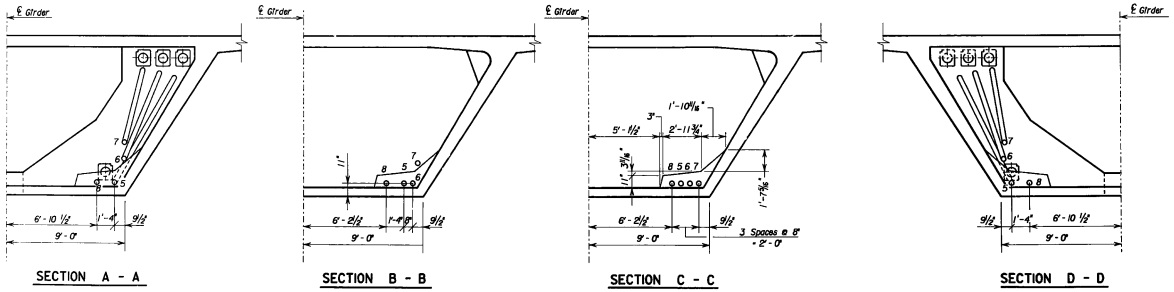

SECTION A - A

SECTION B - B

SECTION C - C

SECTION D - D

Note:
All Tendons are 13 - 0.6" ϕ Strands Each.

20'-0" Typ. Appr. Segs.
9'-0" Typ. Pivot Segs.

N.B.L. & S.B.L. RTE. 295 OVER JAMES RIVER

APPROACH TYPICAL SPAN POST-TENSIONING LAYOUT II SPANS 2-5, 8-11, 21-23, 26 AND 27

DESIGNED BY
DRAWN BY
CHECKED BY

Note: Geometric dimensions of Approach Deviation Blocks were revised by the Contractor.

Figg and Muller Engineers, Inc.
Tallahassee, Fl. / Paris, Fr. / Washington, D.C. / Denver, Co. Scale: 3/16" = 1'-0" Unless otherwise noted

November, 1984

260-32
Sheet 61 of 333

FHWA REGION	STATE	FEDERAL AID ROUTE	FEDERAL AID PROJECT	STATE ROUTE	STATE PROJECT	SHEET NO.
3	VA.	95		295	0096-020-101,PE 102,B610,B611	15(82)

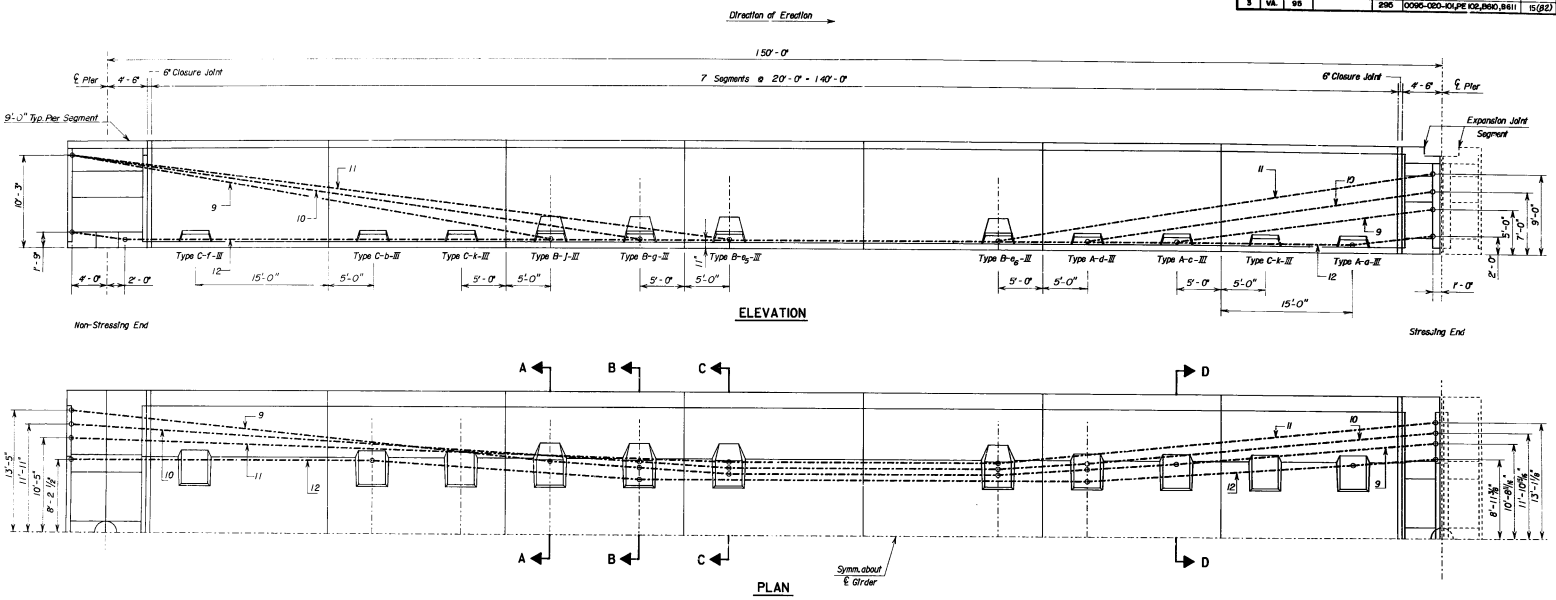

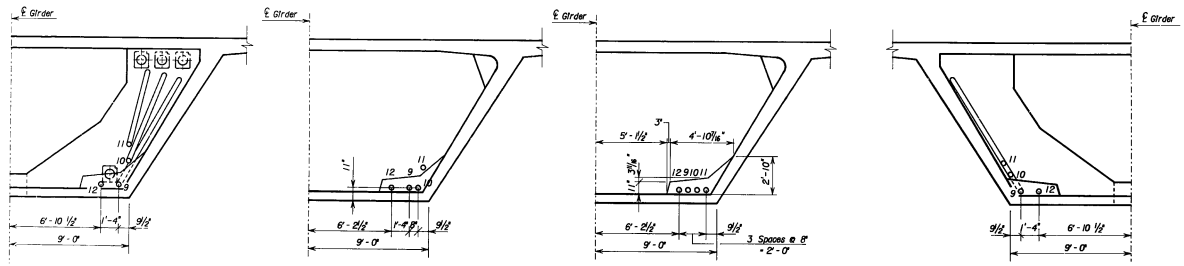

SECTION A - A

SECTION B - B

SECTION C - C

SECTION D - D

Note:
All Tendons are 19 - 0.6" ϕ Strands Each.

10'-0" TYP. APP. SPANS
9'-0" TYP. PIER SPANS

N.B.L. & S.B.L. RTE. 295 OVER JAMES RIVER

APPROACH EXPANSION JOINT SPAN POST-TENSIONING LAYOUT III SPANS 6, 12, 20 & 25

Note: Geometric dimensions of Approach Deviation Blocks were revised by the Contractor.

DESIGNED BY
DRAWN BY
CHECKED BY

Figg and Muller Engineers, Inc.
Tallahassee, Fl. / Paris, Fr. / Washington, D.C. / Denver, Co.

Scale: 3/16" = 1'-0" Unless otherwise noted

November, 1984

260-32

Sheet 92 of 339

FHWA REGION	STATE	FEDERAL AID ROUTE	FEDERAL AID PROJECT	STATE ROUTE	STATE PROJECT	SHEET NO.
3	VA.	95		295	0096-020-101,PE 102,B610,B611	15 (97)

LONGITUDINAL POST TENSIONING QUANTITIES APPROACH SUPERSTRUCTURE

Span No.	Tendon No.	Tendon Type	Tendon Length (ft)	Tendon Weight (lbs)	Number of Tendons / Girder	Total Weight (lbs)	Stressing Force (kips)
1,28	1	19-0.6" ϕ	153.99	2165	4	8,660	861
	2	19-0.6" ϕ	153.96	2164	4	8,658	865
	3	19-0.6" ϕ	154.03	2165	4	8,662	871
	4	19-0.6" ϕ	152.78	2148	4	8,592	861
2,3,4,5, 8,9,10,11, 21,22,23, 26,27,	5	19-0.6" ϕ	159.74	2245	26	58,370	879
	6	19-0.6" ϕ	159.03	2236	26	58,136	871
	7	19-0.6" ϕ	158.58	2229	26	57,954	865
	8	19-0.6" ϕ	157.30	2211	26	57,486	854
6,12 20,25,	9	19-0.6" ϕ	153.99	2165	8	17,320	889
	10	19-0.6" ϕ	153.96	2164	8	17,317	883
	11	19-0.6" ϕ	154.03	2165	8	17,325	874
	12	19-0.6" ϕ	152.78	2148	8	17,184	868
7,24	13	19-0.6" ϕ	153.99	2165	4	8,660	861
	14	19-0.6" ϕ	153.96	2164	4	8,656	865
	15	19-0.6" ϕ	154.03	2165	4	8,660	871
	16	19-0.6" ϕ	152.78	2148	4	8,592	861

TOTAL WEIGHT BOTH GIRDERS = 740,464 Lbs.

POST TENSIONING QUANTITIES APPROACH SUPERSTRUCTURE

Pier	Bar Size	Length	Weight (Lbs.)	Number of Anchorages	Number of Bars	Total Weight (Lbs.)	Stressing Force (kips)
8	1 3/8" ϕ	11.90	66	32	16	1058	166k
9	↑	↑	↑	↑	↑	↑	↑
10	↓	↓	↓	↓	↓	↓	↓
11	↓	↓	↓	↓	↓	↓	↓
12	1 3/8" ϕ	11.90	66	32	16	1058	166k
Totals	——	——	——	160	80	5291	——

Note: Totals shown are for One Girder only.

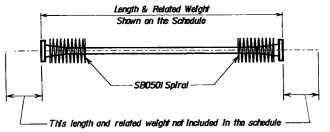

Note : All mild steel reinforcement for Post-tensioning shall be incidental to the system.

VERTICAL POST TENSIONING QUANTITIES APPROACH SUPERSTRUCTURE

Segment	Tendon No.	Number of Segs./ Girder	Tendon Type	Tendon Length (ft)	Tendon Weight (lbs)	Total Weight (lbs)	Stressing Force (kips)
Typical * Pier	A	34	4 x 0.6" ϕ	28.05	83	2823	185k
	B	34	4 x 0.6" ϕ	26.79	79	2696	↑
	C	34	4 x 0.6" ϕ	26.14	77	2630	
	D	34	4 x 0.6" ϕ	25.50	75	2566	
	A'	34	4 x 0.6" ϕ	28.07	83	2824	
	B'	34	4 x 0.6" ϕ	26.80	79	2696	
	C'	34	4 x 0.6" ϕ	26.14	77	2630	
	D'	34	4 x 0.6" ϕ	25.49	75	2565	
Exp.Jt. Pier	A	6	4 x 0.6" ϕ	28.47	84	505	
	B	6	4 x 0.6" ϕ	26.13	77	464	
	C	6	4 x 0.6" ϕ	26.55	79	474	
	D	6	4 x 0.6" ϕ	26.54	79	474	
	A'	6	4 x 0.6" ϕ	28.46	84	505	
	B'	6	4 x 0.6" ϕ	26.12	77	463	
	C'	6	4 x 0.6" ϕ	26.56	79	474	
	D'	6	4 x 0.6" ϕ	26.53	79	474	
Abut.	A	2	4 x 0.6" ϕ	28.47	84	168	
	B	2	4 x 0.6" ϕ	26.13	77	154	
	C	2	4 x 0.6" ϕ	26.55	79	158	
	D	2	4 x 0.6" ϕ	26.54	79	158	
	A'	2	4 x 0.6" ϕ	28.46	84	168	
	B'	2	4 x 0.6" ϕ	26.12	77	154	
	C'	2	4 x 0.6" ϕ	26.56	79	158	
	D'	2	4 x 0.6" ϕ	26.53	79	158	185k

TOTAL WEIGHT BOTH GIRDERS = 53,078 Lbs.

* 9'0" Segments
See ✱

N.B.L. & S.B.L. RTE. 295 OVER JAMES RIVER

SUPERSTRUCTURE POST-TENSIONING QUANTITIES AND STRESSING SCHEDULE

DESIGNED BY KE
DRAWN BY KE
CHECKED BY

Figg and Muller Engineers, Inc.
Tallahassee, Fl. / Paris, Fr. / Washington, D.C. / Denver, Co.

Scale : N / A Unless otherwise noted

November, 1984

260-32
Sheet 97 of 333

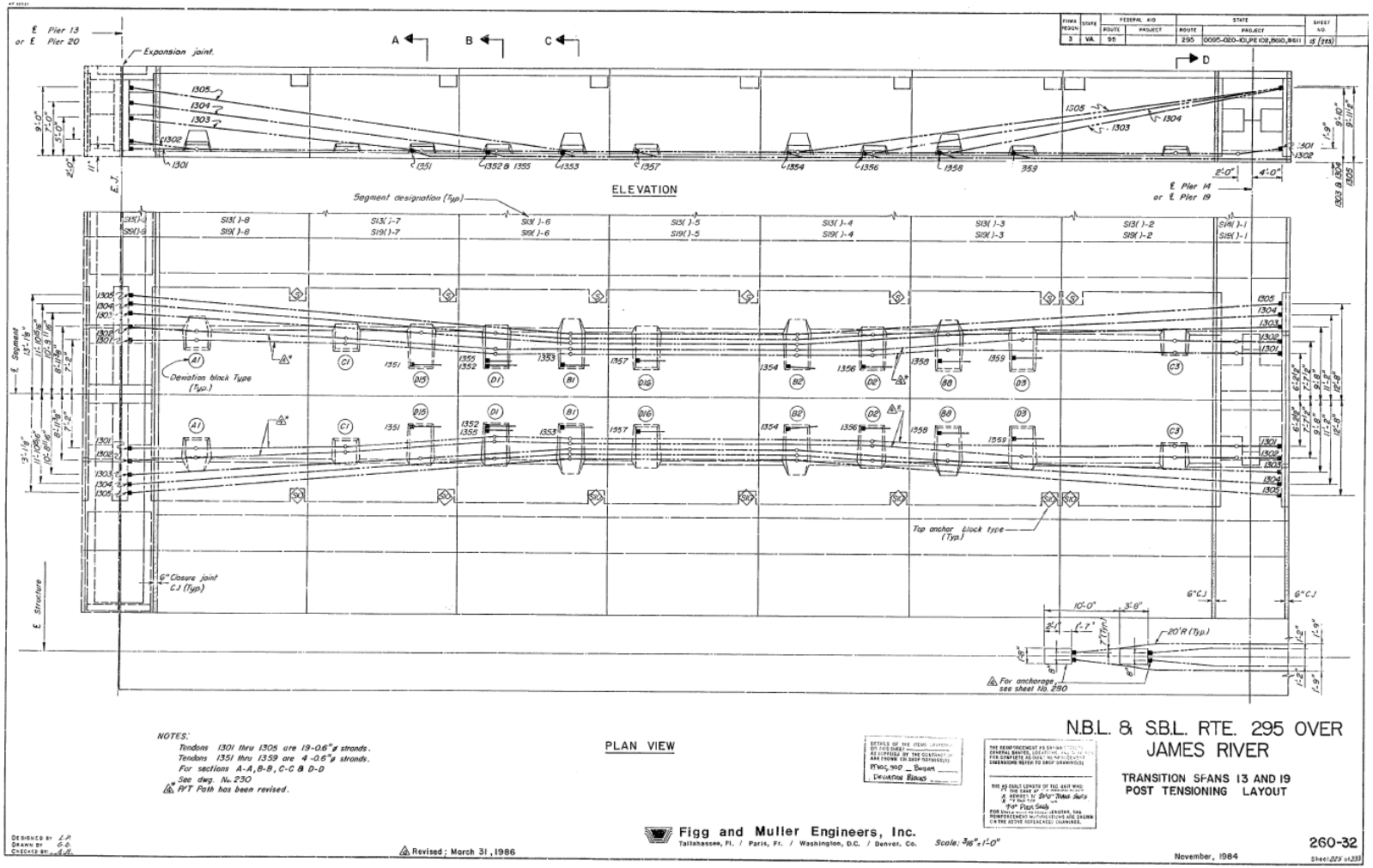

NOTES:
Tendons 1301 thru 1305 are 19-0.6"ϕ strands.
Tendons 1351 thru 1359 are 4-0.6"ϕ strands.
For sections A-A, B-B, C-C & D-D
See dwg. No. 230
Δ* P/T Path has been revised.

N.B.L. & S.B.L. RTE. 295 OVER JAMES RIVER

TRANSITION SPANS 13 AND 19 POST TENSIONING LAYOUT

Figg and Muller Engineers, Inc.
Tallahassee, Fl. / Paris, Fr. / Washington, D.C. / Denver, Co.

Scale: 3/16"=1'-0"

November, 1984

260-32

Sheet 225 of 333

Δ Revised; March 31, 1986

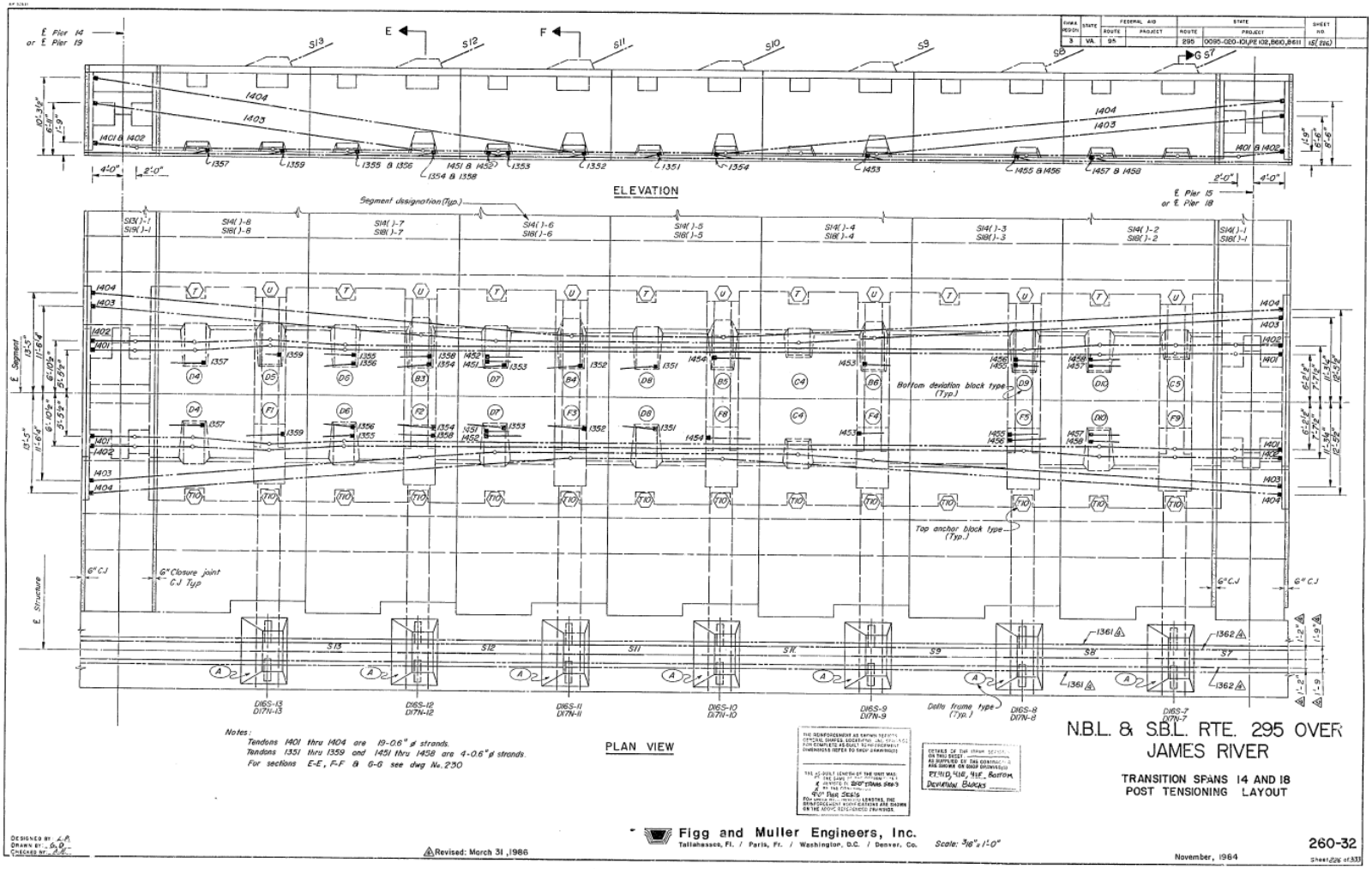
ELEVATION
PLAN VIEW
E Pier 14 or E Pier 19
E Pier 15 or E Pier 18
Segment designation (Typ.)
Bottom deviation block type (Typ.)
Top anchor block type (Typ.)
Drills frame type (Typ.)
Deviation Blocks
6" C.J
6" Closure joint C.J Typ
E Segment
E Structure
Notes:
Tendons 1401 thru 1404 are 19-0.6" ø strands.
Tendons 1351 thru 1359 and 1451 thru 1458 are 4-0.6" ø strands.
For sections E-E, F-F & G-G see dwg No. 230
N.B.L. & S.B.L. RTE. 295 OVER JAMES RIVER
TRANSITION SPANS 14 AND 18
POST TENSIONING LAYOUT
Figg and Muller Engineers, Inc.
Tallahassee, Fl. / Paris, Fr. / Washington, D.C. / Denver, Co.
Scale: 3/16"=1'-0"
November, 1964
260-32
Revised: March 31, 1986

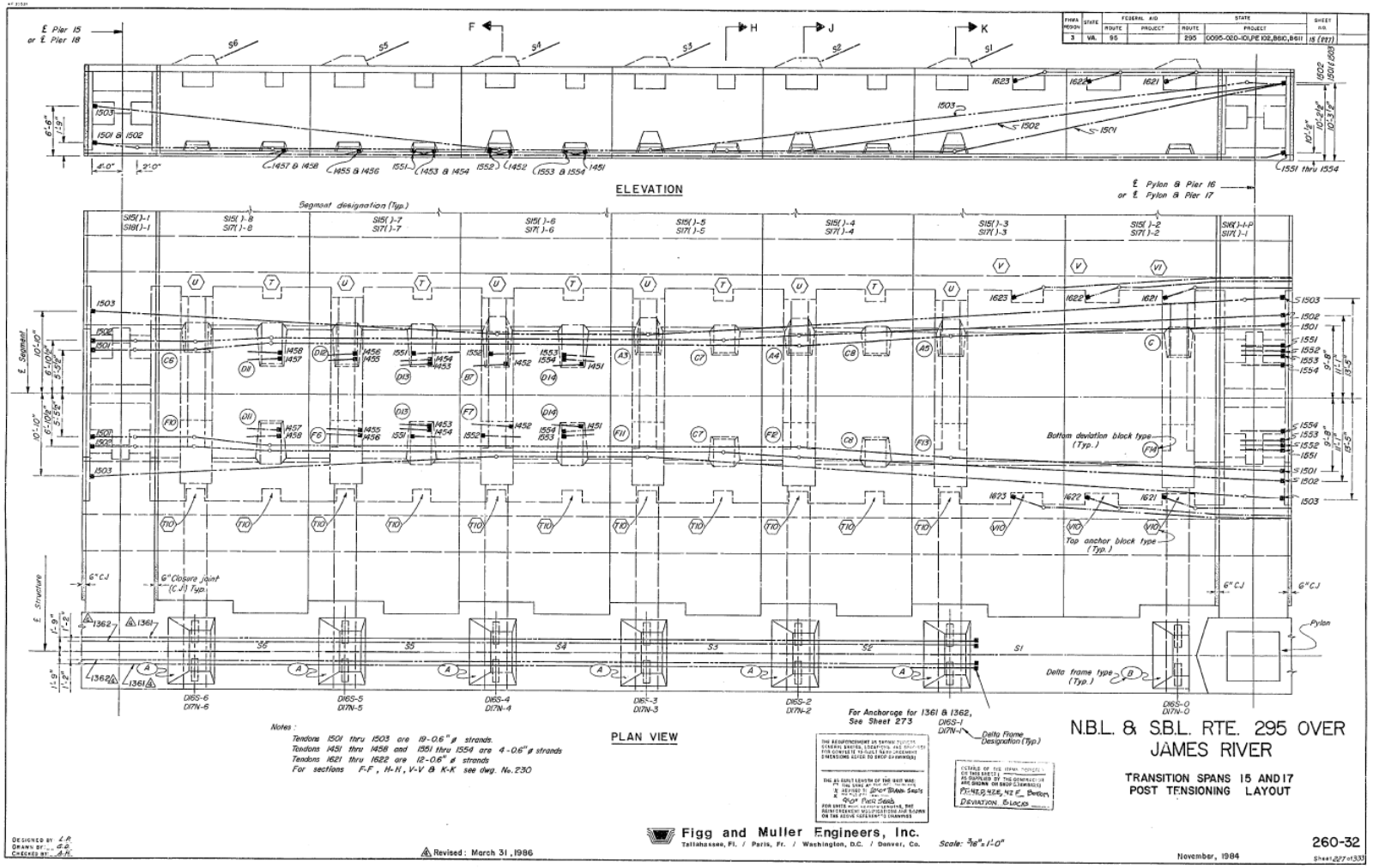
ELEVATION
PLAN VIEW
℄ Pier 15 or ℄ Pier 18
℄ Pylon 8 Pier 16 or ℄ Pylon 8 Pier 17
Segment designation (Typ.)
Bottom deviation block type (Typ.)
Top anchor block type (Typ.)
Delta frame type (Typ.)
Pylon
6" C.J
6" Closure joint (C.J) Typ.
℄ Segment
℄ Structure
For Anchorage for 1361 & 1362, See Sheet 273
Delta Frame Designation (Typ.)
Notes :
Tendons 1501 thru 1503 are 19-0.6" ø strands.
Tendons 1451 thru 1458 and 1551 thru 1554 are 4-0.6" ø strands
Tendons 1621 thru 1622 are 12-0.6" ø strands
For sections F-F, H-H, V-V & K-K see dwg. No. 230
N.B.L. & S.B.L. RTE. 295 OVER JAMES RIVER
TRANSITION SPANS 15 AND 17
POST TENSIONING LAYOUT
Figg and Muller Engineers, Inc.
Tallahassee, Fl. / Paris, Fr. / Washington, D.C. / Denver, Co.
Revised : March 31, 1986
Scale: 3/16" = 1'-0"
November, 1984
260-32
Sheet 227 of 333

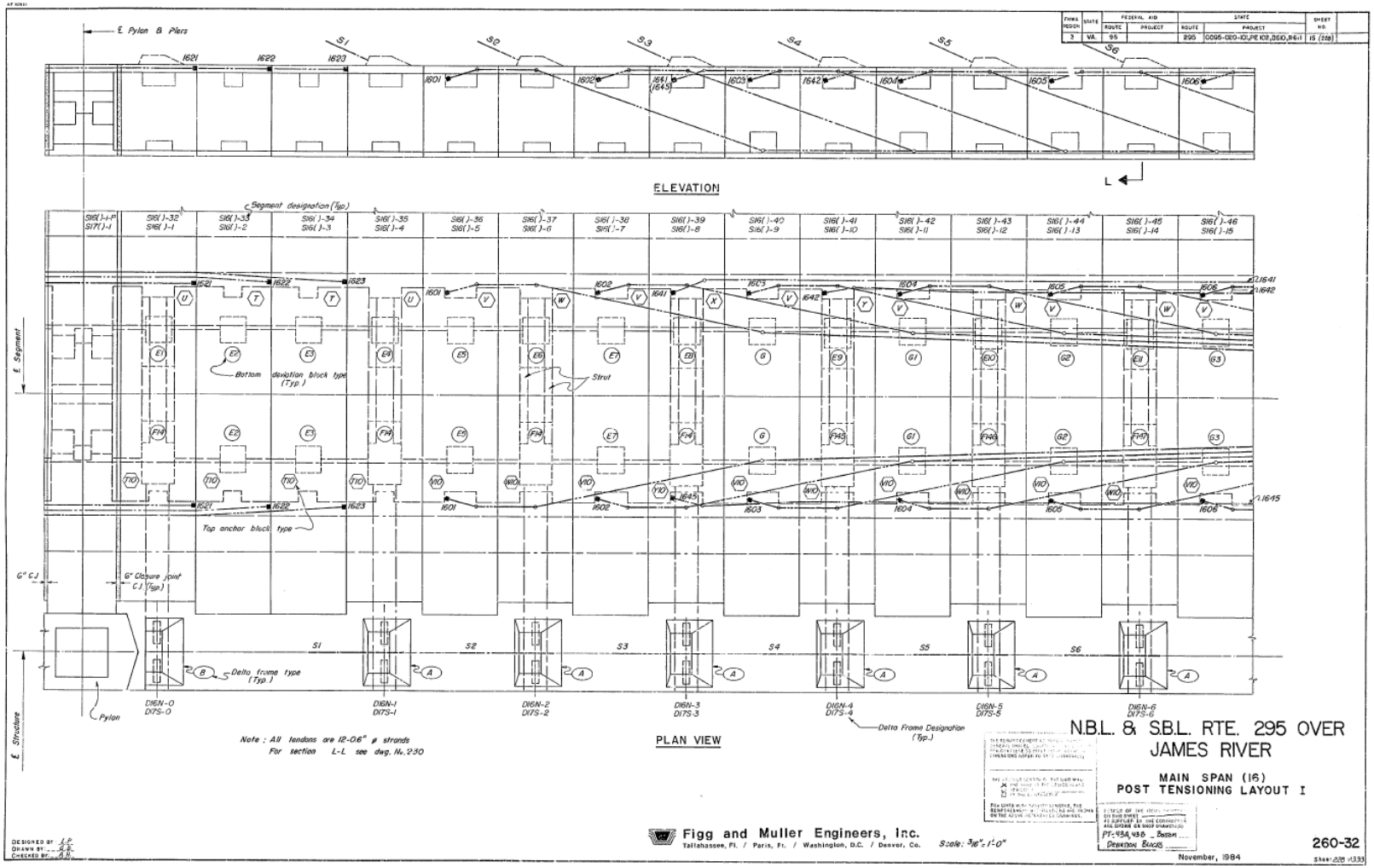

FHWA REGION	STATE	FEDERAL AID ROUTE	FEDERAL AID PROJECT	STATE ROUTE	STATE PROJECT	SHEET NO.
3	VA.	95		295	0095-020-101,PE 102,B610,B611	15 (228)

N.B.L. & S.B.L. RTE. 295 OVER JAMES RIVER

MAIN SPAN (16) POST TENSIONING LAYOUT I

Figg and Muller Engineers, Inc.
Tallahassee, Fl. / Paris, Fr. / Washington, D.C. / Denver, Co.

Scale: 3/16"=1'-0"

November, 1984

260-32

Sheet 226 of 333

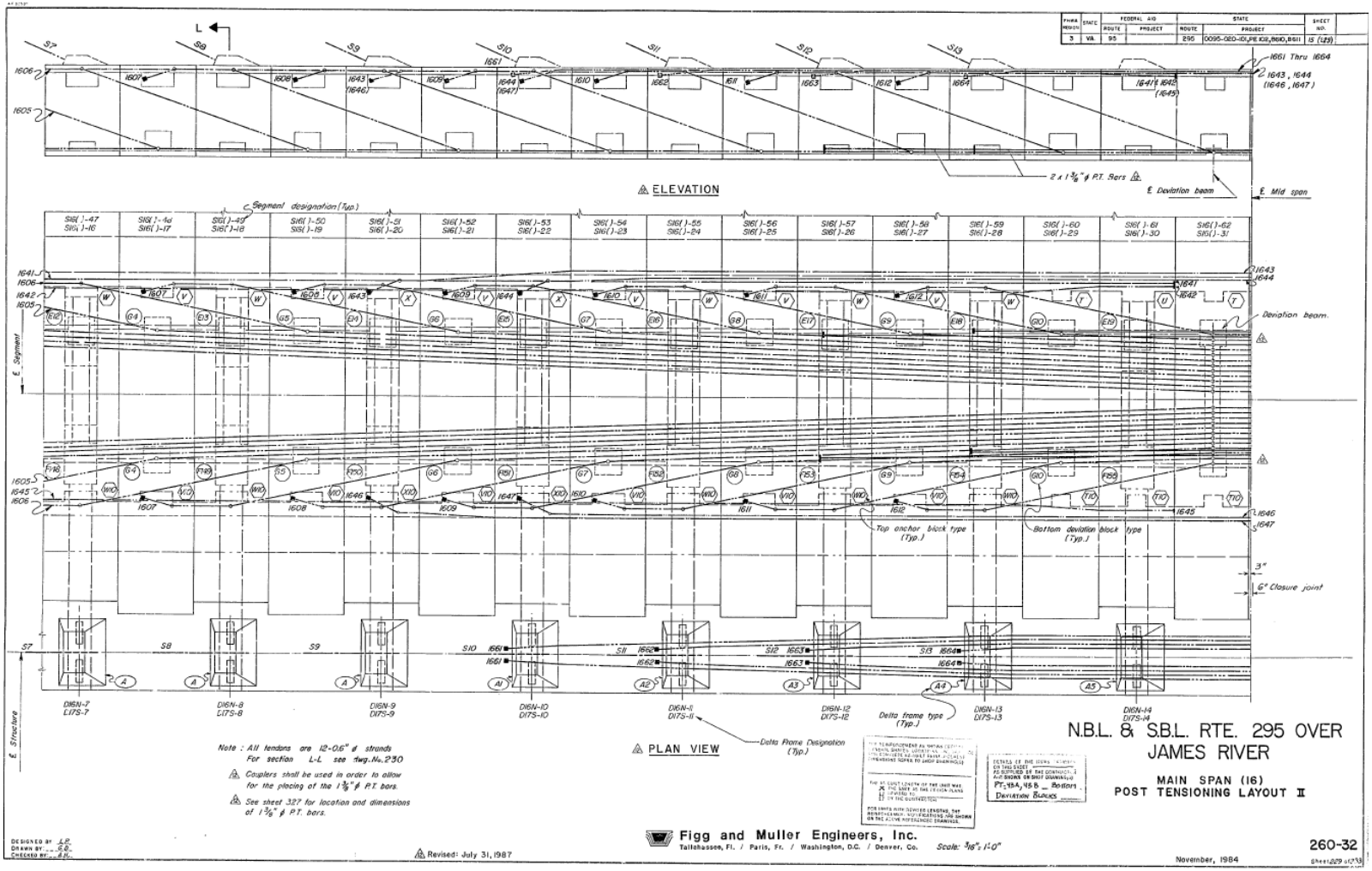
ELEVATION
PLAN VIEW
Segment designation (Typ.)
2 x 1 3/8" ϕ P.T. Bars
E Deviation beam
E Mid span
Deviation beam
Top anchor block type (Typ.)
Bottom deviation block type (Typ.)
3"
6" Closure joint
Delta frame type (Typ.)
Delta Frame Designation (Typ.)
E Segment
E Structure
Note : All tendons are 12-0.6" ϕ strands
For section L-L see Awg. No. 230
Couplers shall be used in order to allow for the placing of the 1 3/8" ϕ P.T. bars.
See sheet 327 for location and dimensions of 1 3/8" ϕ P.T. bars.
N.B.L. & S.B.L. RTE. 295 OVER JAMES RIVER
MAIN SPAN (16)
POST TENSIONING LAYOUT II
Figg and Muller Engineers, Inc.
Tallahassee, Fl. / Paris, Fr. / Washington, D.C. / Denver, Co.
Scale: 3/16"=1'-0"
November, 1984
260-32
Revised: July 31, 1987

FHWA REGION	STATE	FEDERAL AID ROUTE	FEDERAL AID PROJECT	STATE ROUTE	STATE PROJECT	SHEET NO.
3	VA.	95		295	0095-020-101,PE 102,B610,B611	15 (214)

TENDON SCHEDULE

Location	Tendon No.	Tendon Size	Tendon Length (Ft.)	Tendon Weight (Lbs)	Number of Tendon per Location	Number of Location	Total Weight (Lbs.)	Stressing Force (Kips)		Bars/Tendon SB0304	SB0501	SB0502	DB0501
Spans 13,19 (One girder)	1301	19-0.6"ϕ	153.23	2,154.4	2	4	17,235	844			2		
	1302		153.31	2,155.5			17,244						
	1303		154.28	2,169.2			17,354						
	1304		154.35	2,170.0			17,360						
	1305		154.51	2,172.4			17,379						
Spans 14,18 (One girder)	1401		158.19	2,224.6			17,794						
	1402		158.19	2,224.9			17,794						
	1403		158.97	2,235.1			17,881						
	1404		159.42	2,241.4			17,931						
Spans 15,17 (One girder)	1501		159.17	2,237.9			17,903						
	1502		158.83	2,233.1			17,865						
	1503	19-0.6"ϕ	159.05	2,236.2			17,890	844			2		
Spans 13 & 14 or 19 & 18 (One girder)	1351	4-0.6"ϕ	184.0	544.6			4,357	178		2			
	1352		164.0	485.4			3,883						
	1353		144.0	426.2			3,410						
	1354		104.0	307.8			2,462						
	1355		134.0	396.6			3,173						
	1356		84.0	248.6			1,989						
	1357		94.0	278.2			2,226						
	1358		84.0	248.6			1,989						
	1359		54.0	159.8			1,278						
Spans 14 & 15 or 18 & 17 (One girder)	1451		164.0	485.4			3,883						
	1452		154.0	455.8			3,646						
	1453		94.0	278.2			2,226						
	1454		114.0	337.4			2,699						
	1455		64.0	189.4			1,515						
	1456		64.0	189.4			1,515						
	1457		44.0	130.2			1,042						
	1458		44.0	130.2			1,042						
Span 15 (One girder)	1551		116.5	344.8			2,758						
	1552		106.5	315.2			2,522						
	1553		96.5	285.6			2,285						
	1554	4-0.6"ϕ	96.5	285.6			2,285	178		2			
Spans 15 & 16 or 17 & 16 (One girder)	1601	12-0.6"ϕ	87.75	2464			1,971	533				2	
	1602		87.75	494.0			3,392	533					
	1603		87.75	601.6		4	4,813	533					
	1601		541.0	4,804.1		2	19,216	562					
	1602		501.0	4,448.9			17,796						
	1603		461.0	4,093.7			16,375						
	1604		421.0	3,738.5			14,954						
	1605		381.0	3,383.3			13,533						
	1606		341.0	3,028.1			12,112						
	1607		301.0	2,672.9			10,692						
	1608		260.8	2,315.9			9,264						
	1609		220.8	1,960.7			7,843						
	1610		180.8	1,605.5			6,422						
	1611		140.6	1,250.3			5,001						
	1612		100.6	895.1	9	2	3,580	562					
	1641		257.75	2,022.4	1	4	8,090	533					
	1642		207.75	1,644.8		4	7,379						
	1643		235.5	2,041.2		2	4,182						
	1644		195.5	1736.0		2	3,472						
	1645		227.75	2,022.4		4	8,090						
	1646		235.5	2,091.2		2	4,182						
	1647		195.5	1736.0	1	2	3,472						
Span 16 (Closure strip)	1661		198.0	1758.2	2	1	3,516			2			
	1662		198.0	1,403.0		1	2,806			1			
	1663		118.0	1,047.8		1	2,096			1			
	1664	12-0.6"ϕ	78.0	692.6		1	1,385	533		2			
Expansion joint segment	A	4-0.6"ϕ	88.5	84.4		4	675	178		2			
	B		86.0	77.0		4	616						
	C		89.75	88.1		4	705						
	D		27.25	80.7	2	4	646						
Pier segment 14	14051		89.75	88.1	4	2	705						
	14052		89.25	86.6			693						
	14053		86.5	78.4			627						
	14054/14055		86.125	77.3			618						
Pier segment 15	15051		86.875	79.6			637						
	15052		89.25	86.6			693						
	15053		89.25	86.6			693						
	15054/15055		86.875	79.6			637						
Pier segment 16	16051		87.75	82.1			657						
	16052		89.89	86.6			693						
	16053	4-0.6"ϕ	86.75	79.2	4	2	634	178		2			

DESIGNED BY JC
DRAWN BY JCG
CHECKED BY AM

BAR BENDING DIAGRAMS

(All dimensions are out-to-out)

Mark	A	B	C	D
SS 0301	7"	3"	8"	7"
SS 0302	3"	3"	11.1"	7"

SS0301, SS0302

Mark	A	B	C
SB0304	10'5"	8"	1'8"
SB0501	11'3"	1'2"	2'6"
SB0502	2'3"	1'6"	3"
DB0502	2'3"	1'6"	3"
DB0501	1'2"	1'2"	2'3"

SB 0304, SB 0501, SB 0502, DB 0501, DB0502

BAR LIST

Mark	No.	Length	Pin ϕ	Location	Bent	Str.
SB0304	~~848~~	16'-9"	—	Segment	•	
SB0501	184	29'-4"	—		•	
SB0502	~~282~~	51'-10"	—		•	
DB0502	336	51'-10"	—		•	
SB0301	24	4'-9"	2⅛"		•	
SB0302	24	7'-0"	2⅛"	Segment	•	
	~~864~~ 216					
DB0501	16	29'-9"			•	

Length B Related Weight Shown on the Schedule

This length and related weight not included in the schedule

* ESTIMATED QUANTITIES

Item	Unit	Quantity
Epoxy Coated Reinforcing Steel	Lbs.	—
Reinforcing Steel	Lbs.	~~41,781~~ 41,516 ~~41,882~~

NOTE: * Reinforcing steel behind post tensioning anchorages is incidental to the post tensioning quantities.

Location	Tendon No.	Tendon Size	Tendon Length (Ft.)	Tendon Weight (Lbs.)	Number of Tendon per Location	Number of Location	Total Weight (Lbs.)	Stressing Force (Kips)		Bars/Tendon SB0304	SB0501	SB0502	SB0301	SB0302
Pier segment 16	16054/16055	4-0.6"ϕ	26.0	77.0	4	2	616	178		2				
Pier segment 17	17051		27.75	82.1			657							
	17052		29.25	86.6			693							
	17053		26.75	79.2			634							
	17054/17055		26.0	77.0			616							
Pier segment 18	18051		26.875	79.6			637							
	18052		29.25	86.6			693							
	18053		29.25	36.6			693							
	18054/18055		26.875	79.6			637							
Pier segment 19	19051		29.75	88.1			705							
	19052		29.25	86.6			693							
	19053		28.5	78.4			627							
	19054/19055	4-0.6"ϕ	26.125	77.3	4	2	618	178		2				
Delta frame	—	9-0.6"ϕ	55.33	368.5	9	2	42,746	400				2		
	—	12-0.6"ϕ	66.0	586.1	1	58	33,993	500				2		
Deviation beam	—	3-0.6"ϕ	18.0	40.0	3	4	480	133			2	2		
						Subtotal	555,120							
Post tensioning bar		1¼"ϕ PT bar	13.8	41.5	2	60	4,980	102						
Stay anchorage segment		1¼"ϕ PT bar	13.8	41.5	4	4	664	102						
Segment S16(1)-30 & 61	1													
Spans 13 & 19, 14 & 18, 15 & 17	1362	4-0.6"ϕ	283.8	940.0	2	2	3,360	178		2				
(Closure Strip)	1361	4-0.6"ϕ	298.6	883.9	2	2	3,535	178		2				
S16(1)-1 Thru 4 & 32 Thru 35		1¾"ϕ PT bar	40	222.4	3	4	2,668	166 *						
S16(1)-5 Thru 30 & 36 Thru 61		1¾"ϕ PT bar	20	111.2	3	104	34,694	166 *						
Seg. Mid Span (4)		1¾"ϕ PT bar	74' / 114'		2 / 2	2 / 2	3,136	189						

* See Sheets 229 & 273 for location.

Total weight tendons : ~~1,001,571 Lbs.~~ 1,008,466 Lbs.

Total weight P.T. bars : ~~5,222 Lbs. 42,586 Lbs.~~ 45,722 Lbs.

* After Anchor Set

N/A

N.B.L. & S.B.L. RTE. 295 OVER JAMES RIVER

MAIN SPAN UNIT
POST TENSIONING QUANTITIES

Figg and Muller Engineers, Inc.
Tallahassee, Fl. / Paris, Fr. / Washington, D.C. / Denver, Co.

Revised : July 31, 1987
Revised: April 20, 1987
Revised: March 25, 1987
Revised: March 31, 1986

November, 1984

260-32

Sheet 274 of 333

Appendix B. Original Main Span Construction Drawings

FHWA REGION	STATE	FEDERAL AID		STATE		SHEET NO.
		ROUTE	PROJECT	ROUTE	PROJECT	
3	VA.	95		295	0095-020-101,PE102,B610,B611	15(E86)

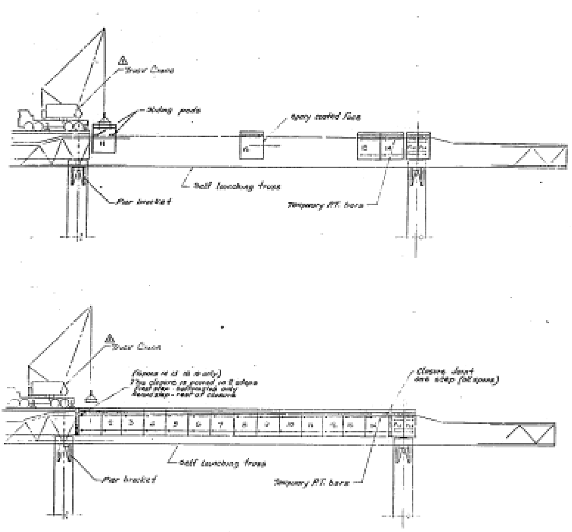

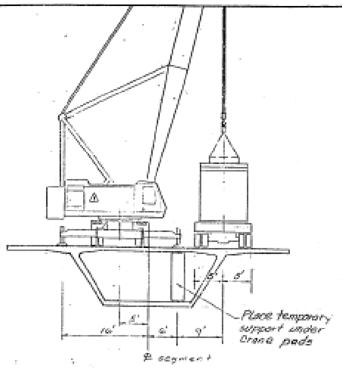

NOTE

(SPECIAL REQUIREMENT FOR PIER SEGMENTS 15 OR PIER SEGMENTS 18)

1. PLACE PIER SEGMENT ON TEMPORARY STEEL SHIMS ON THE MEDIAN SIDE OF BOX GIRDER (NEAR SIDE FROM BRIDGE CENTERLINE) AND ON DRY PACKED MORTAR PAD ON THE OUTSIDE (FAR SIDE FROM BRIDGE CENTERLINE) OF BOX GIRDER
2. STRESS THE 4 X 2 VERTICAL P.T. BARS ON THE OUTSIDE (FAR SIDE FROM BRIDGE CENTERLINE)
3. THIS CONDITION IS MAINTAINED DURING CONSTRUCTION INCLUDING STAY RE-STRESSING OPERATIONS AFTER CLOSURE AT MID SPAN
4. AFTER ALL STAY STRESSING OPERATIONS HAVE BEEN COMPLETED, REMOVE THE TEMPORARY STEEL SHIMS AND STRESS 1 X 2 VERTICAL P.T. BARS ON THE MEDIAN SIDE (NEAR SIDE FROM BRIDGE CENTERLINE) OF BOX GIRDER
5. DRY PACK THE 2 MORTAR PADS UNDER WEBS ON MEDIAN SIDE (NEAR FACE FROM BRIDGE CENTERLINE)
6. STRESS THE 3 X 2 REMAINING VERTICAL P.T. BARS ON THE MEDIAN SIDE (NEAR SIDE FROM BRIDGE CENTERLINE)

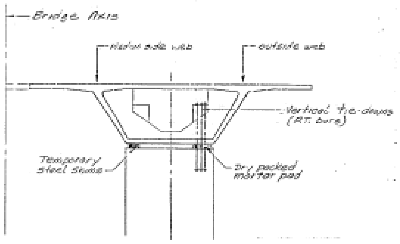

PHASE I (SPAN 13)

1. PLACE THE TWO SELF LAUNCHING TRUSSES, SUPPORTED ON EACH SIDE OF PIERS P-13 AND P 14 BY BRACKETS
2. POSITION CRANE AT END OF LAST SPAN COMPLETED
3. BRING SEGMENTS WITH TRUCK TRAILERS OVER THE DECK TO CRANE LIFTING STATION
4. STARTING BY THE PIER SEGMENT HALVES PLACE ALL THE SEGMENTS OF SPAN 13 BY SLIDING THEM INTO POSITION

4A. COAT MATCHING FACES OF BOTH PIER SEGMENTS WITH EPOXY AND STRESS TEMPORARY P.T. BARS

5. LEAVE GAP BETWEEN PIER SEGMENT AND SEGMENT 14 FOR C.I.P. CLOSURE JOINT.
6. INSTALL SHIMS BETWEEN PIER SEGMENT AND SEGMENT 14 TO MAINTAIN GAP
7. BRING SEGMENT 13. APPLY EPOXY ON ONE FACE OF MATCHING JOINT WITH 14 AND STRESS TOGETHER WITH P.T. BARS (4 BARS PER BOX, 2 TOP, 2 BOTTOM)
8. REPEAT THIS OPPERATION FOR ALL OTHER TYPICAL SEGMENTS
9. POUR CLOSURE JOINT AT EACH END OF SPAN
10. AFTER CLOSURE POUR HAS REACHED 3500 P.S.I. COMPRESSIVE STRENGTH, STRESS PERMANENT P.T. TENDONS (SEE TENDON LAYOUT)
11. PLACE PIER SEGMENT TEMPORARY BEARING AT CENTERLINE OF PIER 14
12. TEMPORARY P.T. BARS MAY BE REMOVED AND TRUSS RELEASED FROM SPAN LOAD BY DEFLATING JACKS ON PIER BRACKETS

PHASE II (SPAN 14)

1. MOVE CRANE TO END OF SPAN 13 AND POSITION IT ON TOP OF PIER 14
2. INSTALL THE THIRD SET OF PIER BRACKETS ON PIER 15
3. USING WINCH SYSTEM, ADVANCE TRUSS INTO POSITION OVER PIER 15. TRUSS IS READY TO ASSEMBLE SPAN 14 SEGMENTS
4. BRACKETS ON PIER 13 MAY NOW BE REMOVED AND RE-USED ON PIER 16
5. REPEAT PHASE I OPERATIONS 3 TO 9
6. POUR CLOSURE JOINT NEAR PIER 15
7. POUR CLOSURE JOINT AT BOTTOM SLAB ONLY NEAR PIER 14
8. AFTER CLOSURE POUR HAS REACHED 3500 P.S.I. COMPRESSIVE STRENGTH, STRESS PERMANENT LONGITUDINAL TENDONS NOS. 1351 THRU 1359
9. POUR REST OF CLOSURE JOINT NEAR PIER 14
10. AFTER THIS NEW CLOSURE CONCRETE HAS REACHED 3500 P.S.I. COMPRESSIVE STRENGTH, STRESS PERMANENT LONGITUDINAL TENDONS 1401 THRU 1404 AND STRESS ADDITIONAL P.T. BARS LOCATED AT TOP OF PIER SEGMENT P15 (8-1 3/8" BARS STRESSED AT 178K)
11. ALL OTHER TEMPORARY P.T. BARS MAY BE REMOVED EXCEPT P.T. BARS CONNECTING SEGMENT 14-7, 14-8, 14-9 CLOSE TO BOTTOM SLAB THAT REMAIN STRESSED AT 119K.
12. PLACE PIER SEGMENTS ON TOP OF PIER 15 ON TEMPORARY BEARINGS AT PIER CENTERLINE
13. MOVE CRANE TO END OF SPAN 14 AND POSITION IT OVER PIER 15
14. DRY PACK PERMANENT CONCRETE BEARING PADS AT PIER 14
15. INSTALL AND STRESS TIE-DOWNS BETWEEN PIER SEGMENTS P14 AND PIER CAP
16. STRESS VERTICAL P.T. TENDONS 1400I
17. RELEASE TRUSS

PHASE III (SPAN 15)

1. INSTALL EXTRA SET OF PIER BRACKET ON PIER 16
2. USING WINCH SYSTEM, ADVANCE TRUSS INTO POSITION OVER PIER 16
3. REPEAT OPERATION CYCLE 3 TO 9 OF PHASE I
4. POUR CLOSURE JOINT NEAR PIER 16
5. POUR CLOSURE JOINT AT BOTTOM SLAB ONLY NEAR PIER 15
6. AFTER CLOSURE POUR HAS REACHED 3500 P.S.I. COMPRESSIVE STRENGTH, STRESS PERMANENT LONGITUDINAL TENDONS NOS. 1451 THRU 1458
7. POUR REST OF CLOSURE JOINT NEAR PIER 15
8. AFTER THIS CONCRETE HAS REACHED 3500 P.S.I. COMPRESSIVE STRENGTH, STRESS PERMANENT LONGITUDINAL TENDONS NOS. 1501 THRU 1503.
9. STRESS TEMPORARY P.T. TENDONS 1551 THRU 1554
10. STRESS ADDITIONAL P.T. BARS LOCATED AT TOP SLAB CONNECTING THE FOLLOWING SEGMENTS 14-13, 14-14, 14P15, 15P15, 15-1, 15-2 (4 - 1 3/8" DIAMETER BARS STRESSED AT 178 K)
11. STRESS ADDITIONAL P.T. BARS LOCATED AT BOTTOM SLAB OF PIER SEGMENT 16
12. DRY PACK PERMANENT CONCRETE BEARING PADS ON PIER 15, FOLLOWING INSTRUCTIONS DESCRIBED IN NOTE A
13. DRY PACK PERMANENT CONCRETE BEARING PADS ON PIER 16
14. STRESS VERTICAL TIE-DOWNS (BARS STRESSED AT 166K) ON PIER 16
15. STRESS VERTICAL P.T. TENDONS NO. 1600I
16. SLACKEN AND REMOVE TEMPORARY P.T. BARS EXCEPT P.T. BARS MENTIONED AS ADDITIONAL IN OPERATIONS 10 AND 11
17. TEMPORARY TENDONS 1551 THRU 1554 MUST REMAIN STRESSED
18. RELEASE TRUSS FROM SPAN LOAD

PHASE IV (TWIN SPANS 13, 14, 15)

1. BRING BACK CRANE, ASSEMBLY TRUSS, AND ALL ERECTION EQUIPMENT TO PIER 13 (THIS SAME EQUIPMENT CAN BE RE-USED IN THE MEANWHILE FROM SPANS 1 THRU 12)
2. INSTALL TRUSS AND PROCEED WITH ERECTION OF THE TWIN SPANS BY REPEATING OPERATIONS DESCRIBED IN PHASES I THRU III

JR-450

The Equipment Schematics are for Information Only.
See Sheet 10 for General Notes.

N.B.L. & S.B.L. RTE. 295 OVER JAMES RIVER

MAIN STRUCTURE ERECTION SCHEME I

Designed by: L.P.

Figg and Muller Engineers, Inc.
Tallahassee, Fl. / Paris, Fr. / Washington, D.C. / Denver, Co.

△ Revised January 25, 1985

November, 1984

260-32

FHWA REGION	STATE	FEDERAL AID ROUTE	FEDERAL AID PROJECT	STATE ROUTE	STATE PROJECT	SHEET NO.
3	WA	90		295	0095-020-I-CL,PE 108,B&B,B411	(5/287)

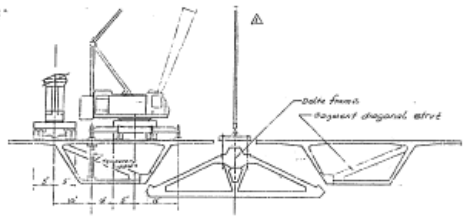

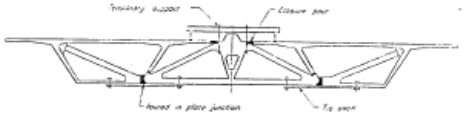

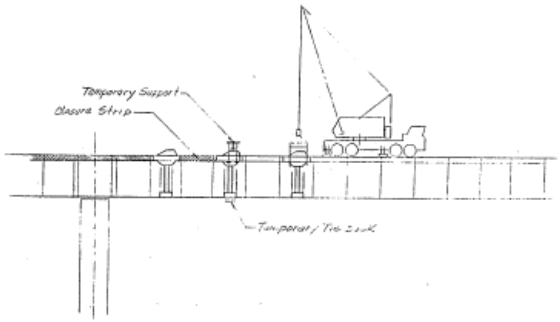

PHASE V

1. THE 3 SPAN TWIN STRUCTURE IS NOW COMPLETED, TRUSS MAY BE REMOVED
2. KEEP ON DECK HANDLING EQUIPMENT FOR DELTA FRAMES CONNECTING SEGMENTS OF SPANS 14 AND 15 TWIN STRUCTURE
3. BRING DELTA FRAME WITH TRAILER TRUCKS OVER THE DECK TO PROPER LOCATION TO BE LIFTED BY THE CRANE
4. USING THE CRANE LIFT AND ROTATE DELTA FRAME 90° ALLOWING IT TO BE LOWERED IN BETWEEN THE TWO STRUCTURES. ONCE THE DELTA FRAME IS BELOW DECK ROTATE IT BACK AND LIFT IT TO ITS FINAL POSITION
5. INSTALL TEMPORARY SUPPORT TO HOLD IT IN PLACE
6. POUR JUNCTION BETWEEN DELTA FRAME AND DIAGONAL STRUT INSIDE SEGMENTS
7. INSTALL FORMWORK UNDER SEGMENT FLANGES
8. POUR CONCRETE IN GAP BETWEEN DELTA FRAME AND SEGMENT ON EACH SIDE AT TOP SLAB LEVEL
9. AFTER THE CONCRETE OF DIAGONAL JUNCTION AND GAP AT TOP SLAB HAS REACHED 2500 P.S.I. COMPRESSIVE STRENGTH, STRESS CONTINUITY TRANSVERSE TENDON IN TOP SLAB (4-0.6" DIAMETER - TENDONS STRESSED AT 175 K)
10. THEN STRESS TRANSVERSE DIAGONAL TENDON ANCHORED IN SEGMENT BOTTOM SLAB (12 X 0.6" DIAMETER TENDON STRESSED AT 524 K)
11. REMOVE TEMPORARY SUPPORT FROM DELTA FRAME AND FORMWORK UNDER FLANGES
12. PROCEED TO ERECTION OF NEXT DELTA FRAME WITH THE SAME OPERATION PREVIOUSLY DESCRIBED
13. AFTER ALL DELTA FRAMES HAVE BEEN ERECTED INSTALL FORMWORK AND POUR CLOSURE STRIP REMAINING BETWEEN DELTA FRAMES AND THE FILL CLOSURE STRIP AT SPAN 13
14. STRESS ALL REMAINING TRANSVERSE CONTINUITY TENDONS ON SPANS 15 - 14 - 13.
15. REMOVE FORMWORK
16. CONSTRUCTION OF APPROACH IS NOW TERMINATED AND THE EQUIPMENT FOR CONSTRUCTION OF UPPER PART OF PYLON AND THE 630 FT MAIN SPAN CAN BE BROUGHT ON SITE OVER THE DECK.
    NOTE: LOW PART OF PYLON AND UPPER PART OF PYLON UP TO LAST SEGMENT BEFORE FIRST STAY CAN BE CONSTRUCTED DURING PHASES I THRU V. CANTILEVER SEGMENTS IN MAIN SPAN 16-1, 16-2, 16-3 CAN BE ERECTED AT END OF PHASES III AND IV, DURING WORK DESCRIBED IN PHASE V

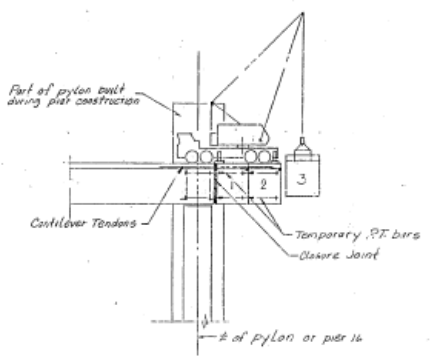

PHASE VI

1. THE 3 FIRST CANTILEVER SEGMENTS CAN BE BROUGHT OVER THE DECK BY TRAILER TRUCK, ALL THE OTHERS WILL BE ERECTED WITH BEAM AND WINCH METHOD.
2. POSITION CRANE ON TOP OF PIER 16
3. LIFT AND PLACE SEGMENT 16-1
4. PRIOR TO STRESSING TEMPORARY P.T. BARS BETWEEN 16-1 AND PIER SEGMENT P16 INSTALL SHIMS FOR CAST IN PLACE CLOSURE JOINT
5. ADJUST SEGMENT AND POUR CLOSURE CONCRETE
6. AFTER CONCRETE WAS REACHED 2500 P.S.I. COMPRESSIVE STRENGTH, STRESS CANTILEVER TENDON 16Z1 AT 533 K
   NOTE: SAME PRECEDING OPERATIONS CAN BE MADE SIMULTANEOUSLY OR SUCCESSIVELY ON TWIN GIRDER (TYPICAL TO ERECTION OF EACH SEGMENT)
7. AFTER BOTH SEGMENTS 16-1 ARE ERECTED AND CANTILEVER TENDONS ARE FULLY STRESSED MOVE CRANE OVER SEGMENT 16-1
8. LIFT AND PLACE SEGMENT 16-2 WITH CRANE
9. PRIOR TO ASSEMBLING WITH TEMPORARY P.T. BARS, APPLY EPOXY ON ONE FACE OF SEGMENT MATCHING WITH 16-1.
10. STRESS TEMPORARY P.T. BARS BETWEEN SEGMENT 16-1 AND SEGMENT 16-2 (FOR TEMPORARY P.T. BARS STRESSING AND AND SLACKENING SEE SPECIAL SHEETS 328 THRU 333.
11. REPEAT PRECEDING OPERATIONS 7-8-9-10 FOR ERECTION OF SEGMENTS 16-3

JR 830, 828

The Equipment Schematics are for Information Only. See Sheet 10 for General Notes.

N.B.L. & S.B.L. RTE. 295 OVER JAMES RIVER

MAIN STRUCTURE ERECTION SCHEME II

DESIGNED BY JP
DRAWN BY JC
CHECKED BY JP

Figg and Muller Engineers, Inc.
Tallahassee, Fl. / Paris, Fr. / Washington, D.C. / Denver, Co.

⚠ Revised: January 25,1985

November, 1984

260-32

Sheet(287+880)

FHWA REGION	STATE	FEDERAL AID ROUTE	FEDERAL AID PROJECT	STATE ROUTE	STATE PROJECT	SHEET NO
3	VA.	95		295	0095-020-101,PE102,B501,B511 (0/2188)	

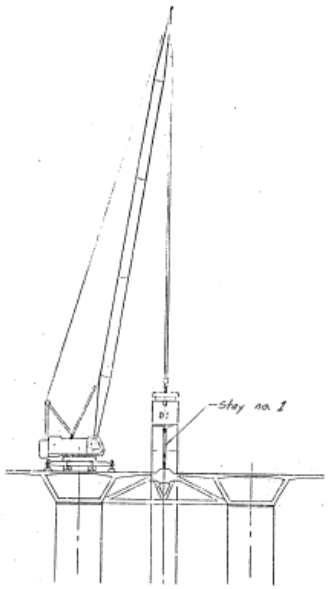

12. REMOVE CRANE FROM CANTILEVER
13. POSITION NEW CRANE NEAR PYLON FOR ERECTION OF STAYS AND PYLON SEGMENTS

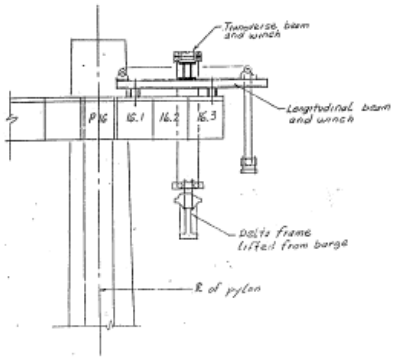

14. INSTALL BEAMS AND WINCHES EQUIPMENT ON BOTH GIRDERS OVER SEGMENTS 16-3
15. USING BEAM AND WINCH LIFT DELTA FRAME TYPE B FROM BARGE AND PLACE IT IN ITS PROPER POSITION NEAR PYLON
16. HOLD IT IN PLACE WITH TEMPORARY SUPPORT
17. CAST IN PLACE JUNCTION BETWEEN DELTA FRAME AND SEGMENT DIAGONALS
18. CAST IN PLACE GAP BETWEEN DELTA FRAME AND SEGMENT TOP SLAB EDGES
19. AFTER THIS CONCRETE HAS REACHED 2500 P.S.I. COMPRESSIVE STRENGTH, STRESS TOP SLAB TRANSVERSE CONTINUITY TENDONS THRU TOP OF DELTA FRAME
20. THEN STRESS TRANSVERSE DIAGONAL TENDONS ANCHORED AT BOTTOM SLAB OF SEGMENTS
21. RELEASE DELTA FRAME FROM TEMPORARY SUPPORT

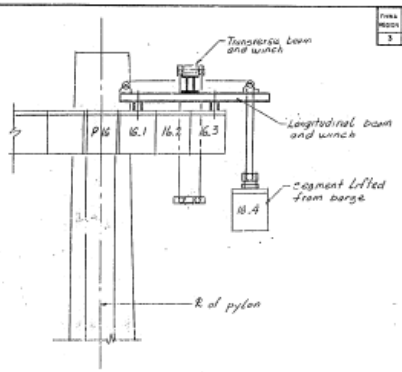

22. LIFT SEGMENTS 16-4 WITH BEAM AND WINCH
23. PRIOR TO ASSEMBLING WITH TEMPORARY P.T. BARS APPLY EPOXY ON ONE FACE MATCHING WITH SEGMENT ALREADY ERECTED
24. STRESS TEMPORARY P.T. BARS.
25. USING BEAM AND WINCH LIFT DELTA FRAME TYPE A AND PLACE IT IN ITS PROPER POSITION IN BETWEEN SEGMENTS 16-4
26. HOLD IT IN PLACE WITH TEMPORARY SUPPORT
27. CAST IN PLACE JUNCTION BETWEEN DELTA FRAME AND SEGMENT DIAGONALS
28. CAST IN PLACE GAP BETWEEN DELTA FRAME AND SEGMENT TOP SLAB EDGES AND CLOSURE STRIP BEHIND
29. AFTER THIS CONCRETE HAS REACHED 2500 P.S.I. COMPRESSIVE STRENGTH, STRESS TOP SLAB TRANSVERSE CONTINUITY TENDON THRU TOP OF DELTA FRAME AND CLOSURE STRIP BEHIND
30. THEN STRESS TRANSVERSE DIAGONAL TENDON ANCHORED AT BOTTOM SLAB OF SEGMENTS
31. REMOVE TEMPORARY SUPPORT FROM DELTA FRAME

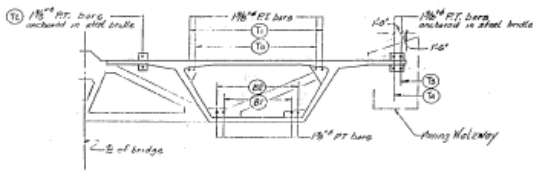

Main Span Temporary P.T. bar Location

SEE SHEETS 328 THRU 333 FOR INSTALLATION AND REMOVAL OF P.T. BARS.

JR 880,821

The Equipment Schematics are for Information Only. See Sheet 10 for General Notes.

N.B.L. & S.B.L. RTE. 295 OVER JAMES RIVER

MAIN STRUCTURE ERECTION SCHEME III

DESIGNED BY LP
DRAWN BY
CHECKED BY

Figg and Muller Engineers, Inc.
Tallahassee, Fl. / Paris, Fr. / Washington, D.C. / Denver, Co.

November, 1984

260-32

Sheet 289 of 333

FROM FEDERAL	STATE	FEDERAL AID ROUTE	FEDERAL AID PROJECT	STATE ROUTE	STATE PROJECT	SHEET NO
3	VA	95		295	(095-080-101,PE 100,B661,B611	260(32)

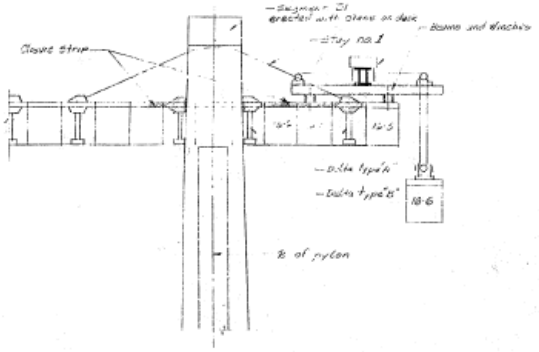

32. BRING STAY NO. 1 OVER THE DECK AND THREAD BOTH ENDS THRU THEIR ANCHORAGES IN DELTA FRAMES
33. USING CRANE POSITIONED NEAR PYLON LIFT STAY NO. 1 AND PLACE IT IN ITS SADDLE PROVIDED IN PYLON SEGMENT C (SEGMENT C WAS ERECTED DURING CONSTRUCTION PHASES OF LOWER PART OF PYLON) AND STRESS STAY NO. 1 FROM BOTH ENDS (SEE SCHEDULE FOR STAY STRESSING FORCES)
34. APPLY EPOXY ON TOP OF PYLON SEGMENT C, LIFT AND PLACE PYLON SEGMENT D1 ON TOP OF PYLON SGMENT C AND STRESS TEMPORARY P.T. BARS.
35. USING BEAM AND WINCH, LIFT CANTILEVER SEGMENTS 16-5, 16-6 AND ASSEMBLE IT WITH THE SAME PROCEDURE DESCRIBED PREVIOUSLY IN OPERATIONS 21-22-23-24
36. LIFT AND PLACE DELTA FRAME CONNECTING WITH SEGMENTS 16-6 WITH THE SAME PROCEDURE DESCRIBED IN OPERATIONS 25-26 AND BE FOLLOWED WITH OPERATIONS 27, 28, 29, 30, 31
37. BRING STAY NO. 2 AND REPEAT SAME OPERATIONS AS FOR STAY NO. 1
38. APPLY EPOXY ON TOP OF PYLON SEGMENT D1 AND PLACE PYLON SEGMENT D2
39. STRESS TEMPORARY P.T. BARS
40. REPEAT FULL OPERATION CYCLE FOR ERECTING ALL OTHER CANTILEVER SEGMENTS, STAYS AND PYLON SEGMENTS UNTIL CANTILEVER SEGMENTS 16-30, STAY NO. 13 AND PYLON SEGMENT "E" IS ERECTED
41. STRESS VERTICAL P.T. TENDON IN PYLON FROM TOP OF PYLON SEGMENT "E" AND INSTALL PYLON CAP
42. INSTALL AND STRESS DECK TENDONS 16A1, 16A2, 16A8, AT 535 K
43. ERECT CANTILEVER SEGMENT 31

STAY	F STAY
1	1184 K
2	1645 K
3	1726 K
4	1620 K
5	1599 K
6	1551 K
7	1552 K
8	1557 K
9	1571 K
10	1564 K
11	1605 K
12	1633 K
13	1662 K

STAY STRESSING

FOR SEQUENCE OF STAY STRESSING, REFER TO SHEETS 328 THRU 335.

RESTRESS THE STAYS TO THE FOLLOWING FORCES

STAY		
1	~~2370 K~~	NO RESTRESSING
2	~~2370 K~~	2370 K
3	~~2370 K~~	2370 K
4	~~2370 K~~	2370 K
5	~~2370 K~~	2340 K
6	~~2370 K~~	2310 K
7	~~2370 K~~	2280 K
8	~~2370 K~~	2200 K
9	~~2370 K~~	2120 K
10	~~2370 K~~	2020 K
11	~~2370 K~~	1920 K
12	~~2370 K~~	1820 K
13	~~2370 K~~	~~2080 K~~ 2050 K

LETTER OF THE ITEMS CONTAINED ON THIS SHEET ARE IN NOTES OF 13 AS SUPPLIED BY THE CONTRACTOR AFTER AWARD OF BRIDGE CONTRACT

JK 8/21/86

The Equipment Schematics are for Information Only. See Sheet 10 for General Notes.

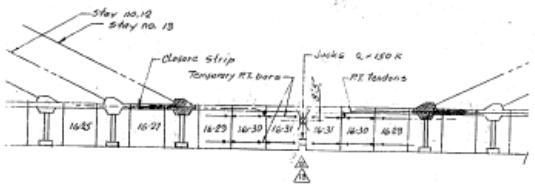

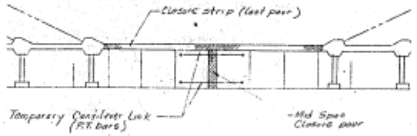

44. THE SOUTH CANTILEVER OF THE MAIN SPAN IS NOW COMPLETED AND ERECTION EQUIPMENT CAN BE REMOVED
THE NORTH CANTILEVER OF THE MAIN SPAN AND THE TRANSITION SPANS 17-18-19 ARE TO BE CONSTRUCTED THE SAME WAY AS THE SOUTH SIDE BY REPEATING ALL OPERATIONS OF PHASES I TO VI.
45. LINE UP NORTH AND SOUTH CANTILEVER. INSTALL JACKS IN CLOSURE GAP AT MID SPAN
46. INFLATE JACKS TO OBTAIN 300 K FOR A TOTAL OF 2 JACKS PER BOX GIRDER (SEE SKETCH FOR JACK LOCATION)
47. PLACE SHIM (AS SHOWN ON SKETCH) RELEASE JACKS AND REMOVE THEM
48. USE P.T. BARS TO LINK BOTH CANTILEVERS TEMPORARILY

46. INSTALL FORMWORK AND POUR MIDSPAN CLOSURE GAP
~~49. AFTER MID SPAN CLOSURE HAS REACHED 3500 P.S.I. COMPRESSIVE STRENGTH, INSTALL DECK CONTINUITY TENDONS AND PERMANENT P.T. BARS AND STRESS THEM IN THIS ORDER: 1601, 1602, 1603, PERMANENT PT. BARS (2 PER WEB), 1604, 1605 AND BALANCE OF TENDONS.~~
51. SLACKEN AND REMOVE REMAINING TEMPORARY P.T. BARS
52. GROUT ALL TENDONS
53. AFTER TRAFFIC BARRIER AND CONCRETE OVERLAY HAVE BEEN COMPLETED RE STRESS ALL STAYS TO THEIR FINAL FORCES (SEE SCHEDULE)
50. AFTER MID SPAN CLOSURE HAS REACHED 4500 P.S.I. COMPRESSIVE STRENGTH, INSTALL DECK CONTINUITY TENDONS AND PERMANENT P.T. BARS AND STRESS THEM IN THIS ORDER: 1601, 1602, 1603, PERMANENT PT. BARS (2 PER WEB), 1604, 1605 AND BALANCE OF TENDONS.

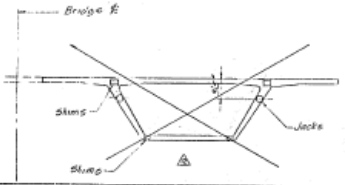

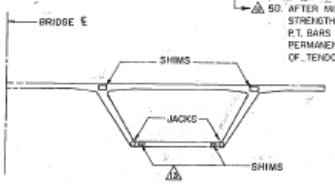

N.B.L. & S.B.L. RTE. 295 OVER JAMES RIVER

MAIN STRUCTURE ERECTION SCHEME IV

DESIGNED BY L.P.
DRAWN BY ...
CHECKED BY ...

Figg and Muller Engineers, Inc.
Tallahassee, Fl. / Paris, Fr. / Washington, D.C. / Genoa, Co.

Revised: August 21, 1987
Revised: July 31, 1987

November, 1984

260-32

GENERAL NOTES

1. THE ERECTION SEQUENCE WHICH FOLLOWS DEPICTS THE PROGRESSIVE CANTILEVER CONSTRUCTION OF THE MAINSPAN BEGINNING AT PIER 16. THE SEQUENCE OF ERECTION IS IDENTICAL FOR MAINSPAN CONSTRUCTION BEGINNING AT PIER 17.
2. COUPLERS AND ANCHOR PLATES FOR P.T. BARS ARE DENOTED AS:

PLATE —— COUPLER

3. PERMANENT P.T. TENDON NUMBERS ARE AS DESIGNATED IN THE POST-TENSIONING DRAWINGS.
4. FOR LOCATION AND DESIGNATION OF TEMPORARY P.T. BARS SEE SHEET 327.
5. CABLE STAYS WHICH ARE CONTINUOUS THROUGH THE PYLON, SHALL BE STRESSED SIMULTANEOUSLY AT BOTH ENDS

FHWA REGION	STATE	FEDERAL AID ROUTE	FEDERAL AID PROJECT	STATE ROUTE	STATE PROJECT	SHEET NO
3	VA	95		295	0095-020-10,PE102,B610,B611	15(208)

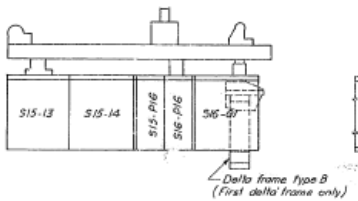

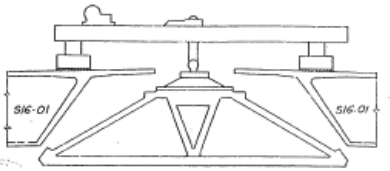

PHASE 2- DELTA FRAME ASSEMBLY

(CONSTRUCTION PHASES IDENTICAL FOR ALL DELTA FRAMES IN MAIN SPAN)

(A) LIFT DELTA FRAME FROM BARGE
(B) POUR CAST IN PLACE JOINTS IN TOP SLAB AND PLACE PACK MORTAR AT DELTA FRAME/SEGMENT BOTTOM CONNECTION
(C) WHEN CIP CONCRETE STRENGTH REACHES 3500 PSI, STRESS ALL TRANSVERSE TOP SLAB CONTINUITY TENDONS AND DELTA FRAME TRANSVERSE POST-TENSIONING OF SEGMENTS S16-01.

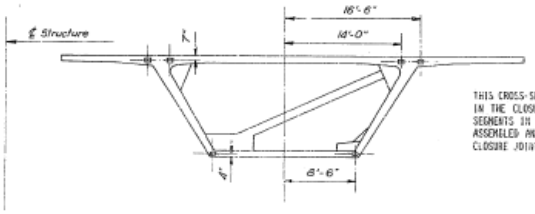

THIS CROSS-SECTION SHOWS THE LOCATION OF 6 - 6" X 8" SHIMS PLACED IN THE CLOSURE JOINTS BETWEEN THE PIER SEGMENTS AND THE FIRST SEGMENTS IN CANTILEVER. ONCE THE FIRST CANTILEVER SEGMENTS ARE ASSEMBLED AND ORIENTED TO GIVE THE FINAL ROADWAY ALIGNMENT, THE CLOSURE JOINTS ARE POURED.

LOCATION OF SHIMS

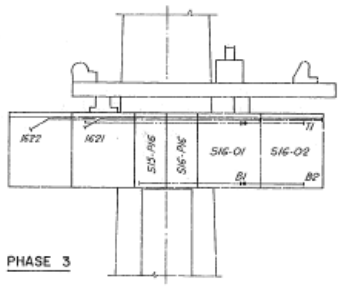

PHASE 3

(A) MOVE BEAM AND WINCH TO SEGMENTS S16-01
(B) LIFT SEGMENTS S16-02 FROM BARGE
(C) COUPLE AND STRESS P.T. BARS T1 AND B2 IN SEGMENT S16-02
(D) STRESS TENDONS 1622
(E) STRESS P.T. BARS B1 BETWEEN SEGMENTS S15-P16 AND S16-01

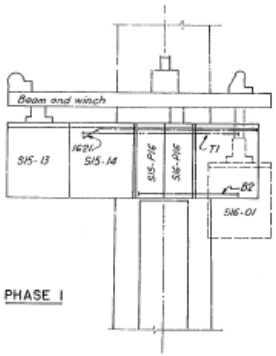

PHASE 1

(A) ASSEMBLE BEAM AND WINCH ABOVE PIER 16
(B) SECURE SHIMS TO FREE FACE OF SEGMENTS S16-P16
(C) LIFT SEGMENTS S16-01 WITH BEAM AND WINCH FROM BARGE
(D) STRESS P.T. BARS T1 BETWEEN SEGMENTS S15-14 AND S16-01 AND P.T. BARS B2 BETWEEN SEGMENTS S15-P16 AND S16-01
(E) ADJUST SEGMENTS S16-01 TO REQUIRED ELEVATIONS
(F) POUR CLOSURE JOINTS
(G) WHEN CIP JOINT CONCRETE STRENGTH HAS REACHED 2500 PSI STRESS TENDONS 1621 FROM CANTILEVER END.

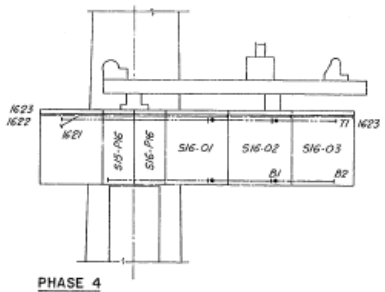

PHASE 4

JR-820

(A) ADVANCE BEAM AND WINCH TO SEGMENTS 16-02
(B) LIFT SEGMENTS S16-03 FROM BARGE
(C) COUPLE AND STRESS P.T. BARS T1 AND B2 IN SEGMENTS S16-03
(D) STRESS TENDONS 1623
(E) COUPLE AND STRESS P.T. BARS B1 IN SEGMENTS S16-02

The Equipment Schematics are for Information Only See Sheet 10 for General Notes.

N.B.L. & S.B.L. RTE. 295 OVER JAMES RIVER

MAIN SPAN ERECTION SEQUENCE I

DESIGNED BY J.P.
DRAWN BY J.B.
CHECKED BY J.C.

Figg and Muller Engineers, Inc.
Tallahassee, Fl. / Paris, Fr. / Washington, D.C. / Denver, Co.

No scale

November, 1984

260-32

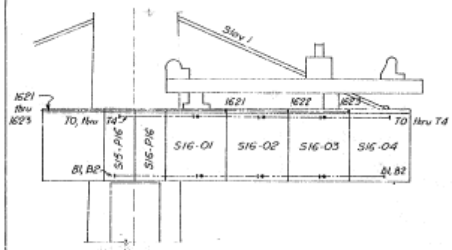

PHASE 5

(A) ADVANCE BEAM AND WINCH TO SEGMENTS S16-03
(B) LIFT SEGMENTS S16-04 FROM BARGE
(C) COUPLE AND STRESS P.T. BARS T1 AND B2 IN SEGMENTS S16-04
(D) STRESS P.T. BARS T0, T2, T3, T4 FROM SEGMENTS S15-P16 TO SEGMENTS S16-04
(E) COUPLE AND STRESS P.T. BAR B1 IN SEGMENTS S16-04
(F) LIFT DELTA FRAME OF SEGMENTS S16-04
(G) PLACE DRY PACKED MORTAR BETWEEN DELTA FRAME AND SEGMENT WEBS
(H) POUR CIP CONCRETE CLOSURE IN TOP SLAB FOR SEGMENTS S16-02, S16-03, S16-04
(I) WHEN THE CIP CONCRETE REACHES A MINIMUM COMPRESSIVE STRENGTH OF 3500 PSI, STRESS THE 1200.6" STRAND TENDON OF THE DELTA FRAME AND ALL TRANSVERSE CONTINUITY POST TENSIONING OF SEGMENTS S16-02, S16-03, S16-04
(J) ASSEMBLE STAY 1 AND STRESS TO 1480 KIPS
(K) REMOVE P.T. BARS T1 FROM SEGMENTS S15-14

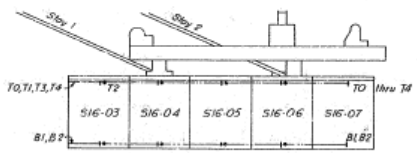

PHASE 8

(A) ADVANCE BEAM AND WINCH TO SEGMENTS S16-06
(B) LIFT SEGMENTS S16-07 FROM BARGE
(C) COUPLE AND STRESS P.T. BARS T3 AND B2 IN SEGMENTS S16-07
(D) COUPLE AND STRESS P.T. BARS T0, T2, T3, T4 IN SEGMENTS S16-07
(E) COUPLE AND STRESS P.T. BAR B1 IN SEGMENTS S16-07

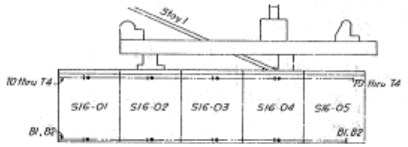

PHASE 6

(A) ADVANCE BEAM AND WINCH TO SEGMENTS S16-04
(B) LIFT SEGMENTS S16-05 FROM BARGE
(C) COUPLE AND STRESS P.T. BARS T1 AND B2 IN SEGMENTS S16-05
(D) COUPLE AND STRESS P.T. BARS T0, T2, T3, T4 IN SEGMENTS S16-05
(E) COUPLE AND STRESS P.T. BARS B1 IN SEGMENTS S16-05

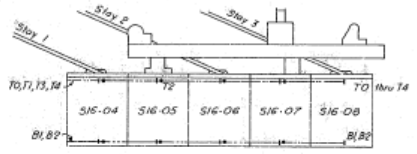

PHASE 9

(A) ADVANCE BEAM AND WINCH TO SEGMENTS S16-07
(B) LIFT SEGMENTS S16-08 FROM BARGE
(C) COUPLE AND STRESS P.T. BARS T3 AND B2 IN SEGMENTS S16-08
(D) COUPLE AND STRESS P.T. BARS T0, T2, T3, T4 IN SEGMENTS S16-08
(E) COUPLE AND STRESS P.T. BAR B1 IN SEGMENTS S16-08
(F) LIFT DELTA FRAME OF SEGMENTS S16-08
(G) PLACE DRY PACKED MORTAR BETWEEN DELTA FRAME AND SEGMENT WEBS
(H) POUR CIP CONCRETE CLOSURE IN TOP SLAB FOR SEGMENTS S16-07 AND S16-08
(I) WHEN THE CIP CONCRETE REACHES A MINIMUM COMPRESSIVE STRENGTH OF 3500 PSI, STRESS THE 1200.6" STRAND TENDON OF THE DELTA FRAME AND ALL TRANSVERSE CONTINUITY POST TENSIONING OF SEGMENTS S16-07 AND S16-08
(J) ASSEMBLE STAY 3 AND STRESS TO 1480 KIPS
(K) REMOVE P.T. BARS T2 FROM SEGMENTS S16-03 THRU S16-04

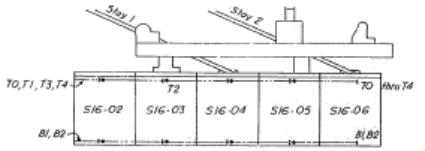

PHASE 7

(A) ADVANCE BEAM AND WINCH TO SEGMENTS S16-05
(B) LIFT SEGMENTS S16-06 FROM BARGE
(C) COUPLE AND STRESS P.T. BARS T1 AND B2 IN SEGMENTS S16-06
(D) COUPLE AND STRESS P.T. BARS T0, T2, T3, T4 IN SEGMENTS S16-06
(E) COUPLE AND STRESS P.T. BAR B1 IN SEGMENTS S16-06
(F) LIFT DELTA FRAME OF SEGMENTS S16-06
(G) PLACE DRY PACKED MORTAR BETWEEN DELTA FRAME AND SEGMENT WEBS
(H) POUR CIP CONCRETE CLOSURE IN TOP SLAB FOR SEGMENTS S16-05 AND S16-06
(I) WHEN THE CIP CONCRETE REACHES A MINIMUM COMPRESSIVE STRENGTH OF 3500 PSI, STRESS THE 1200.6" STRAND TENDON OF THE DELTA FRAME AND ALL TRANSVERSE CONTINUITY POST TENSIONING OF SEGMENTS S16-05 AND S16-06
(J) ASSEMBLE STAY 2 AND STRESS TO 1480 KIPS
(K) REMOVE P.T. BARS T2 FROM SEGMENTS S15-P16 THRU S16-02

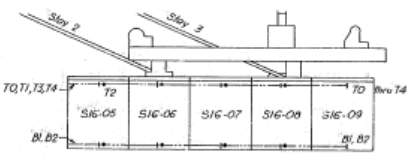

PHASE 10

JR-921

(A) ADVANCE BEAM AND WINCH TO SEGMENTS S16-08
(B) LIFT SEGMENTS S16-09 FROM BARGE
(C) COUPLE AND STRESS P.T. BARS T2 AND B2 IN SEGMENTS S16-09
(D) COUPLE AND STRESS P.T. BARS T0, T2, T3, T4 IN SEGMENTS S16-09
(E) COUPLE AND STRESS P.T. BAR B1 IN SEGMENTS S16-05

The Equipment Schematics are for Information Only. See Sheet 10 for General Notes.

N.B.L. & S.B.L. RTE. 295 OVER JAMES RIVER

MAIN SPAN ERECTION SEQUENCE II

Figg and Muller Engineers, Inc.
Tallahassee, Fl. / Paris, Fr. / Washington, D.C. / Denver, Co.

No scale

November, 1984

260-32

FHWA REGION	STATE	FEDERAL AID ROUTE	FEDERAL AID PROJECT	STATE ROUTE	STATE PROJECT	SHEET NO
3	VA	95		295	0099-020-101,PE 102,B660,B611	15 (380)

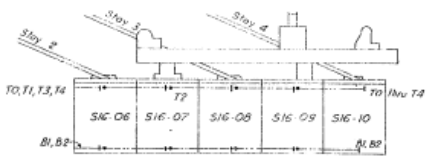

PHASE 11

(A) ADVANCE BEAM AND WINCH TO SEGMENTS S16-09
(B) LIFT SEGMENTS S16-10 FROM BARGE
(C) COUPLE AND STRESS P.T. BARS T1 AND B2 IN SEGMENTS S16-10
(D) COUPLE AND STRESS P.T. BARS T0, T2, T3, T4 IN SEGMENTS S16-10
(E) COUPLE AND STRESS P.T. BAR B1 IN SEGMENTS S16-10
(F) LIFT DELTA FRAME OF SEGMENTS S16-10
(G) PLACE DRY PACKED MORTAR BETWEEN DELTA FRAME AND SEGMENT WEBS
(H) POUR CIP CONCRETE CLOSURE IN TOP SLAB FOR SEGMENTS S16-09 AND S16-10
(I) WHEN THE CIP CONCRETE REACHES A MINIMUM COMPRESSIVE STRENGTH OF 3500 PSI, STRESS THE 12X0.6" STRAND TENDON OF THE DELTA FRAME AND ALL TRANSVERSE CONTINUITY POST TENSIONING OF SEGMENTS S16-09 AND S16-10
(J) ASSEMBLE STAY 4 AND STRESS TO 1480 KIPS
(K) REMOVE P.T. BARS T2 FROM SEGMENTS S16-05 THRU S16-06. REMOVE P.T. BARS T3 AND T4 FROM SEGMENTS S15-P16 THROUGH S16-02.

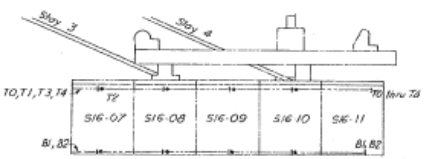

PHASE 12

(A) ADVANCE BEAM AND WINCH TO SEGMENTS S16-10
(B) LIFT SEGMENTS S16-11 FROM BARGE
(C) COUPLE AND STRESS P.T. BARS T1 AND B2 IN SEGMENTS S16-11
(D) COUPLE AND STRESS P.T. BARS T0, T2, T3, T4 IN SEGMENTS S16-11
(E) COUPLE AND STRESS P.T. BAR B1 IN SEGMENTS S16-11

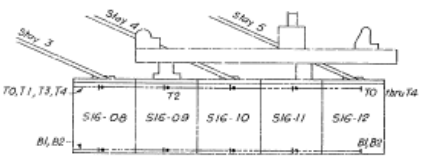

PHASE 13

(A) ADVANCE BEAM AND WINCH TO SEGMENTS S16-11
(B) LIFT SEGMENTS S16-12 FROM BARGE
(C) COUPLE AND STRESS P.T. BARS T1 AND B2 IN SEGMENTS S16-12
(D) COUPLE AND STRESS P.T. BARS T0, T2, T3, T4 IN SEGMENTS S16-12
(E) COUPLE AND STRESS P.T. BAR B1 IN SEGMENTS S16-12
(F) LIFT DELTA FRAME OF SEGMENTS S16-12
(G) PLACE DRY PACKED MORTAR BETWEEN DELTA FRAME AND SEGMENT WEBS
(H) POUR CIP CONCRETE CLOSURE IN TOP SLAB FOR SEGMENTS S16-11 AND S16-12
(I) WHEN THE CIP CONCRETE REACHES A MINIMUM COMPRESSIVE STRENGTH OF 3500 PSI, STRESS THE 12X0.6" STRAND TENDON OF THE DELTA FRAME AND ALL TRANSVERSE CONTINUITY POST TENSIONING OF SEGMENTS S16-11 AND S16-12
(J) REMOVE P.T. BARS B1 FROM SEGMENTS S15-P16 THROUGH S16-02
(K) SLACKEN TENDONS 1551 THROUGH 1554
(L) REMOVE P.T. BARS OF PIER SEGMENT P15 AND P.T. BARS IN TOP SLAB OF SEGMENTS S14-13, S14-15, S15-01, S15-02
(M) ASSEMBLE AND STRESS STAY 5 TO 1480 KIPS
(N) REMOVE P.T. BARS T2 FROM SEGMENTS S16-07 AND S16-08. REMOVE P.T. BARS T3 AND T4 FROM SEGMENTS S16-03 AND S16-04.

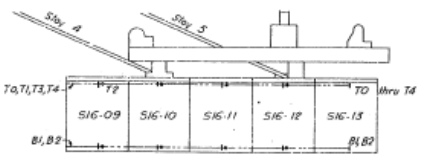

PHASE 14

(A) ADVANCE BEAM AND WINCH TO SEGMENTS S16-12
(B) LIFT SEGMENTS S16-13 FROM BARGE
(C) COUPLE AND STRESS P.T. BARS T1 AND B2 IN SEGMENTS S16-13
(D) COUPLE AND STRESS P.T. BARS T0, T2, T3, T4 IN SEGMENTS S16-13
(E) COUPLE AND STRESS P.T. BAR B1 IN SEGMENTS S16-13

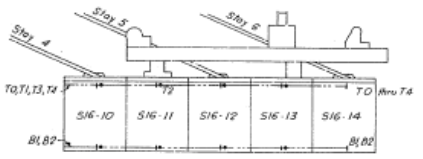

PHASE 15

(A) ADVANCE BEAM AND WINCH TO SEGMENTS S16-13
(B) LIFT SEGMENTS S16-14 FROM BARGE
(C) COUPLE AND STRESS P.T. BARS T1 AND B2 IN SEGMENTS S16-14
(D) COUPLE AND STRESS P.T. BARS T0, T2, T3, T4 IN SEGMENTS S16-14
(E) COUPLE AND STRESS P.T. BAR B1 IN SEGMENTS S16-14
(F) LIFT DELTA FRAME OF SEGMENTS S16-14
(G) PLACE DRY PACKED MORTAR BETWEEN DELTA FRAME AND SEGMENT WEBS
(H) POUR CIP CONCRETE CLOSURE IN TOP SLAB FOR SEGMENTS S16-13 AND S16-14
(I) WHEN THE CIP CONCRETE REACHES A MINIMUM COMPRESSIVE STRENGTH OF 3500 PSI, STRESS THE 12X0.6" STRAND TENDON OF THE DELTA FRAME AND ALL TRANSVERSE CONTINUITY POST TENSIONING OF SEGMENTS S16-13 AND S16-14
(J) REMOVE P.T. BARS B1 FROM SEGMENTS S16-3 AND S16-4
(K) ASSEMBLE AND STRESS STAY 6 TO 1480 KIPS
(L) REMOVE P.T. BARS T2 FROM SEGMENTS S16-09 AND S16-10
REMOVE P.T. BARS T3 AND T4 FROM SEGMENTS S16-05 AND S16-06
REMOVE P.T. BARS T0 AND T1 FROM SEGMENTS S15-P16 THROUGH S16-02

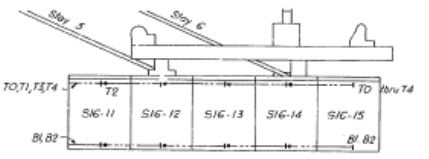

PHASE 16

JR-822

(A) ADVANCE BEAM AND WINCH TO SEGMENTS S16-14
(B) LIFT SEGMENTS S16-15 FROM BARGE
(C) COUPLE AND STRESS P.T. BARS T1 AND B2 IN SEGMENTS S16-15
(D) COUPLE AND STRESS P.T. BARS T0, T2, T3, T4 IN SEGMENTS S16-15
(E) COUPLE AND STRESS P.T. BAR B1 IN SEGMENTS S16-15

The Equipment Schematics are for Information Only
See Sheet 10 for General Notes.

N.B.L. & S.B.L. RTE. 295 OVER JAMES RIVER

MAIN SPAN
ERECTION SEQUENCE III

DESIGNED BY E.P
DRAWN BY J.R.
CHECKED BY J.C.

Figg and Muller Engineers, Inc.
Tallahassee, Fl. / Paris, Fr. / Washington, D.C. / Denver, Co.

No scale

November, 1984

260-32

Sheet 83 of 335

FHWA REGION	STATE	FEDERAL AID		STATE		SHEET
		STATE	PROJECT	ROUTE	PROJECT	NO
3	VA	95		295	0095-020-101,PE 102,B610,B611	15(33)

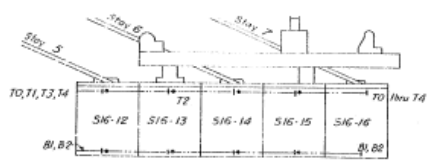

PHASE 17

(A) ADVANCE BEAM AND WINCH TO SEGMENTS S16-15
(B) LIFT SEGMENTS S16-16 FROM BARGE
(C) COUPLE AND STRESS P.T. BARS T1 AND B2 IN SEGMENTS S16-16
(D) COUPLE AND STRESS P.T. BARS T0, T2, T3, . . IN SEGMENTS S16-16
(E) COUPLE AND STRESS P.T. BAR B1 IN SEGMENTS S16-16
(F) LIFT DELTA FRAME OF SEGMENTS S16-16
(G) PLACE DRY PACKED MORTAR BETWEEN DELTA FRAME AND SEGMENT WEBS
(H) POUR CIP CONCRETE CLOSURE IN TOP SLAB FOR SEGMENTS S16-15 AND S16-16
(I) WHEN THE CIP CONCRETE REACHES A MINIMUM COMPRESSIVE STRENGTH OF 3500 PSI, STRESS THE 12X0.6" STRAND TENDON OF THE DELTA FRAME AND ALL TRANSVERSE CONTINUITY POST TENSIONING OF SEGMENTS S16-15 AND S16-16
(J) REMOVE P.T. BARS B1 FROM SEGMENTS S16-05 AND S16-06
(K) ASSEMBLE AND STRESS STAY 7 TO 1480 KIPS
(L) REMOVE P.T. BARS T2 FROM SEGMENTS S16-11 AND S16-12
REMOVE P.T. BARS T3 AND T4 FROM SEGMENTS S16-07 AND S16-08
REMOVE P.T. BARS T0 AND T1 FROM SEGMENTS S16-03 AND S16-04

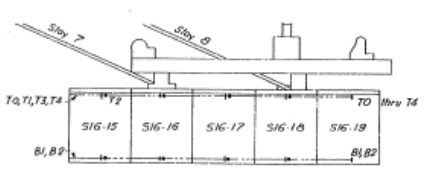

PHASE 20

(A) ADVANCE BEAM AND WINCH TO SEGMENTS S16-18
(B) LIFT SEGMENTS S16-19 FROM BARGE
(C) COUPLE AND STRESS P.T. BARS T1 AND B2 IN SEGMENTS S16-19
(D) COUPLE AND STRESS P.T. BARS T0, T2, T3, T4 IN SEGMENTS S16-19
(E) COUPLE AND STRESS P.T. BAR B1 IN SEGMENTS S16-19

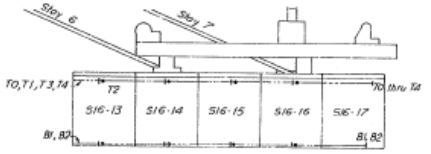

PHASE 18

(A) ADVANCE BEAM AND WINCH TO SEGMENTS S16-16
(B) LIFT SEGMENTS S16-17 FROM BARGE
(C) COUPLE AND STRESS P.T. BARS T1 AND B2 IN SEGMENTS S16-17
(D) COUPLE AND STRESS P.T. BARS T0, T2, T3, T4 IN SEGMENTS S16-17
(E) COUPLE AND STRESS P.T. BAR B1 IN SEGMENTS S16-17

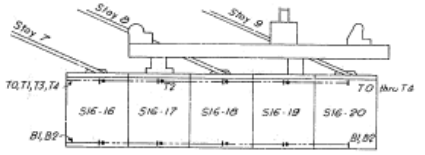

PHASE 21

(A) ADVANCE BEAM AND WINCH TO SEGMENTS S16-19
(B) LIFT SEGMENTS S16-20 FROM BARGE
(C) COUPLE AND STRESS P.T. BARS T1 AND B2 IN SEGMENTS S16-20
(D) COUPLE AND STRESS P.T. BARS T0, T2, T3, T4 IN SEGMENTS S16-20
(E) COUPLE AND STRESS P.T. BAR B1 IN SEGMENTS S16-20
(F) LIFT DELTA FRAME OF SEGMENTS S16-20
(G) PLACE DRY PACKED MORTAR BETWEEN DELTA FRAME AND SEGMENT WEBS
(H) POUR CIP CONCRETE CLOSURE IN TOP SLAB FOR SEGMENTS S16-19 AND S16-20
(I) WHEN THE CIP CONCRETE REACHES A MINIMUM COMPRESSIVE STRENGTH OF 3500 PSI, STRESS THE 12X0.6" STRAND TENDON OF THE DELTA FRAME AND ALL TRANSVERSE CONTINUITY POST TENSIONING OF SEGMENTS S16-19 AND S16-20
(J) REMOVE P.T. BARS B1 FROM SEGMENTS S16-09 AND S16-10
REMOVE P.T. BARS B2 FROM SEGMENTS S16-01 AND S16-02
(K) ASSEMBLE AND STRESS STAY 9 TO 1480 KIPS
(L) REMOVE P.T. BARS T2 FROM SEGMENTS S16-15 AND S16-16
REMOVE P.T. BARS T3 AND T4 FROM SEGMENTS S16-11 AND S16-12
REMOVE P.T. BARS T0 AND T1 FROM SEGMENTS S16-07 AND S16-08

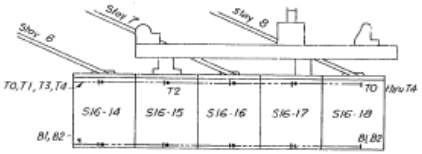

PHASE 19

(A) ADVANCE BEAM AND WINCH TO SEGMENTS S16-17
(B) LIFT SEGMENTS S16-18 FROM BARGE
(C) COUPLE AND STRESS P.T. BARS T1 AND B2 IN SEGMENTS S16-18
(D) COUPLE AND STRESS P.T. BARS T0, T2, T3, T4 IN SEGMENTS S16-18
(E) COUPLE AND STRESS P.T. BAR B1 IN SEGMENTS S16-18
(F) LIFT DELTA FRAME OF SEGMENTS S16-18
(G) PLACE DRY PACKED MORTAR BETWEEN DELTA FRAME AND SEGMENT WEBS
(H) POUR CIP CONCRETE CLOSURE IN TOP SLAB FOR SEGMENTS S16-17 AND S16-18
(I) WHEN THE CIP CONCRETE REACHES A MINIMUM COMPRESSIVE STRENGTH OF 3500 PSI, STRESS THE 12X0.6" STRAND TENDON OF THE DELTA FRAME AND ALL TRANSVERSE CONTINUITY POST TENSIONING OF SEGMENTS S16-17 AND S16-18
(J) REMOVE P.T. BARS B1 FROM SEGMENTS S16-07 AND S16-08
REMOVE P.T. BARS B2 FROM SEGMENTS S15-P16 AND S16-P16
(K) ASSEMBLE AND STRESS STAY 8 TO 1480 KIPS
(L) REMOVE P.T. BARS T2 FROM SEGMENTS S16-13 AND S16-14
REMOVE P.T. BARS T3 AND T4 FROM SEGMENTS S16-09 AND S16-10
REMOVE P.T. BARS T0 AND T1 FROM SEGMENTS S16-05 AND S16-06

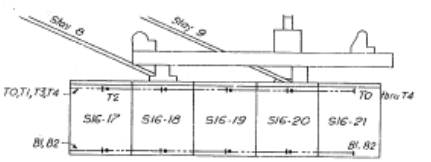

PHASE 22

JR-825

(A) ADVANCE BEAM AND WINCH TO SEGMENTS S16-20
(B) LIFT SEGMENTS S16-21 FROM BARGE
(C) COUPLE AND STRESS P.T. BARS T1 AND B2 IN SEGMENTS S16-21
(D) COUPLE AND STRESS P.T. BARS T0, T2, T3, T4 IN SEGMENTS S16-21
(E) COUPLE AND STRESS P.T. BAR B1 IN SEGMENTS S16-21

The Equipment Schematics are for Information Only
See Sheet 10 for General Notes

N.B.L. & S.B.L. RTE. 295 OVER JAMES RIVER

MAIN SPAN
ERECTION SEQUENCE IV

DESIGNED BY LP
DRAWN BY JH
CHECKED BY MG

Figg and Muller Engineers, Inc.
Tallahassee, Fl. / Paris, Fr. / Washington, D.C. / Denver, Co.

No scale

November, 1984

260-32

Sheet 33 of 133

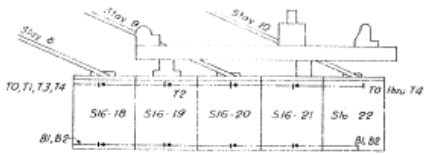

PHASE 23

(A) ADVANCE BEAM AND WINCH TO SEGMENTS S16-21
(B) LIFT SEGMENTS S16-22 FROM BARGE
(C) COUPLE AND STRESS P.T. BARS T1 AND B2 IN SEGMENTS S16-22
(D) COUPLE AND STRESS P.T. BARS T0, T2, T3, T4 IN SEGMENTS S16-22
(E) COUPLE AND STRESS P.T. BAR B1 IN SEGMENTS S16-22
(F) LIFT DELTA FRAME OF SEGMENTS S16-22
(G) PLACE DRY PACKED MORTAR BETWEEN DELTA FRAME AND SEGMENT WEBS
(H) POUR CIP CONCRETE CLOSURE IN TOP SLAB FOR SEGMENTS S16-21 AND S16-22
(I) WHEN THE CIP CONCRETE REACHES A MINIMUM COMPRESSIVE STRENGTH OF 3500 PSI, STRESS THE 12X0.6" STRAND TENDON OF THE DELTA FRAME AND ALL TRANSVERSE CONTINUITY POST TENSIONING OF SEGMENTS S16-21 AND S16-22
(J) REMOVE P.T. BARS B1 FROM SEGMENTS S16-11 AND S16-12
REMOVE P.T. BARS B2 FROM SEGMENTS S16-03 AND S16-04
(K) ASSEMBLE AND STRESS STAY 10 TO 1480 KIPS
(L) REMOVE P.T. BARS T2 FROM SEGMENTS S16-17 AND S16-18
REMOVE P.T. BARS T3 AND T4 FROM SEGMENTS S16-13 AND S16-14
REMOVE P.T. BARS T0 AND T1 FROM SEGMENTS S16-09 AND S16-10

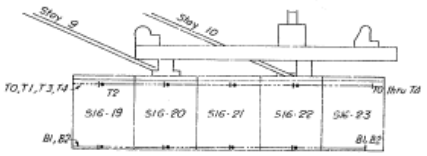

PHASE 24

(A) ADVANCE BEAM AND WINCH TO SEGMENTS S16-22
(B) LIFT SEGMENTS S16-23 FROM BARGE
(C) COUPLE AND STRESS P.T. BARS T1 AND B2 IN SEGMENTS S16-23
(D) COUPLE AND STRESS P.T. BARS T0, T2, T3, T4 IN SEGMENTS S16-23
(E) COUPLE AND STRESS P.T. BAR B1 IN SEGMENTS S16-23

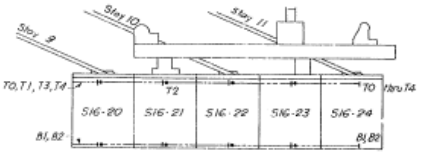

PHASE 25

(A) ADVANCE BEAM AND WINCH TO SEGMENTS S16-23
(B) LIFT SEGMENTS S16-24 FROM BARGE
(C) COUPLE AND STRESS P.T. BARS T1 AND B2 IN SEGMENTS S16-24
(D) COUPLE AND STRESS P.T. BARS T0, T2, T3, T4 IN SEGMENTS S16-24
(E) COUPLE AND STRESS P.T. BAR B1 IN SEGMENTS S16-24
(F) LIFT DELTA FRAME OF SEGMENTS S16-24
(G) PLACE DRY PACKED MORTAR BETWEEN DELTA FRAME AND SEGMENT WEBS
(H) POUR CIP CONCRETE CLOSURE IN TOP SLAB FOR SEGMENTS S16-23 AND S16-24
(I) WHEN THE CIP CONCRETE REACHES A MINIMUM COMPRESSIVE STRENGTH OF 3500 PSI, STRESS THE 12X0.6" STRAND TENDON OF THE DELTA FRAME AND ALL TRANSVERSE CONTINUITY POST TENSIONING OF SEGMENTS S16-23 AND S16-24
(J) REMOVE P.T. BARS B1 FROM SEGMENTS S16-13 AND S16-14
REMOVE P.T. BARS B2 FROM SEGMENTS S16-05 AND S16-06
(K) ASSEMBLE AND STRESS STAY 11 TO 1480 KIPS
(L) REMOVE P.T. BARS T2 FROM SEGMENTS S16-19 AND S16-20
REMOVE P.T. BARS T3 AND T4 FROM SEGMENTS S16-15 AND S16-16
REMOVE P.T. BARS T0 AND T1 FROM SEGMENTS S16-11 AND S16-12

FHWA REGION	STATE	ROUTE	PROJECT	ROUTE	PROJECT	SHEET NO.
3	VA	95		295	0095-020-101,PE-102,B610,B611	9 (132)

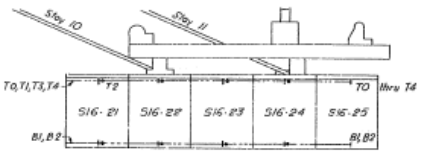

PHASE 26

(A) ADVANCE BEAM AND WINCH TO SEGMENTS S16-24
(B) LIFT SEGMENTS S16-25 FROM BARGE
(C) COUPLE AND STRESS P.T. BARS T1 AND B2 IN SEGMENTS S16-25
(D) COUPLE AND STRESS P.T. BARS T0, T2, T3, T4 IN SEGMENTS S16-25
(E) COUPLE AND STRESS P.T. BAR B1 IN SEGMENTS S16-25

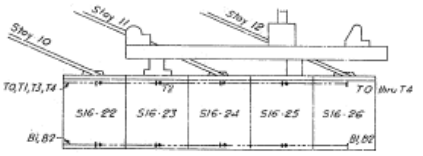

PHASE 27

(A) ADVANCE BEAM AND WINCH TO SEGMENTS S16-25
(B) LIFT SEGMENTS S16-26 FROM BARGE
(C) COUPLE AND STRESS P.T. BARS T1 AND B2 IN SEGMENTS S16-26
(D) COUPLE AND STRESS P.T. BARS T0, T2, T3, T4 IN SEGMENTS S16-26
(E) COUPLE AND STRESS P.T. BAR B1 IN SEGMENTS S16-26
(F) LIFT DELTA FRAME OF SEGMENTS S16-26
(G) PLACE DRY PACKED MORTAR BETWEEN DELTA FRAME AND SEGMENT WEBS
(H) POUR CIP CONCRETE CLOSURE IN TOP SLAB FOR SEGMENTS S16-25 AND S16-26
(I) WHEN THE CIP CONCRETE REACHES A MINIMUM COMPRESSIVE STRENGTH OF 3500 PSI, STRESS THE 12X0.6" STRAND TENDON OF THE DELTA FRAME AND ALL TRANSVERSE CONTINUITY POST TENSIONING OF SEGMENTS S16-25 AND S16-26
(J) REMOVE P.T. BARS B2 FROM SEGMENTS S16-07 AND S16-08
(K) ASSEMBLE AND STRESS STAY 12 TO 1480 KIPS
(L) REMOVE P.T. BARS T2 FROM SEGMENTS S16-21 AND S16-22
REMOVE P.T. BARS T3 AND T4 FROM SEGMENTS S16-17 AND S16-18
REMOVE P.T. BARS T0 AND T1 FROM SEGMENTS S16-13 AND S16-14

DETAILS OF THE KEY TENDON ON THIS SHEET ARE SUBJECT TO REVISION BY THE CONTRACTOR AS DISCUSSED BY THE ENGINEER ON SHOP DRAWINGS.

JR-827

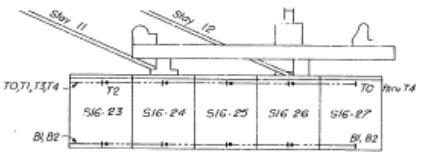

PHASE 28

(A) ADVANCE BEAM AND WINCH TO SEGMENTS S16-26
(B) LIFT SEGMENTS S16-27 FROM BARGE
(C) COUPLE AND STRESS P.T. BARS T1 AND B2 IN SEGMENTS S16-27
(D) COUPLE AND STRESS P.T. BARS T0, T2, T3, T4 IN SEGMENTS S16-27
(E) COUPLE AND STRESS P.T. BAR B1 IN SEGMENTS S16-27

The Equipment Schematics are for Information Only
See Sheet 10 for General Notes.

N.B.L. & S.B.L. RTE. 295 OVER JAMES RIVER

MAIN SPAN
ERECTION SEQUENCE V

Designed by LP
Drawn by JR
Checked by MG

Figg and Muller Engineers, Inc.
Tallahassee, Fl. / Paris, Fr. / Washington, D.C. / Denver, Co.

No scale

November, 1984

260-32

FHWA REGION	STATE	FEDERAL AID ROUTE	FEDERAL AID PROJECT	STATE ROUTE	STATE PROJECT	SHEET NO
3	VA.	95		295	0095-020-101,PE 101,RW[illegible]	15(333)

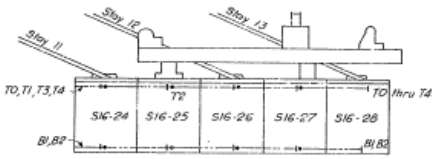

PHASE 29

(A) ADVANCE BEAM AND WINCH TO SEGMENTS S16-27
(B) LIFT SEGMENTS S16-28 FROM BARGE
(C) COUPLE AND STRESS P.T. BARS T1 AND B2 IN SEGMENTS S16-28
(D) COUPLE AND STRESS P.T. BARS T0, T2, T3, T4 IN SEGMENTS S16-28
(E) COUPLE AND STRESS P.T. BAR B1 IN SEGMENTS S16-28
(F) LIFT DELTA FRAME OF SEGMENTS S16-28
(G) PLACE DRY PACKED MORTAR BETWEEN DELTA FRAME AND SEGMENT WEBS
(H) POUR CIP CONCRETE CLOSURE IN TOP SLAB FOR SEGMENTS S16-27 AND S16-28
(I) WHEN THE CIP CONCRETE REACHES A MINIMUM COMPRESSIVE STRENGTH OF 3500 PSI, STRESS THE 12X0.6" STRAND TENDON OF THE DELTA FRAME AND ALL TRANSVERSE CONTINUITY POST TENSIONING OF SEGMENTS S16-27 AND S16-28
(J) REMOVE P.T. BARS B2 FROM SEGMENTS S16-09 AND S16-10
(K) ASSEMBLE AND STRESS STAY 13 TO 1580 KIPS
(L) REMOVE P.T. BARS T2 FROM SEGMENTS S16-25 AND S16-24
REMOVE P.T. BARS T3 AND T4 FROM SEGMENTS S16-19 AND S16-20
REMOVE P.T. BARS T0 AND T1 FROM SEGMENTS S16-15 AND S16-16

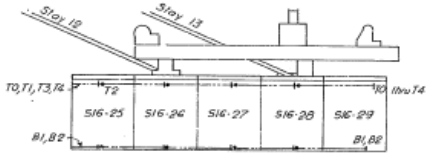

PHASE 30

(A) ADVANCE BEAM AND WINCH TO SEGMENTS S16-28
(B) LIFT SEGMENTS S16-29 FROM BARGE
(C) COUPLE AND STRESS P.T. BARS T1 AND B2 IN SEGMENTS S16-29
(D) COUPLE AND STRESS P.T. BARS T0, T2, T3, T4 IN SEGMENTS S16-29
(E) COUPLE AND STRESS P.T. BAR B1 IN SEGMENTS S16-29

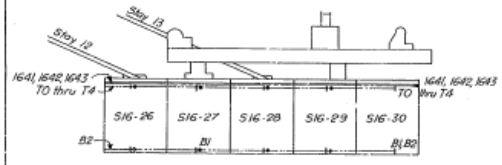

PHASE 31

(A) ADVANCE BEAM AND WINCH TO SEGMENTS S16-29
(B) LIFT SEGMENTS S16-30 FROM BARGE
(C) COUPLE AND STRESS P.T. BARS T1 AND B2 IN SEGMENTS S16-30
(D) COUPLE AND STRESS P.T. BARS T0, T2, T3, T4 IN SEGMENTS S16-30
(E) COUPLE AND STRESS P.T. BAR B1 IN SEGMENTS S16-30
(F) LIFT DELTA FRAME OF SEGMENTS S16-30
(G) PLACE DRY PACKED MORTAR BETWEEN DELTA FRAME AND SEGMENT WEBS
(H) POUR CIP CONCRETE CLOSURE IN TOP SLAB FOR SEGMENTS S16-29 AND S16-30
(I) WHEN THE CIP CONCRETE REACHES A MINIMUM COMPRESSIVE STRENGTH OF 3500 PSI, STRESS THE 12X0.6" STRAND TENDON OF THE DELTA FRAME AND ALL TRANSVERSE CONTINUITY POST TENSIONING OF SEGMENTS S16-29 AND S16-30
(J) STRESS TENDONS 1641, 1642 AND 1643
(K) REMOVE P.T. BARS B1 FROM SEGMENTS S16-15 THROUGH S16-26
REMOVE P.T. BARS B2 FROM SEGMENTS S16-11 THROUGH S16-24
REMOVE P.T. BARS T0 AND T1 FROM SEGMENTS S16-17 AND S16-18

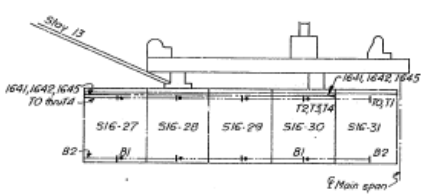

PHASE 32

(A) ADVANCE BEAM AND WINCH TO SEGMENTS S16-30
(B) LIFT SEGMENTS S16-31 FROM BARGE
(C) COUPLE AND STRESS P.T. BARS T1, B2 AND T0 IN SEGMENTS S16-31
(D) POUR CIP CONCRETE CLOSURE IN TOP SLAB OF SEGMENTS S16-31
(E) WHEN THE CIP CONCRETE REACHES A MINIMUM COMPRESSIVE STRENGTH OF 3500 PSI, STRESS ALL TRANSVERSE CONTINUITY POST-TENSIONING OF SEGMENTS S16-31

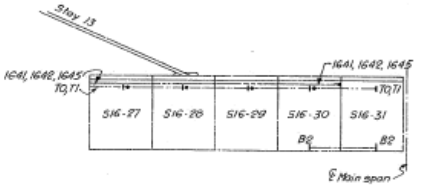

PHASE 33

(A) REMOVE BEAM AND WINCH FROM CANTILEVER, TRANSPORT TO PIER 17, AND BEGIN FOR PROGRESSIVE CANTILEVER CONSTRUCTION
(B) REMOVE ALL P.T. BARS B1
REMOVE P.T. BARS B2 FROM SEGMENTS S16-25 THROUGH S16-29
REMOVE ALL P.T. BARS T2, T3 AND T4
REMOVE P.T. BARS T0 AND T1 FROM SEGMENTS S16-19 THROUGH S16-25

DETAILS OF THE STEAM CURING TO BE SUBMITTED FOR APPROVAL AS REQUIRED BY THE CONTRACT AND SPECIFIED ON THESE DRAWINGS
JR-826

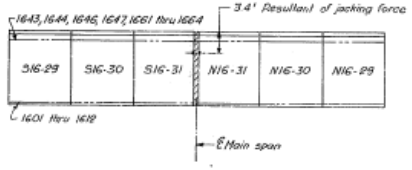

PHASE 34 - MAIN SPAN CLOSURE

The Equipment Schematics are for Information Only
See Sheet 10 for General Notes.

(A) PROGRESSIVE CANTILEVER CONSTRUCTION OF PIER 17 IS COMPLETED THROUGH PHASE 32.
(B) REMOVE P.T. BARS IN SEGMENTS S14-07 THROUGH S14-09 AND IN SEGMENTS N18-06 THROUGH N18-08
(C) JACK AT CLOSURE BETWEEN PIER 16 AND 17 CANTILEVERS BY APPLYING A FORCE OF 150K PER WEB (600 KIPS TOTAL). THE JACKS SHALL BE PLACED SUCH THAT THE RESULTANT OF THE JACKING FORCE LIES 3.4 FEET BELOW THE TOP OF THE TOP SLAB
(D) SHIM AND POUR CLOSURE JOINT
(E) WHEN CONCRETE OF CLOSURE JOINT REACHES A MINIMUM COMPRESSIVE STRENGTH OF 2500 PSI, STRESS, IN THE ORDER GIVEN, THE FOLLOWING TENDONS:
1612 - 1644 AND 1647 - 1664 - 1611 - 1610 - 1609
1645 - 1646 - 1663 - 1662 - 1661
1608 - 1607 - 1606 - 1605 - 1604 - 1603 - 1602 - 1601
(F) REMOVE ALL P.T. BARS T0,T1, AND B2.

N.B.L. & S.B.L. RTE. 295 OVER JAMES RIVER

MAIN SPAN ERECTION SEQUENCE VI

DESIGNED BY
DRAWN BY
CHECKED BY

Figg and Muller Engineers, Inc.
Tallahassee, Fl. / Paris, Fr. / Washington, D.C. / Denver, Co.

No scale

November, 1984

260-32
Sheet 233 of 329